Numerical simulation of borehole thermal energy storage in the geological subsurface

Dissertation
zur Erlangung des Doktorgrades
der Mathematisch-Naturwissenschaftlichen Fakultät
der Christian-Albrechts-Universität zu Kiel

vorgelegt von
Anke Boockmeyer
Meerbusch, Mai 2020

Erster Gutachter:	Prof Dr. Sebastian Bauer
Zweiter Gutachter:	Prof. Dr. Peter Bayer

Tag der mündlichen Prüfung: 11.08.2020

gez. Prof. Dr. Frank Kempken, Dekan

Kurzfassung

Für die Bereitstellung von Wärme im Winter wird zunehmend Wärme saisonal im geologischen Untergrund gespeichert. Dabei wird überschüssige Wärmeenergie verwendet, die aus Solarthermie durch Solarkollektoren, industriellen Prozessen oder Raumkühlung stammt. Speichertechnologien wie Hochtemperatur-Erdsondenspeicher können so im Winter den Wärmebedarf decken und im Sommer wieder aufladen, wenn keine Heizung benötigt wird. Für eine breite Anwendung dieser Speichertechnologie sind ausreichende Systemkenntnisse hinsichtlich Speichereigenschaften, Dimensionierung sowie induzierten Auswirkungen erforderlich. In dieser Arbeit werden deshalb diese Speichersysteme mit numerischen Szenariosimulationen unter Verwendung des wissenschaftlichen Simulators OpenGeoSys untersucht. Die Wärmespeicherung wird dabei mit einem validierten numerischen Modell einer Erdwärmesonde in homogenem Untergrund simuliert, um ein Verständnis der gekoppelten induzierten thermischen und hydraulischen Prozesse bei hohen Temperaturen zu erhalten. Für eine korrekte Darstellung der steilen Temperaturgradienten werden in dem Modell die komplexe Sondengeometrie mit allen Komponenten berücksichtigt. Die Ergebnisse zeigen, dass in Speicherformationen mit hoher Permeabilität thermische Konvektion auftreten kann und dass dies die Speichereigenschaften stark beeinflusst. Insbesondere reduziert die Konvektion die Speicherkapazität so stark, dass die Wärmespeicherung ineffizient wird. Aus diesem Grund sollten für Wärmespeicherung im Untergrund gering-permeable Formationen gewählt werden. Weitere Szenariosimulationen zur Untersuchung von Hochtemperatur-Wärmespeicherung in größerem Maßstab werden unter rein konduktiven Bedingungen durchgeführt. Ein Speicher mit mehreren Erdwärmesonden wird verwendet, um gegenseitige Beeinflussung der einzelnen Sonden, Speicherkapazitäten und Umweltauswirkungen zu untersuchen. Zu diesem Zweck wird ein vereinfachtes Modell für die BHEs entwickelt und validiert, das eine effiziente und dennoch genaue Simulation der Wärmespeicherung mit geringerem Rechenaufwand ermöglicht. Mit diesem Ansatzes werden Speicherszenarien unter Verwendung typischer thermischer Parameter und Speicherzykluslängen simuliert, um ihre jeweiligen Auswirkungen auf Speichermerkmale wie Speicherkapazitäten und -raten sowie induzierte Temperaturänderungen zu quantifizieren. Darüber hinaus werden durch Variation von Erdsonden-Anzahl und -Entfernung Abhängigkeiten für die Speicherdimensionierung abgeleitet. Es zeigt sich, dass die sich thermische Parameter und Zykluslänge auf das Speicherverhalten auswirken und somit den Raumbedarf des Speichers beeinflussen. Anzahl und Abstand der Sonden wirken sich stark auf Speicherkapazitäten sowie induzierte Auswirkungen aus und können außerdem nachteilige Untergrundeigenschaften ausgleichen. Numerische Simulationen sind also für jede in-

dividuelle Speicherlokation erforderlich, um Temperatureinflüsse auf den Untergrund am ausgewählten Speicherort zu identifizieren und vor der Installation eines Speichers dessen optimale Dimensionen zu ermitteln.

Abstract

Seasonal storage of heat in the subsurface is an increasingly used technology for providing heat during winter by storing surplus energy from primary producers. Storage technologies such as high-temperature borehole thermal energy storage (BTES) could meet the heat demand in winter and recharge in summer when heating is not necessary. For a broad application of this storage technology, an adequate system knowledge is required in terms of storage characteristics, dimensioning and the induced effects. In this thesis, high-temperature BTES systems are studied with numerical scenario simulations using the scientific open source simulator OpenGeoSys. For gaining a thorough understanding of the coupled induced thermal and hydraulic processes with high temperatures, heat storage is simulated with a validated numerical model of a single borehole heat exchanger (BHE) in a homogeneous subsurface. This model accounts for the complex BHE geometry with all its components to ensure a correct representation of the steep temperature gradients. It is shown that thermal convection can occur in storage formations with high permeability and that this strongly affects the storage characteristics. In particular, heat convection reduces the storage capacity to the point at which heat storage becomes inefficient. For this reason, conditions that prevent thermally induced convection should be constraining the decision process of storage site locations. Further scenario simulations investigating high-temperature heat storage on a larger scale are thus placed in a conductive setting. A BTES model consisting of multiple BHEs is used to assess mutual BHE interferences, storage impacts and capacities. For this purpose, an adapted modelling approach is developed and validated for the comprising BHEs, making efficient yet accurate simulation of heat storage with feasible computational effort possible. Using this approach, storage scenarios are simulated employing sets of typical subsurface thermal parameters and storage cycle lengths to quantify their respective impact on storage features such as storage capacities and rates as well as induced temperature changes. Additionally, storage layouts are varied in terms of BHE number and distance to derive dependencies for storage dimensioning. The simulation results show that the effects of thermal parameters and cycle length on storage behaviour are fundamental for determining required dimensions of the BTES. BHE distance and number strongly affect storage features and induced impacts in the subsurface; they can further compensate for disadvantageous subsurface conditions. Optimal storage dimensions in terms of BHE distance thus have to be identified at the given storage site. The results show further that site-specific numerical simulations are necessary to identify temperature impacts on the subsurface at the selected storage site and to execute an ideal dimensioning before installing a BTES.

Contents

List of Figures

List of Tables

1 Introduction

1.1 Energy transition and heat storage

During the last decades, changes in the climate system have been observed worldwide. The Intergovernmental Panel on Climate Change (IPCC) is the United Nations body for assessing the science related to climate change. Its 2014 report states:

> *"Warming of the climate system is unequivocal, and since the 1950s, many of the observed changes are unprecedented over decades to millennia. The atmosphere and ocean have warmed, the amounts of snow and ice have diminished, and sea level has risen."*

In fact, today's temperatures and sea levels are the highest in the history of recordings and climate-related weather extremes have drastically increased (USGCRP et al. 2017). Numerous scientific studies yield that the rising greenhouse gas concentration in the atmosphere due to burning of fossil fuels for power and energy generation is most likely the major cause for climate change (Oreskes 2018, UBA 2013). Mitigating or even preventing further climate change requires immense reduction of CO2 and other greenhouse gas emissions (IPCC et al. 2014). In this context, the German government enacted the "Climate Action Plan 2050" to decrease carbon emissions by 80 to 95 % by 2050 compared to 1990 levels (BMUB 2016). With conventional sources being the major contributor to carbon emissions and at the same time accounting for almost 80 % of the total primary energy supply in Germany today (AGEB 2019), the task of drastically decreasing carbon emissions in the future will be challenging. Despite advancing developments in renewable energy production, energy efficiency and distribution, necessary progress is slow and the transition to a complete renewable energy production will take decades (IEA 2016). Additionally, the major renewable sources, i.e. wind and solar energy, undergo diurnal and seasonal fluctuations due to changing weather conditions and thus must be expanded massively to reliably cover the energy demand. Expansion of these renewable energy sources takes time and even if their availability meets the demand in the future, other technologies still must compensate for their fluctuations. For this reason, a successful energy transition also involves the expansion of storage capacities (BMWi 2010). In 2017, the overall end energy consumption was 2592 TWh, turning the energy sector into the main contributor to carbon emission (AGEB 2019). Around 25 % of the energy consumption falls on households, 30 % each on transport or industry and 15 % on the service/business sector (Fig. 1.1). Between these four sectors, the application percentage share varies significantly. Yet, except for the transport sector, where only mechanical energy is needed, the energy needed for heating pur-

poses, i.e. space heating, hot water and process heating, accounts for more than 60 % in each sector. In the three sectors combined, heat consumption accounts for 77 %; in households, this share is even 90 % (Fig. 1.1).

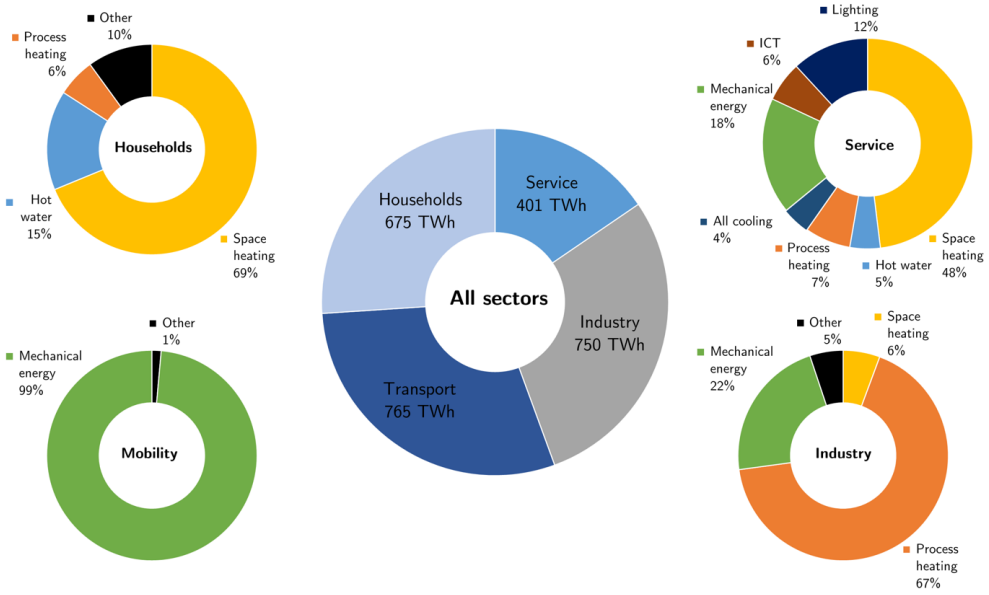

Fig. 1.1 *Energy consumption 2017 by sector with their individual percentage share by application. Energy data ascertained by AGEB (2019)*

For this reason, energy transition will only succeed with heat transition through reducing heat demand, improving insulation of buildings and substituting conventional heat sources by renewables (BMUB 2016). However, the possibilities of renewable heat production are limited. Compared to renewable fuels (i.e. wood, biogas) or electric heating, the more promising options are solar thermal energy, waste heat from either industrial processes or space cooling or even heat generation from surplus wind power (Sternberg and Bardow 2015). Consequently, due to the diurnal and seasonal fluctuations of these options, there is a need for thermal energy storage, a seasonal storage option that bears large potential for renewable heat supply (Santamouris 2001). With thermal energy storage, heat produced during availability periods in summer can be stored for use during demand periods in winter. Seasonal storage of heat requires very large storage capacities at yearly cycles.

There are four possible types of seasonal heat storage, either tanks or systems that store heat directly in the subsurface, that are commonly installed in Germany. They are frequently described in the literature as follows (e.g. by Benner et al. 2003 or Schmidt et al. 2003):

(1) *Hot-water tanks.* Separated storage volume commonly built of concrete filled with water and thermally insulated to the surroundings. Heat is stored through direct water exchange. With this storage type, high heat capacities and charging/discharging rates can be achieved and they can be built almost everywhere. Due to high construction and material costs, hot-water tanks are the most expensive heat storage types.

(2) *Gravel-water tanks.* Separated storage volume like a hot-water tank, but filled with a gravel/water or soil/water mixture. Built of plastic liner and insulation layer. Heat storage is performed either directly by water exchange or indirectly by pipes filled with water running through the tank. With this storage type, material costs are high as well and to achieve heat capacities that are comparable to hot-water tank capacities, a 1.5 times higher volume is required.

(3) *Aquifer thermal energy storage.* Heat is stored directly in the subsurface through two wells that inject and extract groundwater into and from the storage formation. For aquifer heat storage, high permeabilities are required but natural groundwater flow should be very low or non-existent in the storage formation. With the layers above and below being aquitards with low permeability, water will only be exchanged in the aquifer. As heat insulation is not possible, large storage volumes and thus high aquifer thicknesses are required to stem heat loss. Because the subsurface is directly used as storage medium, groundwater exchange in combination with high temperatures can result in unwanted geochemical or microbiological changes inside the storage formation that might potentially damage the system.

(4) *Borehole thermal energy storage.* Heat is stored in the subsurface with multiple borehole heat exchangers. Charging or discharging takes place by circulating hot or cold water through them. Like with aquifer heat storage, large storage volumes are needed, as heat insulation is only possible on top of the storage and natural groundwater flow should be non-existent. In contrast, borehole heat storage can also be installed in low-permeable layers. Additionally, the numbers of boreholes can be raised to meet higher heat demand at comparatively low material and installation costs.

Compared to hot-water or gravel-water tanks, BTES is less expensive and can be extended by adding more boreholes. Thus, BTES can adapt to increasing heat demand. Compared to ATES, BTES is more flexible in terms of storage location as boreholes can be drilled in low permeable layers as well (Schmidt et al. 2003). Furthermore, BTES is less sensitive to changes in geochemistry or microbiology. Because of these mentioned reasons, BTES is chosen out of the four storage options for investigating and quantifying induced effects as well as characterizing storage behaviour in this thesis.

1.2 Borehole thermal energy storage

Borehole thermal energy storage (BTES) uses the subsurface directly as a storage medium. Arrays of vertical borehole heat exchangers (BHEs) are installed to inject heat into and extract heat from the subsurface (Bollin et al. 2013). BHEs can be single U-tube, double U-tube or coaxial pipes made of synthetic polymers. For BTES, they are placed in vertical boreholes and embedded in a grouting material that connects the pipe with the surrounding subsurface material. Typical storage formations are low-permeable layers with high heat capacity, where natural groundwater flow is non-existent (Bauer et al. 2013a).

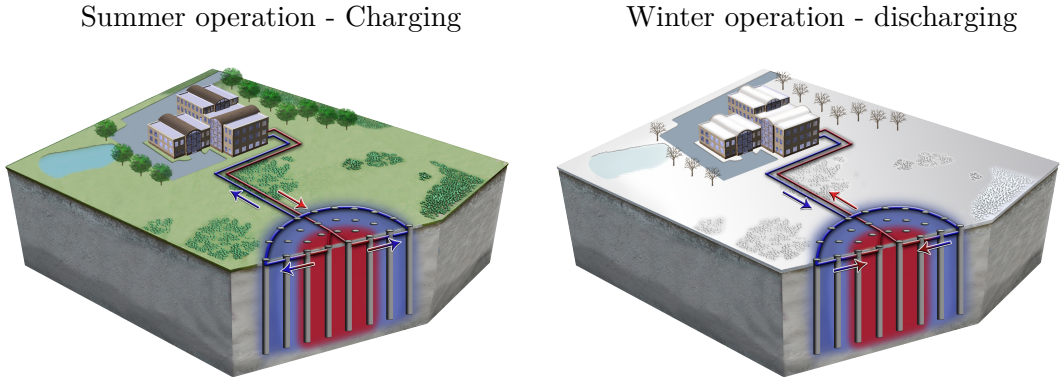

Fig. 1.2 *Principle of BTES through an array of vertical BHEs (*Underground Energy *2019)*

For charging in summer, a working fluid is heated with solar or waste heat and cycles through the BHEs. Due to the temperature gradient from the circulating fluid towards the storage formation, heat is conductively transferred to the surrounding subsurface. The subsurface temperature increases during charging (Fig. 1.2). For discharging in winter, the process is reversed and cold fluid is used (Bockelmann et al. 2011). As the heat carrier fluid remains inside the BHEs, BTES is a so-called closed storage system.

The amount of heat in the storage formation changes only by heat conduction between subsurface and BHE. High working fluid temperatures result in large temperature gradients and thus increase heat transfer rates and capacities (Hauer et al. 2013).

1.2.1 Storage applications

The first pilot plants storing waste heat or solar heat in BTES were installed in Europe the 80's (Rees 2016). With maximum temperatures above 60 °C inside the storage, the BTES systems in Luleå, Sweden and in Groningen, Netherlands, already used high temperatures to achieve high rates and capacities and thus a high efficiency of the operation. An unsaturated layer on top of the storage insulates both storage applications (Nordell 1990, Wijsman and Havinga 1988). The BTES in Luleå was built to store industrial waste heat and provide space heating for a University Building. It consisted of 120 BHEs with 4 m distance and a length of 65 m each. However, it was taken out of operation in 1990 due to lower performance than expected regarding heat injection and recovery (Nordell 1993). In Groningen, solar heat is stored through 360 BHEs until this day. The BHEs each are 20 m deep, installed in a distance of 0.5 m between each other and thus comprise a subsurface volume of $23,000\,\mathrm{m}^3$ with a storage capacity of over 600 MWh (van Meurs 1985).

Since then, a large number of BTES has been installed worldwide. Although there is no official statistics on the number of BTES systems, around 400 systems were estimated to be in operation in Sweden by 2011; the number of boreholes for heat storage in the Netherlands was about 22,500 in 2007. In other European countries, the numbers are increasing as well (Gao et al. 2015). Most of the BTES system described in the literature operate with maximum temperatures below 50 °C. However, several storage applications reach higher temperatures (Lundh and Dalenbäck 2008, Rees 2016). The best-known examples for high-temperature systems operating today with the purpose to partly cover the heat demand of residential areas in winter are located in Crailsheim and Neckarsulm, Germany, Okotoks, Canada, and in Brædstrup, Denmark (Specific characteristics in Tab. 1.1 and 1.2).

The four abovementioned systems are all solar thermal heating plants with heat storage based on the same principle: heat supplied by solar collectors is mainly stored in buffer tanks. Surplus heat is then charged into BTES and discharged when needed. If necessary, further heat is supplied by district heating or other production sources (Fig. 1.3, by example of the Crailsheim solar thermal plant).

Tab. 1.1 *Examples of high-temperature BTES applications: storage geometry properties*

Location	Year	Number	Distance [m]	Depth [m]	Volume [m^3]
Luleå, Sweden	1983	121	4	65	115,000
Groningen, Netherlands	1984	360	0.5	20	23,000
Neckarsulm, Germany	1997	528	1.5-2.5	30	63,000
Crailsheim, Germany	2008	80	3	55	37,000
Okotoks, Canada	2007	144	2.25	35	35,000
Brædstrup, Denmark	2012	48	3	45	19,000

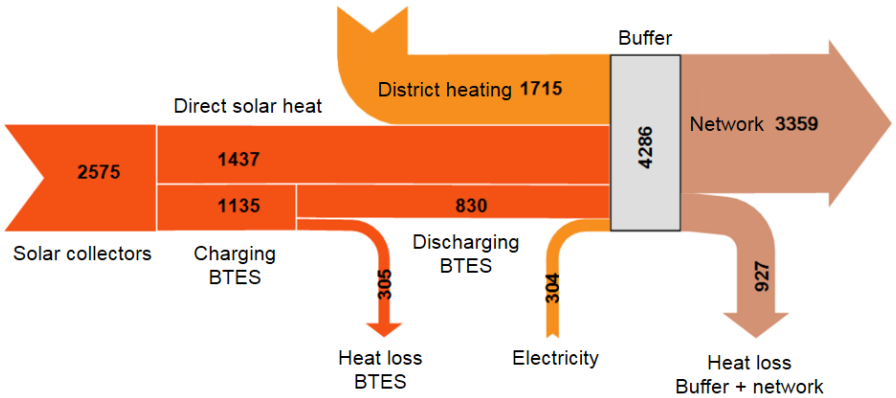

Fig. 1.3 *Energy flow diagram for the solar district heating plant in Crailsheim, Germany during planning process (after Mangold et al. 2012)*

In Germany, the two most detailed documented BTES applications are located in Neckarsulm and Crailsheim. With both systems, solar thermal energy is stored at high temperatures through BHEs in the subsurface to be retrieved and fed into the local heat network during times of high heat demand (Bauer et al. 2009). In Neckarsulm, 528 double U-tube BHEs are used for storage. They cover a subsurface volume of $63,000\,m^3$, as they are installed in a depth of 30 m and in distances of 1.5 to 2.5 m between each other. After four years of heat injection only, small amounts of heat were extracted at first increasing with time. After 10 years of operation, the storage volume was charged with ~1100 MWh at the maximum, leading to temperatures of 65 °C at the end of heat injection. In the same year, almost 800 MWh were recovered resulting in minimum temperatures of 30 °C after heat recovery. With this heat amount, the

BTES systems contributes almost a quarter to the local heat network that provides for a development area with 350 homes (Bauer et al. 2013a). The BTES system in Crailsheim supplies 300 homes with heat through the local heat network. The subsurface storage includes 80 double U-tube BHEs of 55 m length in 3 m distance with a volume of $37,500\,m^3$. This storage volume was charged for three years reaching temperatures of up to 60 °C inside the storage, before a considerable amount of heat could be extracted. After that, around 800 MWh could be injected and 400 MWh could be regained during the storage cycles. With this amount, the BTES contributes less than 10 % to the heat demand (Schmidt 2015).

Tab. 1.2 *Examples of high-temperature BTES applications: storage characteristics*

Location	Temperature max. [°C]	Heat supply [MWh/a]	Formation
Luleå, Sweden	65	1000	Granitic/gneissic bedrock
Groningen, Netherlands	>60	>400	Fine sand, clay, peat
Neckarsulm, Germany	65	800	Claystone, limestone, marl, dolomite
Crailsheim, Germany	60	400	Claystone, limestone, dolomite
Okotoks, Canada	>65	250	Moraine (clay, silt, sand)
Brædstrup, Denmark	50	530	Clay till, sand, silt

The Drake Landing Solar Community in Okotoks, Canada stores solar energy with BTES for supplying space heating to 52 homes. 144 single U-tube BHEs, each 35 m deep, are plumbed in distances of 2.25 m and covered with a layer of insulation beneath the topsoil (Sibbitt et al. 2007). In the 5th year of operation, around 580 MWh could be stored in the storage volume of $35,000\,m^3$ at peak temperatures of over 65 °C in the centre of the BTES (Sibbitt et al. 2012). Another high-temperature BTES system is located in Brædstrup, Denmark, where a residential area is supplied with seasonally stored solar thermal heat through a district heating network (Sørensen et al. 2013). Until now, the storage has $19,000\,m^3$ and consists of 48 BHEs. The BHEs are 45 m long with 3 m distance between each other. Heat insulation of mussel shells is installed on top of the storage. After the first years of operation, the storage provides around 530 MWh at temperatures of around 50 °C in the storage (Schmidt and Sørensen 2018).

Comparison of the four BTES systems illustrates that their contribution to the respective heating network mainly depends on the storage volume and the injected heat amount. With large storage volume, larger amounts of heat can be charged and thus discharged, as shown by example of Neckarsulm. The reason is that large volumes have a smaller surface-to-volume-ratio than small volumes, which reduces heat loss from them. Another influencing factor is the temperature of the heat carrier fluid. Most BTES systems are discharged with comparatively high temperatures around 30 °C. Because of the resulting low temperature gradient between fluid and storage formation, the storage efficiencies are between 40 and 50 %, except for Neckarsulm where a storage efficiency of over 70 % is achieved due to large storage volume. Extracting heat at much lower temperatures leads to higher efficiencies, i.e. temperatures of 12 °C are used to discharge Brædstrup BTES, producing a storage efficiency of almost 65 % despite its small storage volume. The extracted heat per meter borehole is affected by the temperature as well. For example, the Brædstrup BTES reaches 0.24 MWh per borehole metre during heat recovery while the Crailsheim storage only achieves 0.09 MWh/m in comparison. In addition, the injected heat per metre borehole is higher with 0.18 MWh for the Crailsheim BTES, but still half as much as the injected heat per metre in Brædstrup. This emphasizes that high temperature differences between working fluid and subsurface and thus high injection/low recovery temperatures are most favourable for heat storage.

1.2.2 Storage processes and their environmental impact

Heat injection and recovery through BTES induces a temperature signal in the subsurface that is used as storage formation. Besides thermal processes, this can cause hydraulic, chemical or geomechanical processes. Occurrence and extent of these processes mainly depend on the subsurface properties and even more on the imposed temperatures, which are in turn controlled by the storage settings. In the storage formation, this can cause environmental impacts or affect the storage operation itself. For this reason, the different storage processes are introduced in this chapter. Since chemical and geomechanical effects are not investigated in this thesis, only a short overview of these processes is given here.

Thermal processes

For injection of heat with a BTES system, water at high temperatures is cycled through BHEs. Heat transport is convective there because it is controlled by the fluid flow resulting from the flow rate specified for the operation. As temperatures in the subsurface, which functions as storage formation, are significantly lower, a temperature gradient is

built up. Through pipe and grout, heat transport is conductive only as these components are impermeable for flow. Following the principles of heat conduction in solids formulated by Carslaw and Jaeger (1959), their thermal properties and the temperature difference between heat carrier fluid and storage formation control the conductive heat transfer. Typical storage formations are low-permeable with the result that natural groundwater flow is non-existent or slow (Schmidt et al. 2003). With such subsurface condition, the introduction of high temperatures causes heat conduction only. Heat transport points in the direction of the temperature gradient, i.e. towards comparatively lower temperatures. Extent, magnitude, and shape of the resulting temperature distribution depend on the storage characteristics and subsurface properties. Homogenous thermal conductivity and heat capacity of the porous formation lead to a uniform temperature distribution where heat spreads radially away from the storage into the formation. In the case of heterogeneously distributed thermal parameters, a different shape may be expected (Carslaw and Jaeger 1959).

Hydraulic processes

In addition to conductive heat transport, hydraulic processes may theoretically occur, causing convective heat transport and thus enhancing heat transfer from the BHEs into the subsurface. One reason for convective heat transport could be the presence of natural groundwater flow in the storage formation (Chiasson et al. 2000). Among others, high groundwater flow is typically associated with high permeabilities. Even moderate groundwater flow may lead to significant heat loss as heat that is injected is transported away and cannot be recovered (Emad Dehkordi et al. 2015). The other reason for convective heat transport could be thermally induced convection. Due to the temperature dependence of groundwater density and viscosity, thermal and hydraulic processes are coupled and heating of natural groundwater can result in the forming of convection cells. The likelihood of thermally induced convection increases when the temperatures used for heat injection strongly differ from the subsurface temperatures and when the storage formations are well permeable (Skarphagen et al. 2019). Significant convection can result in heat being lost from the BTES. However, thermally induced convection is not the center of current research and is avoided in practice by choosing low permeable storage formations.

Chemical processes

When heat is injected into the storage formation and temperatures rise, the chemical equilibrium is changed and various geochemical reactions can be triggered. For example, this can change groundwater chemistry due to the temperature dependency of mineral

dissolution and precipitation processes (Jesußek et al. 2013). Both processes can affect hydraulic and thermal properties of the storage formation and in consequence potentially impair the BTES system's performance. Moreover, increasing temperatures can result in formation of a separate gas phase in the subsurface that additionally affects the heat transport (Lüders et al. 2016).

Geomechanical processes

With the alternating temperatures in the storage formation, heat storage with heat injection and recovery can induce geomechanical processes. Besides others, cyclic heat storage may for example cause damage accumulation especially in heterogeneous storage formations. This can be expressed in thermal ratcheting and progressing rearrangement of the subsurface material's granular structure due to different thermal expansion properties (Pasten and Santamarina 2011). In turn, this can affect the thermal properties and therefore the heat transport.

The described processes are storage site specific and they impact the surrounding subsurface. Thermal impact (when conductive only) is highest in the storage area and decreases rapidly with increasing distance to the BTES system. In vertical direction, the extent is expected to be similar to the horizontal direction as thermal properties are typically isotropic and vary within tight boundaries. Hydraulic processes can go far distances when induced, with the result that temperature is transported further away from the storage site. Their potential regional extent is highly coupled to the extent of the subsurface layer that allows for thermal convection. These aspects have to be considered when planning a BTES system to estimate spatial demands (Bauer et al. 2015). Temperature impacts and associated space requirements should thus be regarded in the process. Additionally, an increase of the number of BTES systems installed can be expected in the future. Therefore, subsurface spatial planning will become more important and spatial demands will have to be considered in the planning process (Kabuth et al. 2017). This emphasises that there is a need for investigations that include heat storage impacts especially with high temperatures applied.

1.2.3 Numerical simulation of heat storage

For subsurface planning, the abovementioned processes, induced in the subsurface by heat storage through BHEs, can be investigated and predicted by mathematical models. Analytical solutions that approximate BHEs can be applied. They are principally used for interpretation of thermal response tests (e.g. Sass and Lehr 2011, or Poulsen and Alberdi-Pagola 2015) and to a lesser extend for large-scale applications. Introducing

simplifying assumptions, analytical solutions can for example account for either interaction of multiple BHEs (e.g. Beck et al. 2013), spatial heterogeneities (e.g. Abdelaziz et al. 2014) or vertical heat transport inside the storage formation (e.g. Bandos et al. (2009)). For this reason, their applicability is restricted and not sufficient for large-scale BTES systems in real geological settings.

The mathematical model should comprise all described processes and their interactions with each other. Especially due to the complexity of BTES systems with their geometry and operational setup as well as the amount of different materials involved, numerical simulations are the only applicable tool to analyse heat storage processes. Numerical simulations use computer codes to model the associated processes and the behavior of all BHE components and storage formation. They predict heat storage processes and assess the environmental impacts related to the storage operation. Numerical simulations serve as tool for an effective site characterisation and therefore form the basis of decision-making processes (NETL 2017).

Many decades of research and development have shown that numerical simulations are a very important method for planning and operating subsurface storage projects. Numerical simulations are performed using simulation codes capable of representing the dynamics of these subsurface storage systems (NETL 2017). Research has brought up many modelling codes for application to BTES. One simulation code capable of taking into account all physical effects related to subsurface storage is the simulation system OpenGeoSys (OGS) (e.g. Kolditz et al. 2012). OGS is a process and object oriented numerical code (Kolditz and Bauer 2004, Wang et al. 2009), that solves the mathematical equations with a finite element method, which allows for a detailed representation of the complex BTES system. OGS is a coupled simulator that is able to solve the combined equations for more than one of the processes. Concerning heat storage at high temperatures, OGS can handle variable fluid densities and viscosities for solving coupled thermal and hydraulic processes. This is necessary for reliable quantification of these processes and their impacts. OGS can further include geomechanical effects (Watanabe et al. 2012) and geochemical reactions (e.g. Li et al. 2014, Bauer et al. 2012) if required.

Numerical simulations with OGS thus allow for an investigation of storage characteristics and induced impacts by BTES in the geological subsurface. With the gained results, decision making at all stages of a BTES project can be supported. Therefore, numerical simulations serve as a critical component for the site assessment and should always be part of the planning and management of a storage site.

1.3 Aims of this thesis

Research activities and especially pilot storage projects show that high temperature differences between heat carrier fluid and subsurface yield high storage rates and efficiencies. This means that high-temperature BTES can be a worthwhile storage option to compensate for fluctuations in the renewable heat production or to recycle waste heat. Additionally, many geological formations without natural groundwater flow can be considered as storage location, ensuring a wide applicability and large storage potential. However, although BTES are already installed in practice, further methodical investigations are necessary. Especially when high temperatures are applied, characterising the effects such as coupling between thermal and hydraulic processes is crucial. Furthermore, investigating thermal impact of BTES has to be done systematically with respect to subsurface properties and storage settings. Only then, the required reliable prognoses of storage characteristics are possible for planning the energy system. With respect to these aspects of BTES in the subsurface and based on the current state of research, the following research aims are investigated in this thesis:

- Assessment of the coupled thermal and hydraulic processes that are induced by high-temperature heat storage
- Development of a modelling approach to assess effects induced during high-temperature BTES using scenario simulations
- Quantification of achievable capacities such as storable heat amounts and storage rates for various settings differing in terms of subsurface properties and storage conditions
- Establishment of criteria for optimal storage dimensions for designated storage operation conditions and the particular parameterisation at the designated storage site
- Evaluation of thermal impacts of heat storage on the geological subsurface, i.e. magnitude and lateral extent of the temperature distribution induced by heat storage

The assessment of site-specific effects during high-temperature heat storage in a porous formation will be conducted using numerical simulations based on a scenario approach. This requires a setup that allows for identifying significant storage conditions and subsurface properties as well as quantifying their individual impact. For this purpose, an adequate representative scenario of the subsurface, accounting for all technical components as well as subsurface parameters prevailing at a typical North German storage

site has to be developed. On this basis, numerical simulations are performed for identifying the influencing storage processes in the subsurface. The investigations further involve storage performance in terms of storage capacities, rates or efficiency as well as the storage's impacts in the subsurface. This includes induced temperatures inside and around the storage as well as the heat distribution's extent in space and time.

1.4 Structure of this thesis

Following this introduction (Chapter 1), in Chapter 2, the coupled thermal and hydraulic processes induced in the subsurface by heat storage are investigated and quantified. To gain a comprehensive understanding of the ongoing processes near the borehole, a high-resolution model of a singular BHE is used in the simulations that includes all BHE components and is therefore able to represent every aspect of the storage operation. The storage formation in the numerical scenario is chosen to be homogenous to distinguish the particular effects and is parameterized based on realistic Northern German thermal and hydraulic properties from the literature. Special focus is put on the hydraulic permeability of the storage formation as thermally induced convection can occur under certain conditions. The simulations are used to evaluate the heat balances and the dimensions of the induced temperature field under different parameterisation. Because of the high computation times of the scenario simulations, a modelling approach is introduced in Chapter 3. For decreasing computation time, an adapted model is developed and tested for all types of BHE to significantly reduce the discretisation effort while still including all BHE's components. Based on the simulation results of Chapter 2 and with the adapted model developed in Chapter 3, numerical scenario simulations of BTES are performed in Chapter 4 to investigate induced effects and potential storage dimensions heat storage in the geological subsurface. To differentiate and quantify the influence of the various governing factors, the numerical model is parameterised homogeneously based on available literature data. Consequently, different storage scenarios are defined, including variation of BHE number, BHE distance, subsurface thermal parameters and storage operation mode. In Chapter 5, the results of the Chapter 2 to 4 regarding induced thermal and hydraulic impacts as well as optimal storage dimensions are summarized and discussed. The findings are evaluated with reference to the relevance of numerical simulations for assessing and dimensioning heat storage systems.

2 Process study on a single borehole heat exchanger

Subsurface energy storage of high temperature heat in middle deep formations below drinking water aquifers may offer a new possibility of hosting large amounts of energy in the subsurface. An adequate system and process understanding is required in order to predict and assess the complex and interacting induced effects. In this chapter, the near field effects of high temperature heat storage are studied by numerical simulations using a 100 m BHE placed in the shallow subsurface accounting for the detailed geometry of U-pipes, grout, borehole and soil. Coupled thermo-hydraulic simulations show that the simulated system may store up to 90 MWh of thermal energy using an injection temperature of 90 °C, and that the temperature evolution with time is strongly dependent on the radial distance from the borehole and the soil permeability and sensitive to the thermal conductivity of the grout material. At low soil permeability, heat transfer is controlled by conduction and the amount of heat stored is mainly influenced by the soil thermal conductivity. A higher soil permeability leads to convection in the soil with a doubling of the stored heat. In this case, the amount of heat stored is not sensitive to the soil thermal conductivity but to the grout thermal conductivity. The scenario simulations show further that only a small portion of heat can be recovered during heat extraction depending strongly on the soil permeability.

Parts of this chapter are published as:
Boockmeyer A, Bauer S (2014) High-temperature heat storage in geological media: high-resolution simulation of near-borehole processes. Geotechnique Letters 4:151-156 doi: 10.1680/geolett.13.00060

2.1 Introduction

Transition of energy supply from fossil sources to renewable energy sources is seen as an option for mitigating climate change effects and preparing for a future of sustainable energy supply (IEA 2013). Increasing use of energy from fluctuating sources such as wind power or solar power plants however requires storage of energy on different scales in terms of energy stored and storage time. The ANGUS+ research project aims at evaluating the storage capacity and the impact of the individual storage options on the subsurface and at quantifying and assessing the induced hydraulic, thermal, mechanical, and geochemical effects for typical storage sites (Bauer et al. 2013b).

One potential new storage option in the geologic subsurface investigated in this manuscript is the high temperature heat storage in middle deep formations. The heat is transferred to the ground using BHEs. Possible high temperature subsurface storage formations for seasonal heat storage of up to 100 °C are located in greater depths up to about 1500 m and below fresh water aquifers, as regulations do not allow temperature changes of more than a few degree C in these (Hähnlein et al. 2013). However, both the high temperature heat storage in these middle deep formations as well as the use of borehole heat exchangers for this storage type has not been studied and reported in the literature.

BHEs are commonly used for heating and cooling purposes and well described in the literature for shallow low temperature applications (e.g. Florides and Kalogirou 2007, Yang et al. 2010, Vandenbohede et al. 2011). Heat transfer from deep formations to open wells has been studied intensively for deep geothermal applications (e.g. Gérard et al. 2006). Studies by e.g. Signorelli et al. (2007) for shallow and Kohl et al. (2002) for deep settings have shown that a detailed representation of the geometric conditions of the borehole heat exchanger is important for obtaining reliable results of the specific yield and backflow temperature. Besides temperature distribution, storage capacity becomes very important when assessing possible storage formations. No such study has been reported for a detailed numerical investigation of high temperature heat storage in formations of a few hundred meters depth, especially not with reference to the amount of heat stored.

Therefore, to assess the feasibility, storage capacity and accessibility as well as predict the induced effects of high temperature borehole thermal energy storage, a numerical scenario analysis is conducted here to investigate the governing processes. A detailed and realistic representation of the BHE and thus the governing processes is crucial for accurate and reliable model results. This paper therefore presents a detailed numerical model of a double U-tube BHE, accounting for the full geometry of pipe, grout and aquifer, in order to study the governing coupled hydraulic and thermal processes in the

near field of the BHE and quantify the effects induced.

2.2 Methods

Numerical simulation of heat storage through a BHE involves coupled groundwater flow and heat transport. The governing equation of groundwater flow is given by Bear (2007)

$$(nb\rho_w + (1-n)a\rho_w)\frac{\partial p}{\partial t} + \nabla\left(\frac{k\rho_w}{\mu_w}(\nabla p + \rho_w g \nabla z)\right) + Q = 0 \tag{2.1}$$

with compressibilities of solid and fluid a and b [Pa^{-1}], porosity n [-], pressure p [Pa], intrinsic permeability k [m^2], fluid dynamic viscosity $\mu_w(p,T)$ [$\mathrm{Ns\ m}^{-2}$], fluid density $\rho_w(p,T)$ [$\mathrm{kg\ m}^{-3}$] gravitational acceleration g [$\mathrm{m\ s}^{-2}$], depth z [m], and sources and sinks Q [$\mathrm{kg\ m}^{-3}\ \mathrm{s}^{-1}$].

Heat transport in a porous medium includes heat convection and conduction (Bear and Bachmat 1990)

$$c\rho\frac{\partial T}{\partial t} + \nabla(nc_w\rho_w\mathbf{v}T) - \nabla(\mathbf{D}\nabla T) + Q_H = 0 \tag{2.2}$$

where T [K] is the temperature, $\mathbf{v}$ [$\mathrm{m\ s}^{-1}$] is the groundwater transport velocity and Q_H [$\mathrm{W\ m}^{-3}$] are heat sources and sinks. $c\rho$, $c_s\rho_s$ and $c_w\rho_w$ [$\mathrm{J\ m}^{-3}\ \mathrm{K}^{-1}$] are the volumetric heat capacities of porous medium, solid phase and fluid with

$$c\rho = nc_w\rho_w + (1-n)c_s\rho_s \tag{2.3}$$

$\mathbf{D}$ [$\mathrm{W\ m}^{-1}\ \mathrm{K}^{-1}$] is the heat diffusion-dispersion tensor. In the i-direction it is

$$D_i = \lambda + nc_w\rho_w\alpha_i v_i \tag{2.4}$$

with dispersivity and flow velocity in the i-direction α_i [m] and v_i [$\mathrm{m\ s}^{-1}$], respectively. The thermal conductivity of the porous medium λ [$\mathrm{W\ m}^{-1}\ \mathrm{K}^{-1}$] is given by

$$\lambda = n\lambda_w + (1-n)\lambda_s \tag{2.5}$$

where λ_s and λ_w [$\mathrm{W\ m}^{-1}\ \mathrm{K}^{-1}$] are the thermal conductivities of solid phase and fluid.

For low Rayleigh numbers,

$$Ra = \frac{c\rho kl\beta_T\delta T}{\lambda} \tag{2.6}$$

heat transport is conduction dominated, for large Rayleigh numbers heat convection is dominating (Bear and Bachmat 1990).

The governing equations are solved using the simulation system OpenGeoSys (OGS) (e.g. Kolditz et al. 2012). OGS is a process and object oriented numerical code (Kolditz and Bauer 2004, Wang et al. 2009), that solves the governing partial differential equations with a finite element method, which allows for a detailed representation of the geometry of the BHE. OGS is able to handle variable fluid densities and viscosities for solving for groundwater flow coupled with heat transport, but can also include mechanical effects (Watanabe et al. 2012) and geochemical reactions (e.g. Li et al. 2014, Bauer et al. 2012).

2.3 Model setup

Transient high temperature heat storage in the shallow subsurface with an average depth of 50 m in the North German basin is simulated, representing in detail and with high spatial resolution all components of the BHE and the soil in the 3D numerical model (Fig. 2.1 and 2.2).

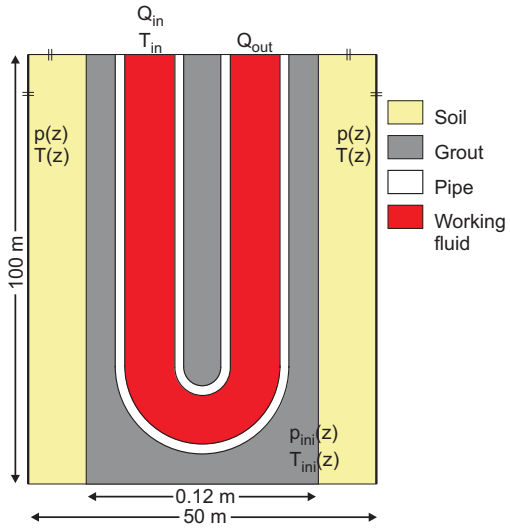

Fig. 2.1 *Schematic illustration of BHE with initial and boundary conditions*

The 100 m long BHE is placed in a depth of 0 m to 100 m. Due to symmetry reasons, only half the model area is simulated. The dimensions of the finite element mesh are 100 m × 50 m × 100 m consisting of a total of 230,000 prism and tetrahedron elements, enabling a high resolution simulation of the ongoing processes. The borehole measures 0.12 m in diameter and includes two U-tubes with an outer tube diameter of 0.03 m and a pipe material thickness of 0.003 m. The spatial discretisation is finest in and around the BHE in order to represent its geometry including the U-pipe and the steep temperature gradients (Fig. 2.2) with high spatial and numerical resolution. For groundwater flow,

the initial pressure distribution is set to hydrostatic pressure $p_{ini}(z)$ and a constant pressure is defined in the upper right corner of the numerical model (Fig. 2.1).

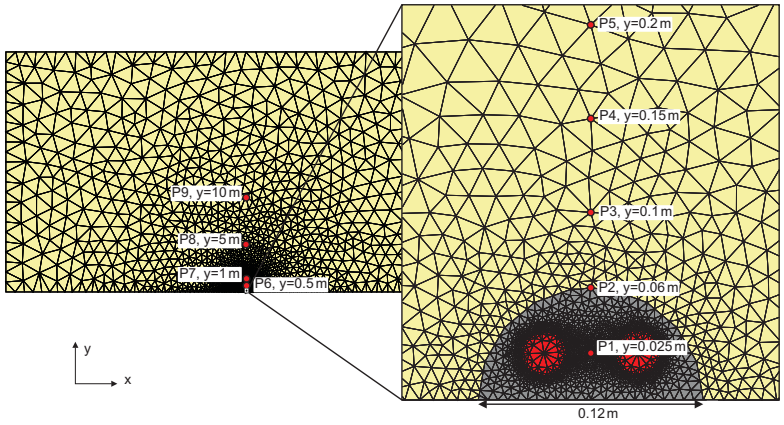

Fig. 2.2 *Top view of finite-element mesh used, with location of observation points and zoom on the near-field of the BHE*

The working fluid is water, and the pipe interior is modelled as equivalent porous medium with a porosity of 0.99 and using a high permeability (Tab. 2.2), while the pipe walls are impermeable for fluid flow. Injection and extraction of the working fluid are controlled by two source terms $Q_{in} = 10^{-3}\,\mathrm{m^3\ s^{-1}} = -Q_{out}$ at the upper model boundary (Fig. 2.1). As flow is controlled by these Neumann boundary conditions, the correct flow velocities and the correct amount of heat transported along the pipe are obtained, even when using the equivalent porous medium assumption. Because the thermal conductivity of the working fluid is higher than of the pipe wall, thermal resistance to heat flow is in the pipe walls and no radial temperature gradient within the pipe at a cross section vertical to the pipe axis is present in the simulations. This represents the fast lateral heat transfer in pipes with turbulent flow. The initial temperature is defined with $T = 9\,^{\circ}\mathrm{C}$ at the upper surface $z = 0\,\mathrm{m}$ and increases with $dT/dz = 0.03\,\mathrm{K\ m^{-1}}$. As a simplifying assumption that is made in this work, all boundaries are closed during the simulation. During the first six months of the simulation, the temperature of the injected working fluid is set to $90\,^{\circ}\mathrm{C}$ at the inlet of the pipe, while the temperature along the pipe and at the outlet is calculated. Extraction of the heat thus stored is performed by circulating cold working fluid with a temperature of $1\,^{\circ}\mathrm{C}$ for the next six months. Since thermal rock properties may vary considerably, the impact of the thermal conductivity as well as heat capacity is investigated by assuming different materials for grout and soil. Also, the rate with which the working fluid is pumped through the

pipes is varied here. A high and a low soil permeability are assigned, representing heat transport in the soil with and without convection, respectively (Tab. 2.1 and 2.2).

Tab. 2.1 *Thermal and hydraulic parameters used in the numerical simulations*

Material	k [m^2]	k_v/k_h [-]	n [-]	λ [W m^{-1} K^{-1}]	$c\rho$ [MJ m^{-3} K^{-1}]
Fluid	2×10^{-6}	1.0	0.99	0.56	4.18
Pipe	2×10^{-18}	1.0	0.001	0.42	1.80
Grout	2×10^{-17}	1.0	0.05	1.50	3.00
Soil	5×10^{-12} (case 1)	0.1	0.20	2.00	2.50
	6.7×10^{-11} (case 2)	1.0			

Values for Tab. 2.1 are taken from VDI 4640 Part 1 (2010), Pannike et al. (2006) and HeidelbergCement (2019). Water density and viscosity are assumed to vary with temperature according to Wagner and Kruse (1998). The water density therefore is 1000 kg m^{-3} at 20 °C, 990 kg m^{-3} at 50 °C and 974 kg m^{-3} at 80 °C. The respective water viscosities are 0.001, 0.0005 and 0.0004 Ns m^{-2}.

Tab. 2.2 *Parameterisation of scenarios with different thermal conductivities and heat capacities of grout and soil as well as pumping rate. Bold values indicate the parameter that is changed*

Scenario	λ_{soil} [W m^{-1} K^{-1}]	$c\rho$ [MJ m^{-3} K^{-1}]	λ_{bent} [W m^{-1} K^{-1}]	Q [L s^{-1}]
1 (Base)	2.0	2.5	1.5	1.0
2	**1.5**	2.5	1.5	1.0
3	**2.5**	2.5	1.5	1.0
4	2.0	**2.0**	1.5	1.0
5	2.0	**3.0**	1.5	1.0
6	2.0	2.5	**1.0**	1.0
7	2.0	2.5	**2.0**	1.0
8	2.0	2.5	1.5	**0.5**
9	2.0	2.5	1.5	**1.5**

2.4 Simulation results

Heat is transported convectively through the pipe controlled by the pumping rate and transferred from the circulating working fluid through pipe and grout into the surrounding soil. Assuming a low vertical permeability (case 1) leads to conductive heat transport in the soil with a Rayleigh number of $Ra = 1$, while convection is induced when increasing the permeability, and therefore the Rayleigh number, by a factor of 100 (case 2).

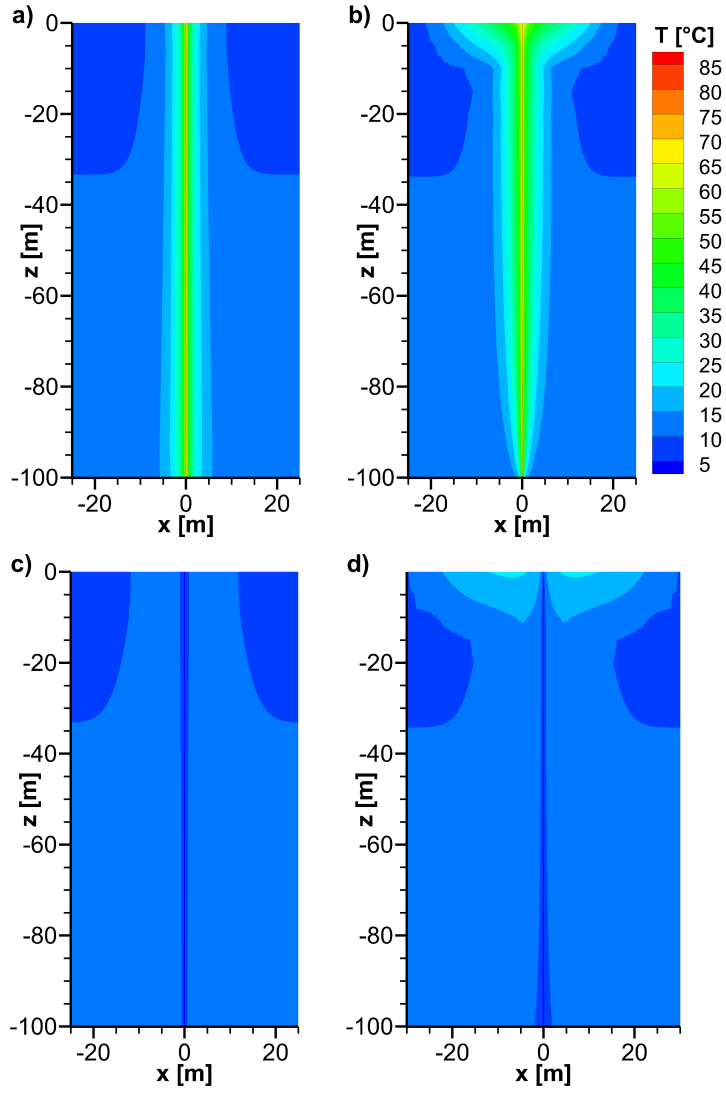

Fig. 2.3 *Temperature distribution in x-z slices. Case 1 (a) and case 2 (b) after six months of heat storage and after six months of heat extraction (c, case 1 and d, case 2)*

The temperature distribution for the base scenario after six months of heat storage is shown in Fig. 2.3 for both cases. For case 1, heat transport is mainly conductive in the soil, resulting in an approximately radial propagate ion of the temperature signal. Due to the natural geothermal gradient, the isotherms are comparatively larger in greater depths (Fig. 2.3 a). The conductive heat transfer results in a temperature spread of 4.5 °C between pipe inlet and outlet after an initial transient phase of a few minutes. This yields a total amount of 93 MWh heat stored within six months at an average of 20 kW through the 100 m long BHE. During the next six months, 23 MWh of heat can be extracted with a temperature spread of 1 °C and an average of 5 kW. The extracted heat fraction (or efficiency) thus is 25 %. Simulation results of case 2 (Fig. 2.3 b) show that convection is induced, causing warm groundwater to rise along the BHE and colder groundwater to flow towards the bottom end of the BHE leading to lower temperatures there. Convection thus increases heat transport from the BHE into the soil, resulting in a temperature spread of 9 °C between pipe inlet and outlet and a doubled heat storage of 172 MWh. However, the amount of heat that can be extracted is only 25 MWh, which is only 15 % of the previously injected heat and therefore 10 % less compared to case 1 (Tab. 2.3).

Tab. 2.3 *Amount of stored and extracted heat with the corresponding extracted heat fraction (efficiency) for the two cases without convection (case 1) and with convection (case 2)*

	Stored heat [MWh]		Extracted heat [MWh]		Fraction [%]	
Scenario	Case 1	Case 2	Case 1	Case 2	Case 1	Case 2
1 (Base)	92.9	172.2	22.6	25.2	24.3	14.7
2	75.9	165.7	19.1	21.3	25.2	12.8
3	108.2	176.7	25.6	28.0	23.6	15.8
4	90.9	170.9	21.9	23.6	24.1	13.8
5	94.6	173.5	23.2	26.6	24.6	15.3
6	89.0	154.2	21.3	23.5	23.9	15.2
7	95.0	183.7	23.4	26.2	24.6	14.3
8	89.1	154.0	21.4	23.6	24.0	15.3
9	94.1	178.9	23.0	25.8	24.4	14.4

Observation points are placed in increasing distances along the y-axis from the BHE in 50 m depth (Fig. 2.2). The arrival (or breakthrough) time of the temperature signal at the observation points in a depth of 50 m increases with increasing distance from the

BHE (Fig. 2.4). In the vicinity of the BHE ($y \approx 0.1$ m) the breakthrough time of the temperature signal equals minutes up to a few hours, while temperature increase takes days to months for distances larger than 0.2 m.

For case 1, temperatures increase to about 85 °C at P1 inside the BHE, 76 °C at the borehole wall (P2) and 69 °C 0.1 m from the borehole centre (P3). Temperature increase takes days to months at distances larger than 0.2 m. At P6 and P7, temperatures have increased to 46 °C and 37 °C, respectively. Temperature increase is smaller than 5 °C at distances larger than 5 m and less than 1 °C at distances larger than 10 m from the BHE (Fig. 2.4 a). In general, temperatures are lower in case 2, and reach near constant values after about three months, when heat flux by vertical convection and lateral conduction become equal. Temperature increase is faster than in case 1 due to heat dispersion (Fig. 2.4 b). Temperature increase is smaller than 5 °C at distances larger than 6 m and less than 1 °C at distances larger than 14 m.

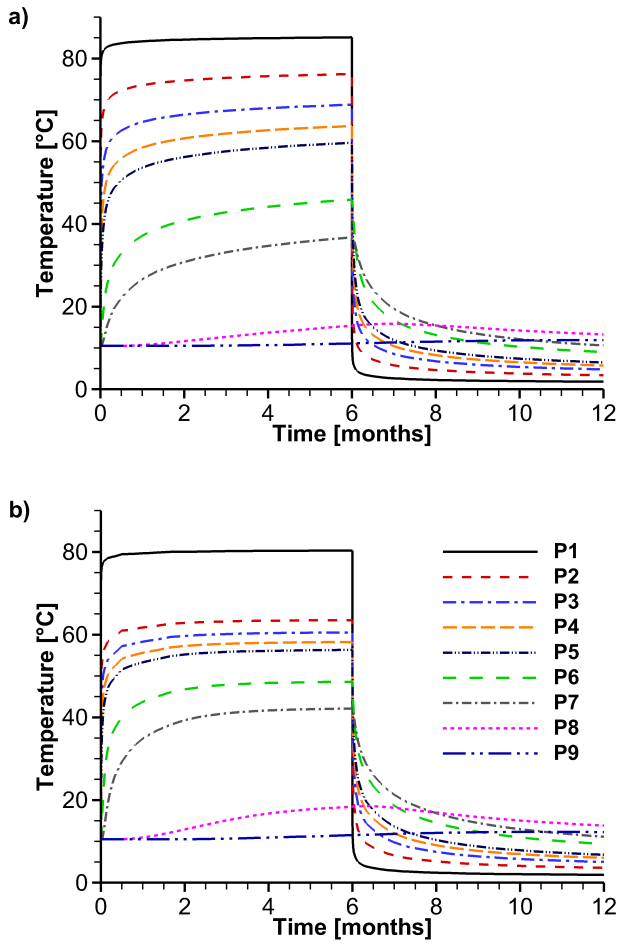

Fig. 2.4 *Temperature breakthrough curves at several observation points (see Fig. 2.2) with increasing distance from the BHE without convection (a, case 1) and with convection (b, case 2)*

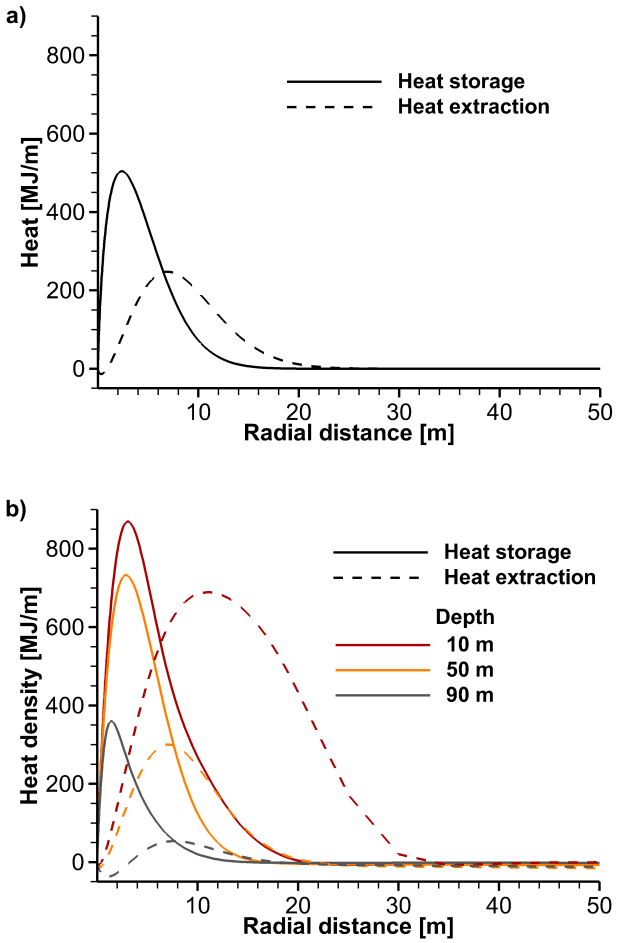

Fig. 2.5 *Radial heat distribution in the soil after each six months of heat storage and extraction without convection (case 1) in a depth of* 50 m *(a) and with convection (case 2) in different depths (b)*

Although the temperature is highest close to the BHE and decreases exponentially with increasing distance from it (case 1 without convection), most of the heat is not stored in accordance with the temperature maximum. The heat spreads radially into the soil and its maximum per metre in radial distance from the BHE is located at 2.5 m where the temperature has only increased to 23.5 °C after heat storage (Fig. 2.5 a). This is because with increasing distance the soil volume affected by the temperature rise increases as well and comparatively more heat can be stored per metre than directly at the BHE. As heat conduction towards the model boundary and extraction towards the BHE are competing processes, the maximum shifts to 7 m during heat extraction where the temperature is still 13 °C. With additional heat convection, the radial heat distribution generally shows the same trend (Fig. 2.5 b). Corresponding to the vertical temperature distribution with its maximum in shallow depths (Fig. 2.3 b and d), more heat per metre is stored in a depth of 10 m than in a depth of 90 m with a maximum

that is almost 2.5 times larger. Compared to the radial profile for case 1, the remaining heat after heat extraction is much higher (i.e. two times, see Tab. 2.3) and most of it is located close to the upper surface.

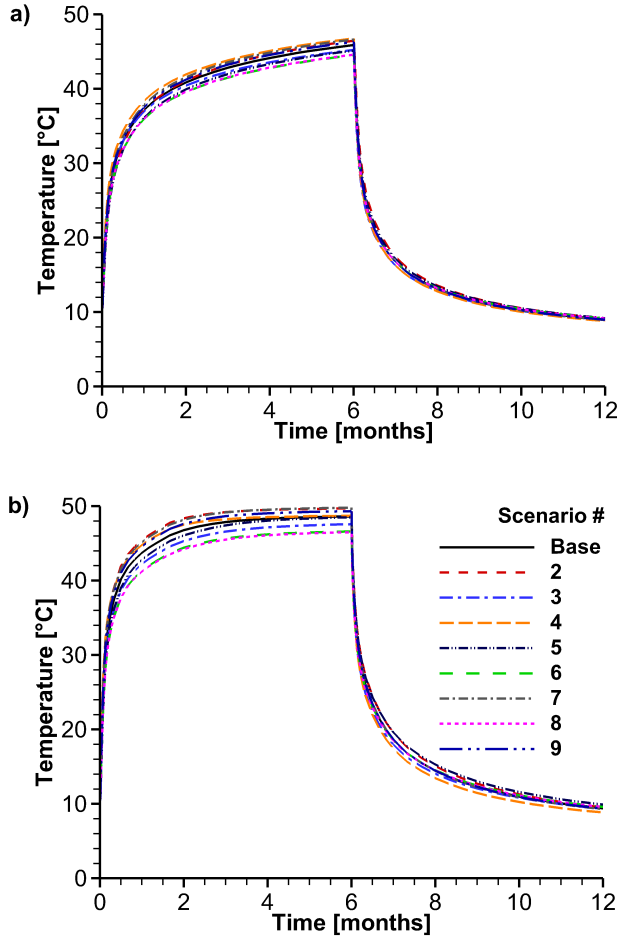

Fig. 2.6 *Temperature breakthrough curves at observation point P6 ($y = 0.5\,\mathrm{m}$) for different thermal conductivities and heat capacities of grout and soil (see Tab. 2.2) as well as varying pumping rate without convection (a, case 1) and with convection (b, case 2)*

Variation of the thermal conductivity of grout and soil shows that temperatures vary only within a few degree C in the vicinity of the borehole (Fig. 2.6). With a smaller soil heat capacity, the temperature is highest in case 1 as less energy is needed to heat up the soil (scenario 4). The temperature is thus 1 °C higher at P6 ($y = 0.5\,\mathrm{m}$) compared to the corresponding base scenario. For case 2, the temperature is 1.5 °C higher compared to the base scenario with a higher grout thermal conductivity that enhances the heat transfer. A grouting material that is not thermally enhanced (scenario 6) reduces the heat transfer, resulting in a 1.5 °C lower temperature for case 1 and a 2 °C lower temperature for case 2 at P6.

While the effect of the soil heat capacity on the amount of stored heat is less than 2 % in case 1, the systems stores 18 % less heat with a lower (scenario 2) and 16 % more with a higher soil thermal conductivity (scenario 3) compared to the base scenario (Tab. 2.3). However, the extracted heat fraction is only marginally effected by the change in thermal conductivity as the amount of heat that can be extracted increases/decreases with the changing soil thermal conductivity too. For grout thermal conductivity and pumping rate, the change in stored heat is less than 5 % and the change in efficiency less than 0.5 % (Fig. 2.7 a).

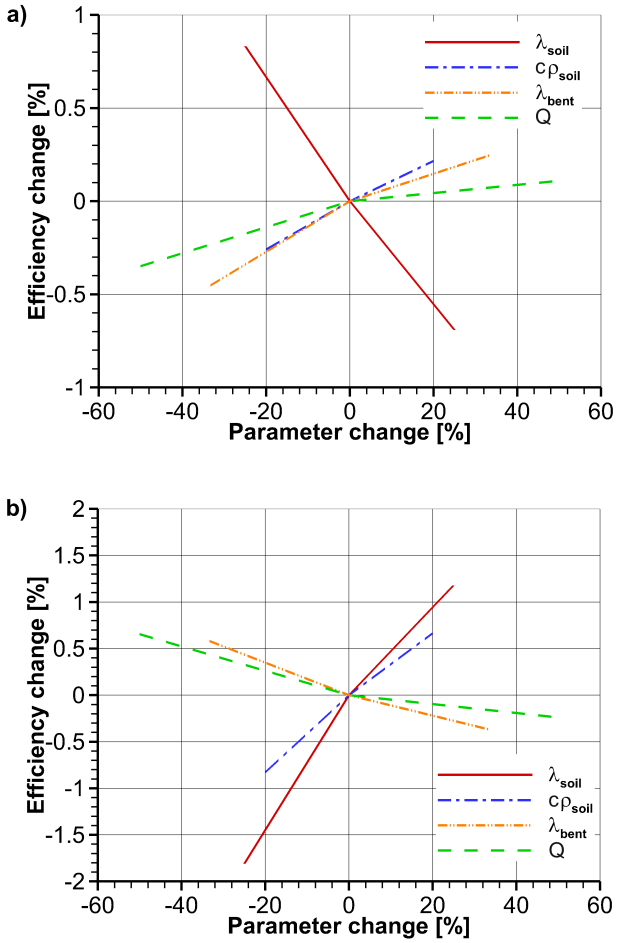

Fig. 2.7 *Change in extracted heat fraction (efficiency) depending on the parameter change for different thermal conductivities and heat capacities of grout and soil (see Tab. 2.2) as well as different pumping rates without convection (a, case 1) and with convection (b, case 2)*

Due to the convection that dominates the heat storage in case 2, the amount of heat stored is only 4 % less and 2.5 % more for a lower or higher soil thermal conductivity, respectively. Also, the extracted heat fraction changes by less than 2 % (Fig. 2.7 b). The effect of the soil heat capacity can be neglected in case 2 as the stored heat varies by less than 1 %. In contrast, the system stores 10 % less heat with a lower grout thermal

conductivity or pumping rate. But still, the extracted heat fraction only changes by less than 1 %.

In this work, geomechanical effects have not been considered. Thermal expansion will cause locally increased pore pressures, which are compensated by fluid flow in the permeable sandy soil, and solid phase expansion, which is small and expected to be compensated by rearrangement of the unconsolidated sandy soils assumed in this work.

2.5 Conclusions

This chapter investigates subsurface energy storage from renewable and fluctuating sources by storing heat at high temperatures in the shallow subsurface. A detailed high resolution numerical model of the borehole heat exchanger, including U-pipes, working fluid, grout and soil, is set up and used to quantify the heat flow rates and temperature effects in and in the near field of the borehole heat exchanger as well as the amount of heat stored. Geometry and material parameters are represented geometrically exact. The model results obtained from this detailed high resolution numerical simulations show that the initial phase of temperature adaptation of the BHE has a time scale of a few days. Temperatures are still changing after six months in case 1 and three months in case 2 for distances greater than about 5 m. Temperature increase for case 1 is less than 1 °C for distances larger than 10 m, representing the area of influence, outside of which induced effects are expected to be small. In case 2, heat transport is driven by conduction and induced convection. That increases the area of influence to 14 m. The impact of the soil thermal conductivity decreases from case 1 to 2, as convection is dominating heat transport in the soil. Doubling of the amount of stored heat from case 1 to 2 shows that convection enhances the heat transfer between the BHE and soil. However, heat extraction and conduction are competing processes and most of the stored heat cannot be regained from the soil. The permeability of the storage formation has to be considered when using high temperatures as induced convection as in case 2 may occur, leading to increased heat transfer and an unfavourable temperature distribution for subsequent heat extraction. Heat is thus additionally transported away from the BHE by convection and even less heat can be regained during six months of heat extraction. This leads to a significantly decreased efficiency of the BHE. Scenario simulations with different parameterisation show that changes in temperature near the BHE and extracted heat fraction are small (less than 2 °C and less than 2 %). In contrast, the total amount of stored heat can vary up to 20 % in case 1 depending on the soil thermal conductivity. This work shows that a detailed representation of the geometry and the governing processes and material parameters is required for a realistic

prediction of the amount of storable heat and the induced effects. The interaction of grout, pipe and soil material parameters as well as the exact geometry of the BHE determine the efficiency of the BHE.

3 Adapted modelling approach for borehole heat exchangers

In this chapter, an adapted model is developed for BHEs to simulate geothermal applications like e.g. heat storage on a large scale efficiently and with high accuracy. The adapted numerical model represents all BHE components, allowing for a detailed representation of the governing processes. The approach is calibrated and validated for a single U-tube BHE using a high-resolution experimental data set from a laboratory thermal response test. It is found that the computational effort can be reduced by factors of ~50, ~50 and ~25 for single U-tube, double U-tube and coaxial BHEs, respectively, if an absolute deviation of less than 1 % compared to a conventional fully discretised model is allowed. Computation times can be reduced further by accepting higher deviations. The adapted modelling approach is shown to allow for a detailed and correct representation of the temporal and spatial temperature distribution under highly transient conditions by applying it to a high temperature heat storage scenario using multiple BHEs. The model is especially suited to represent coupled flow and heat transport processes, to account for groundwater flow in the BHE region as well as geological heterogeneities and especially interaction between a large number of BHEs.

Parts of this chapter are published as:
Boockmeyer A, Bauer S (2016) Efficient simulation of multiple borehole heat exchanger storage sites. Environ Earth Sci 75:1021. doi 10.1007/s12665-016-5773-40

3.1 Introduction

Worldwide, around 70 % of the final energy consumption in residential areas is used for heating and hot water production (IEA 2008). In Germany, it is even more than 80 % (AGEB 2013). Therefore, the use of geothermal energy is seen as a method to reduce the carbon footprint of heating and hot water supply. Borehole heat exchangers (BHEs) are widely used for heat production in urban areas, resulting in high local BHE densities (Vienken et al. 2015). BHEs can also be employed for seasonal heat storage, in order to compensate for the temporally fluctuating renewable energy production. This can either be surplus energy from wind or solar power plants (power-to-heat, Sternberg and Bardow 2015) or from solar thermal plants (Bauer et al. 2010). Especially in combination with solar thermal energy systems, heat is increasingly stored in subsurface heat storages, e.g. in borehole thermal energy storage (BTES) using multiple BHEs. Several pilot storage sites have been installed, e.g. in Crailsheim (Germany), Neckarsulm (Germany) and in Brædstrup (Denmark). These BTES sites store solar thermal energy during summer to provide heat for a residential area during winter. The BTES in Crailsheim consists of 80 BHEs and is operated using maximum inlet temperatures of about 70 °C (Bauer et al. 2009). In Neckarsulm, the BTES consists of 528 BHEs and reaches maximum temperatures of 65 °C (Bauer et al. 2010). The storage site in Brædstrup uses 49 BHEs at the moment but is designed to consist of more than 400 BHEs in the future (Sørensen et al. 2013). These large-scale heat storage sites using high inlet temperatures require dedicated methods to determine storage capacities and heat injection and extraction rates as well as to assess the induced effects in the subsurface. Storage capacities and induced impacts of different geotechnical storage options are investigated in the ANGUS+ research project for typical storage sites (Bauer et al. 2013b, Kabuth et al. 2017), to gain a priori knowledge of these different options. Storage capacities and impacts of heat storage are evaluated by experimental work (Lienen et al. 2017) and numerical scenario simulations (e.g. Bauer et al. 2015, Popp et al. 2015, Popp et al. 2016, Beyer et al. 2016). For this end, efficient simulation methods are required, which allow a prognosis of the storage characteristics and induced effects. These methods have to account for the geometrical set-up of the BHEs and the multi-BHE sites, in order to calculate correctly the mutual influences of the BHEs on each other as well as represent the coupled induced processes during heat storage and retrieval.

Simplified analytical solutions exist. They approximate BHEs as infinite or finite line sources (e.g. Carslaw and Jaeger 1959, Eskilson 1987, Molina-Giraldo et al. 2011, Rivera et al. 2016), cylindrical sources (e.g. Ingersoll et al. 1954, Carslaw and Jaeger 1959) or as a single pipe surrounded by a concentric ring of grout (composite model; e.g.

Shonder and Beck 1999, Javed and Claesson 2011, Beier 2014). Analytical solutions are principally used for interpretation of thermal response tests (Sass and Lehr 2011, Li and Lai 2012, Zhang et al. 2014, Poulsen and Alberdi-Pagola 2015) and to a lesser extend for large-scale applications. Introducing simplifying assumptions, analytical solutions can for example account for either interaction of multiple BHEs (e.g. Beck et al. 2013, Bayer et al. 2014, Cimmino and Bernier 2014), spatial heterogeneities (e.g. Abdelaziz et al. 2014, Schulte et al. 2016b) or vertical heat transport inside the storage formation (e.g. semi-analytical solutions by Bandos et al. (2009) or Rivera et al. (2015)). Geometric dimensions of the BHE's components and their parameterisation or temperature dependencies of the storage formation parameters have to be neglected. Only 3D numerical models, which either use a dual continuum approach or fully discretise the BHE, can correctly predict the temperature distribution for large-scale applications with interacting BHEs in a heterogeneous storage formation. A dual continuum approach was first introduced by Al-Khoury et al. (2005) and Al-Khoury and Bonnier (2006) and was further extended and adapted by Diersch et al. (2011) and Hein et al. (2016). This approach represents the BHE as 1D elements - designed to mimic fluid flow and heat transport in the installed system - that are coupled to the surrounding 3D storage by mathematical relations. For obtaining accurate and reliable transient temperature distributions in the vicinity of the BHE and thus allowing for an accurate representation of the temperature-dependent coupled processes, a detailed representation of the borehole geometry is still necessary. Fully discretised 3D numerical models account for all BHE components and explicitly simulate flow and convective heat transport of the heat transfer fluid in the pipes as well as conductive heat transport in the impermeable components, i.e. pipe walls and grout. They can be used for simulation of either large-scale applications or for thermal response tests in complex geologic settings (e.g. Kohl et al. 2002, Signorelli et al. 2007, Marcotte and Pasquier 2008, Wagner et al. 2012, Boockmeyer and Bauer 2014). These models require a fine discretisation, especially inside the BHE with the small given geometry of the U-tubes or coaxial pipes, the pipe interiors and the grout, but also in the aquifer close to the BHE. The computational expense is correspondingly large due to the high number of computational mesh nodes required. Therefore, adapted versions of fully discretised BHE models are required, which still allow for an accurate representation of the governing coupled processes. The adapted model represents the BHE geometry and the near BHE region in detail, but reduces the computational burden to enable the simulation of large-scale BHE sites.

Therefore, this chapter presents an adapted modelling approach that ensures efficient numerical simulation of large heat storage or production applications without neglecting required geometrical details and processes. For this, the circular BHE geometry is

converted into an equivalent angular geometry that allows for construction of meshes with a much smaller element number and thus a reduced computational expense. This approach utilizes equivalent thermal conductivities, due to the adapted geometries. The adapted model is validated using data from a high-resolution experiment and an application is shown to demonstrate that using the presented approach on a larger scale is feasible.

3.2 Methods

Three different types of BHEs, single U-tube, double U-tube and coaxial BHEs, exist. Boreholes with single U-tube BHEs consist of one U-shaped pipe backfilled with a grouting material, while boreholes with double U-tube BHEs contain two of these pipes. Coaxial BHEs are pipe-in-pipe systems where an inner pipe is located inside the outer pipe.

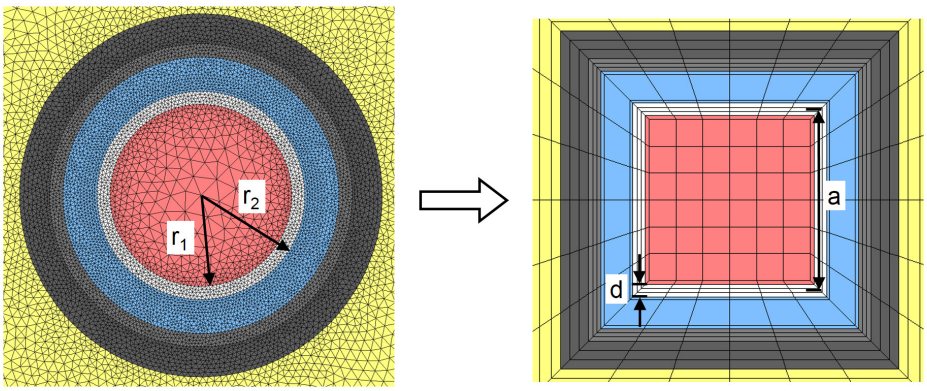

Fig. 3.1 *Principle of adapted modelling approach by example of a coaxial pipe BHE*

An adapted modelling approach to efficiently simulate heat production or storage through BHEs is developed here for all types of BHEs. The aim of the approach is to represent all geometric entities of the BHEs, to be able to represent the governing processes correctly. For this, the element number has to be reduced, which is easier for rectangular geometries than for the circular geometries of the true BHEs. Consequently, in a first step, the BHE geometry is adapted: circular geometries are replaced by rectangular geometries. The volumes of the BHE and of each of its components remain the same for both shapes, which allows using the true volumetric heat capacities of the BHE materials. However, the thermal resistances of the BHE components change due to

the modification of the shape and equivalent thermal conductivities are therefore determined for the rectangular geometries. Subsequently, in a second step, the optimal mesh density is determined based on the geometric simplification, which is identified by mesh sensitivity studies. The principle of the adapted modelling approach is shown in Fig. 3.1 by taking the example of a coaxial pipe BHE. The thermal resistance of a circular shaped pipe or a hollow cylinder is given by

$$R_{th,cyl} = \frac{1}{2\pi L \lambda_{cyl}} \ln \frac{r_2}{r_a} \tag{3.1}$$

where λ [W m^{-1} K^{-1}] is the thermal conductivity of the material and r_1 [m], r_2 [m], and L [m] are inner radius, outer radius, and length of the hollow cylinder, respectively.

The thermal resistance of an angular shaped pipe or a hollow cuboid is given by

$$R_{th,cub} = \frac{d}{2mL\lambda_{cub}} \tag{3.2}$$

with thickness d [m] and mean side length m [m] of the hollow cuboid. The equivalent thermal conductivity of the cuboid is then calculated based on the assumption that cylinder and cuboid thermal resistances are equal

$$\lambda_{cub} = \frac{\pi d}{2m} \lambda_{cyl} \ln^{-1} \frac{r_2}{r_a} \tag{3.3}$$

This determination of effective cuboid thermal conductivities is directly applicable for the pipes of all BHE types and for the grout of coaxial pipes. This allows for a complete representation of coaxial BHEs. However, in the case of single and double U-tube BHEs, the grout geometry is more complex, and a direct approach is not available. The true parameter value of the material provides an estimation of the effective parameter in this case. To increase accuracy, the effective thermal conductivity for the grout of single and double U-tube BHEs can be obtained using parameter estimation methods and by comparing to a conventional fully discretised BHE. For this comparison, a BHE has to be modelled with full geometrical detail, and the effective thermal conductivity is obtained by fitting the results of the adapted model to results from the original model, which is taken as reference. A parameter estimation, however, is not applied in this work, but the original grout thermal conductivity is used in the adapted model.

Numerical simulation of heat storage through a BHE - regarding all BHE components - includes simulation of fluid flow and heat transport inside the heat carrier fluid, heat conduction through the rigid BHE parts and coupled groundwater flow and heat transport in the storage formation.

The governing equation for groundwater flow is given by Bear (2007)

$$(nb\rho_w + (1-n)a\rho_w)\frac{\partial p}{\partial t} + \nabla\left(\frac{k\rho_w}{\mu_w}(\nabla p + \rho_w g \nabla z)\right) + Q = 0 \tag{3.4}$$

with compressibilities of solid and fluid a and b [Pa^{-1}], porosity n [-], pressure p [Pa], intrinsic permeability k [m^2], fluid dynamic viscosity $\mu_w(p,T)$ [N s m^{-2}], fluid density $\rho_w(p,T)$ [kg m^{-3}] gravitational acceleration g [m s^{-2}], depth z [m], and sources and sinks Q [kg m^{-3} s^{-1}].

The heat transport equation for a fully saturated porous medium is (Bear and Bachmat 1990)

$$c\rho\frac{\partial T}{\partial t} + \nabla(nc_w\rho_w\mathbf{v}T) - \nabla(\mathbf{D}\nabla T) + Q_H = 0 \tag{3.5}$$

where $c\rho$ and $c_w\rho_w$ [J m^{-3} K^{-1}] [J m-3 K-1] are the volumetric heat capacities of porous medium and fluid, T [K] is the temperature, $\mathbf{v}$ [m s^{-1}] is the groundwater transport velocity, $\mathbf{D}$ [W m^{-1} K^{-1}] is the heat diffusion dispersion tensor, and Q_H [W m^{-3}] are heat sources and sinks.

In this work, both λ and $c\rho$ for porous medium are calculated as weighted volume fraction averages of fluid and solid phase properties as a temperature dependency of the thermal parameters is neglected and the relations are simply used to calculate the solid phase properties.

The governing equations are solved using the OpenGeoSys simulator (e.g. Kolditz et al. 2012). This process and object oriented program (Kolditz and Bauer 2004, Wang et al. 2009) employs a finite element method to allow for a close representation of the complex geometries of BHEs.

3.3 Model calibration

The adapted model is first introduced and validated by taking the example of a single U-tube BHE. First, a highly discretised numerical model is set up and calibrated by a reference data set of an experimental thermal response test. Subsequently, the adapted modelling approach is applied to the highly discretised numerical model. Finally, the presented adapted model is validated by the given experimental data.

3.3.1 Original model

A high-resolution numerical model of a horizontal single U-tube BHE is set up (Fig. 3.2 a) and calibrated with comprehensive data from a large laboratory sandbox conducted

Tab. 3.1 *Dimensions and thermal parameters of the experimental sandbox and of both original and adapted numerical models*

Parameter	Experiment	Original	Adapted	Unit
Aluminium pipe diameter	12.6	12.6	11.2	cm
Aluminium pipe thickness	0.20	0.20	0.18	cm
U-pipe diameter	3.34	3.34	2.96	cm
U-pipe thickness	0.30	0.30	0.27	cm
Shank spacing	5.30	5.30	5.30	cm
U-pipe thermal conductivity	0.39	0.39	0.31	W m^{-1} K^{-1}
U-pipe heat capacity	1.62	1.62	1.62	MJ m^{-3} K^{-1}
Grout thermal conductivity	0.73	0.80	0.80	W m^{-1} K^{-1}
Grout heat capacity	3.80	3.80	3.80	MJ m^{-3} K^{-1}
Sand thermal conductivity	2.82	2.80	2.80	W m^{-1} K^{-1}
Sand heat capacity	3.20	2.92	2.92	MJ m^{-3} K^{-1}
Average flow rate	0.197	0.197	0.197	L s^{-1}
Average heat input rate	1056	1013	1013	W

by Beier et al. (2011). The sandbox is 18 m long and 1.8 m × 1.8 m wide. In its centre, an aluminium pipe is embedded horizontally that contains the single U-tube. The space between the U-tube and aluminium is filled with bentonite grout. The dimensions and parameterisation of the experiment and thus the numerical model are listed in Tab. 3.1.

The symmetry of the sandbox allows simulation of fluid flow and heat transport for half of the sandbox only. Although fluid flow is only simulated for the heat carrier fluid inside the U-tube and neglected for pipes and grout, the model accounts for all components of the U-tube. This means, every geometric entity is represented in the numerical mesh and is fully discretised (Fig. 3.2 b, by example of fluid, pipe and grout). The fluid circulation inside the U-tube is explicitly simulated with an average flow rate of 0.197 L s^{-1} controlled by two source terms at pipe inlet and outlet with $Q_{in} = 1.97 \times 10^{-4}$ m^3 $s^{-1} = -Q_{out}$. The temperature of the circulating fluid is calculated along the whole length of the BHE according to the heat input rate, which is defined at the pipe inlet.

Beier et al. (2011) placed thermistors that measured circulating fluid and sand temperatures at different locations in the sandbox along one side of the BHE with increasing

distance to the aluminium pipe throughout the entire time of the experiment (52 hours).

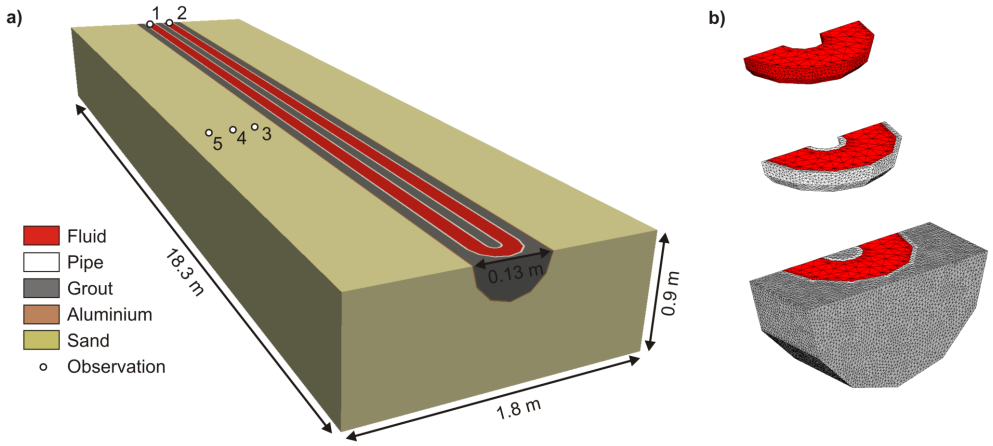

Fig. 3.2 *Conceptual model of the sandbox experiment by Beier et al. (2011) with observation points at pipe inlet (1), pipe outlet (2), and at* 0.24 m *(3),* 0.44 m *(4) and* 0.65 m *(5) away from the borehole (a) and U-turn of the numerical mesh of fluid, pipe, and grout (b)*

The initial temperature in the sandbox is 22.1 °C. During the time of the experiment, the temperatures at pipe inlet and outlet rise significantly to about 39.3 °C at pipe inlet and 38.1 °C at pipe outlet (Fig. 3.3 a).

Due to the constant heating rate, an average shift of 1.3 °C between inlet and outlet temperature is observed throughout the experiment, indicating heat loss of the circulating heat carrier fluid through pipes and grout to the soil. Maximum temperatures of a particular observation point in the sand depend on its distance from the BHE (Fig. 3.3 b). In the vicinity of the BHE, temperatures rise earlier and are comparatively higher. Thus, the maximum temperatures are 24.5 °C, 23.3 °C and 22.8 °C at 0.24 m, 0.44 m and 0.65 m away from the BHE, respectively. Simulation results are compared to the measured temperatures. Although the deviation between simulated and measured curves grows with time at both observation points, it is still within the described measurement uncertainty of ±0.03 °C. The fit between simulation results and experimental data at 0.65 m from the borehole is acceptable with deviations of up to 0.1 °C, while inlet and outlet temperatures do not fit the experimental results as deviations lay between 1 °C and 1.2 °C. These observations lead to the assumption that either the thermal parameters of grout and sand or the calculated heat input rate need to be adapted. To derive

the parameters that give the best fit between simulation results and experimental data, a parameter estimation using the parameter estimation software PEST (Doherty 2015) is done for heating rate, grout thermal conductivity as well as sand thermal conductivity and heat capacity. Within a defined parameter uncertainty range of ±10 %, a unique parameter set is obtained. The resulting values are given in Tab. 3.1. The thermal conductivities of grout and sand given by Beier et al. (2011) are 0.73 W m^{-1} K^{-1} and 2.82 W m^{-1} K^{-1}, respectively with an estimated error of 5 %. The thermal conductivities of grout and sand computed with PEST are 0.80 W m^{-1} K^{-1} and 2.80 W m^{-1} K^{-1}. The computed values deviate by 9.5 % and 0.75 % from the measured values. Considering that the measurement error of 5 % is only estimated, a deviation of 9.5 % is still acceptable, especially as the grout thermal conductivity was measured in a different container.

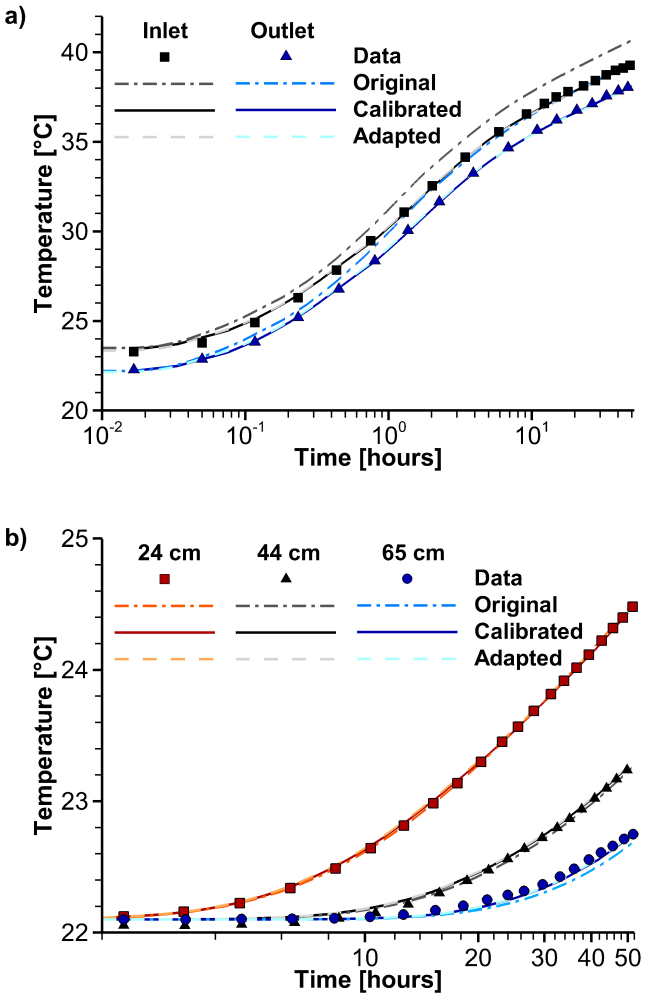

Fig. 3.3 *Measured data (symbols), simulation results conducted with the parameters given by Beier et al. (2011) (dash-dotted lines), with the PEST derived parameters (solid lines) and with the adapted model (dashed lines) at pipe inlet/outlet (a) and at different locations in the sandbox (b)*

Beier (2014) fitted the sand heat capacity to be 3.20 MJ m^{-3} K^{-1} with the analytical solution that was introduced in the paper. The computed value of 2.92 MJ m^{-3} K^{-1} deviates from it by 8.5 %. The heating rate calculated by Beier et al. (2011) is 1056 W with an error of 9.5 %. The estimated heating rate is 1013 W. The deviation of 43 W between calculated and estimated heating rate lies within this error bar. With these estimated parameters, all simulated temperature curves fit the experimental data very well. Deviation between simulated and measured curves are still lower than the reported measurement uncertainty of ±0.03 °C for measurement points at 0.24 m und 0.44 m distance. Differences between simulation results and experimental data at 0.65 m from the borehole are now lower than 0.05 °C, and maximum deviation at pipe inlet and outlet is lower than 0.1 °C. This larger discrepancy may be due to the very detailed geometry, as some differences between experimental set-up and the model on these very small scales are expected and the comparison may become sensitive to the exact position of a temperature sensor (sub-mm scale). This comparison shows that the detailed highly resolved model can be used to simulate the transient and spatial temperature behaviour of a BHE and its surroundings with very high accuracy. Thus, these highly resolved models can be used for comparing and validating computationally reduced models.

3.3.2 Adapted model

For testing of the adapted modelling approach, the previously introduced method is applied to the numerical sandbox model. The geometry of the BHE is adapted, the mesh size is reduced and equivalent thermal conductivities are calculated. The resulting parameters and dimensions are given in Tab. 3.1. Apart from the change in the detailed BHE geometry and the resulting mesh, which is a factor of 50 coarser than the original fully discretised mesh, the same boundary conditions are used as above. The simulation results obtained with the adapted model are again compared to the measured temperatures at pipe inlet, pipe outlet and at three distances from the BHE (0.24 m, 0.44 m, 0.65 m) in the sandbox (Fig. 3.3 a and b). The temperature curves of the adapted model match the experimental data very well. The angular geometry and the coarse mesh cause a minor increase in the deviation of experimental and simulated temperature curves. The maximum deviation at both pipe inlet and outlet is 0.2 °C and thus twice as large as for the original model, while results are the same at all observation points in the sand. The good match of the temperature curves of adapted model and experimental data demonstrates that the adapted model gives accurate results for this metric. The adapted modelling approach is thus tested and successfully validated for the single U-tube BHE.

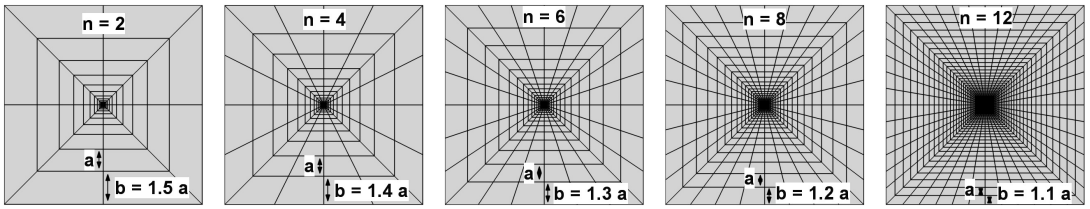

Fig. 3.4 *Illustration of the meshing process. 25 different numerical meshes are tested with different spatial discretisation in radial ($b = 1.5...1.1 \times a$) and angular ($n = 2...12$) direction. Mesh density increases from left to right*

3.4 Adapted models for single U-tube, double U-tube and coaxial BHEs

The computation of heat transfer from the BHE into the storage formation generally strongly depends on the spatial discretisation. Due to the different thermal conductivities of pipe, grout and storage formation, changes in the temperature gradient occur and have to be spatially resolved correctly, in order to simulate the correct temperature distribution and heat fluxes. An inadequate discretisation can overestimate as well as underestimate heat flow from the BHE to the storage formation. Generally, simulation results are more accurate when the spatial discretisation becomes finer. To investigate the influence of the mesh density on the simulation results, the adapted modelling approach is applied to a typical 100 m long BHE embedded in a typical northern German geologic formation. The model dimensions for this scenario are $50\,\mathrm{m} \times 50\,\mathrm{m} \times 100\,\mathrm{m}$. The original highly discretised model with circular shaped BHE consists of prism elements to align with the geometry. Due to the size of the BHE components, the elements are very small ($< 1\,\mathrm{mm}$) inside and directly at the BHE, leading to large mesh sizes of up to 70,000 elements. The thermal and hydraulic parameters for the original model are given in Tab. 3.2, with typical values taken from VDI 4640 Part 1 (2010) and Pannike et al. (2006).

Tab. 3.2 *Thermal and hydraulic parameters used in the numerical simulations*

Material	λ [W m^{-1} K^{-1}]	$c\rho$ [MJ m^{-3} K^{-1}]	n [-]	k [m^2]
Heat carrier fluid	0.56	4.2	-	-
Pipe	0.42	1.6	-	-
Grout	1.50	3.9	0.05	1×10^{-17}
Storage formation	2.00	2.5	0.20	5×10^{-13}

The initial subsurface temperature is $T_0 = 9\,°C$ at the upper boundary ($z = 0\,m$) and increases with depth following a natural geothermal gradient of $dT/dz = 0.03\,K\ m^{-1}$. The initial pressure distribution is assumed to be hydrostatic and remains constant in the storage formation throughout the simulation run (i.e. groundwater flow does not occur). For the simulation, fluid flow and heat transport boundary conditions are defined. The fluid flow rate inside the pipe is set to 1 L s-1 by defining source terms at pipe inlet and outlet. It is assumed that the inlet temperature is constant at $T_{in} = 90\,°C$ during the operation time of six months. The geometry of the BHE is adapted according to the presented scheme (Fig. 3.1) and effective thermal conductivities for pipes of all BHE types and grout of the coaxial pipe BHE are calculated. To attest the suitability of the numerical mesh, simulations are performed for 25 numerical meshes with different spatial discretisation in radial and angular direction (Fig. 3.4).

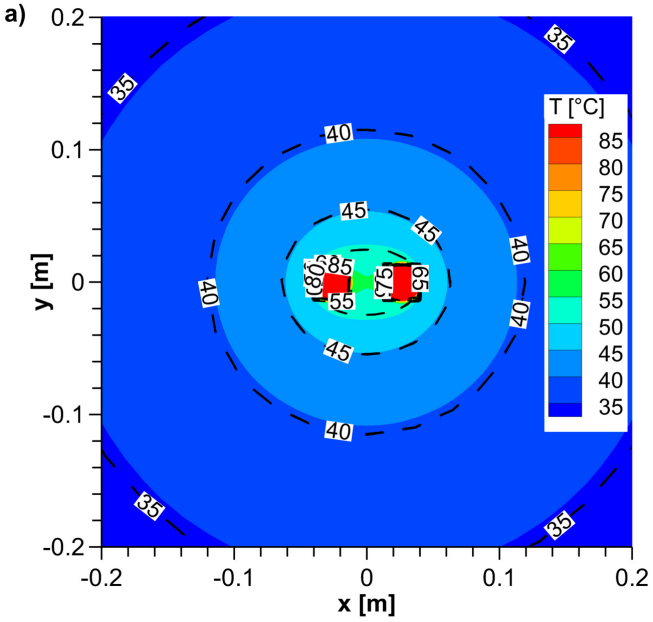

Fig. 3.5 *Horizontal temperature distribution in a depth of* 50 m *at the end of the simulation. Full contours show results of the highly discretised model, dashed lines represent the adapted numerical model*

3.4.1 Single U-tube BHE model

The differences between results from the original highly discretised numerical model with circular geometry and results from the adapted model are evaluated by comparing spatial temperature distributions and the heat balance. Additionally, the mesh size as number of elements and the simulation time are evaluated. Fig. 3.5 shows one example of the simulated horizontal temperature distributions of original and adapted model at

a depth of 50 m. The numerical mesh of the adapted model consists of 18,000 elements, compared to 530,000 of the full model, i.e. a reduction by a factor of 30 (Fig. 3.6).

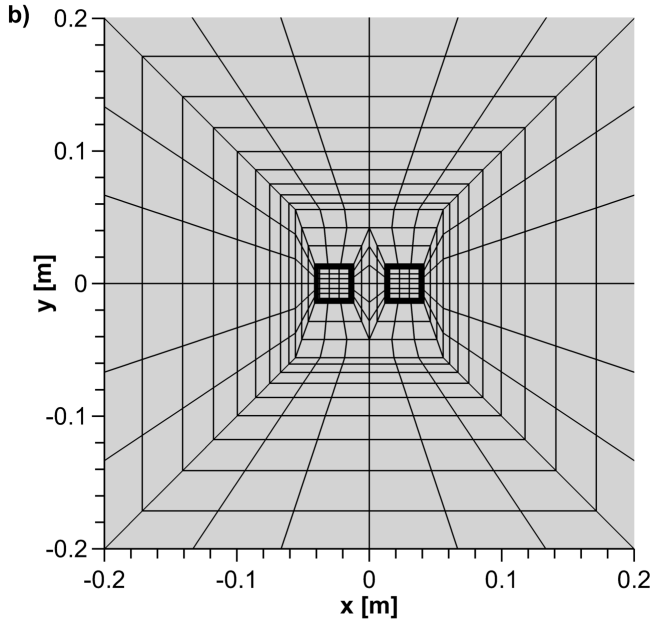

Fig. 3.6 *Numerical mesh of the adapted model*

The temperature spreads radially into the storage formation as no groundwater flow takes place. Simulated temperatures of both models match very well for radial distances larger than the borehole diameter. At the borehole wall, the temperature deviation is already only 0.4 °C and drops further with increasing distance from the BHE. In a distance of 1 m the deviation is 0.15 °C and it is 0.05 °C at a distance of 3 m from it. Only for isotherms 50 °C and larger, which are located inside the BHE, the temperature distribution is controlled by the angular shape of the BHE in the adapted model. The deviation is found to be highest between the two pipes, reaching up to 18 °C. However, this deviation is only local and does not influence the heat transfer rates from the BHE to the storage formation. During half a year of heat loading, 52.731 MWh and 52.381 MWh of heat are stored for the case of the original and the adapted model, respectively. The deviation in heat balance between the two models is therefore −0.66 %.

To quantify the effects of the adapted models, the heat balance is used, as this integral measure is sensitive to small temperature changes. The heat balance deviation between the original highly discretised model and the adapted model is therefore calculated for each adapted mesh and plotted against mesh size and fraction of computation time needed by the adapted model as compared to the original computation time, i.e. the inverse of the computation speedup (Fig. 3.6).

In general, the deviation in heat balance decreases with increasing mesh size (i.e. number of elements (Fig. 3.7 a)), as a finer spatial discretisation results in a more accurate representation of the temperature gradients in the numerical model. However, while at first the adapted model overestimates the amount of heat that can be stored, it underestimates it for higher mesh densities. This negative heat balance deviation is caused by the error from using the original grout thermal conductivity. The relation between heat balance deviation and fraction in computation time shows the same trend (Fig. 3.7 b). The maximum error of 1.8 % corresponds to an adapted model consisting of 6,000 elements and a computation time fraction of about 1 %. As the mesh size of the adapted model rises to 10,000 with an increase of computation time fraction to 2 %, the heat balance deviation drops considerably to around 0 %. The heat balance deviation decreases to −1.4 %, if the mesh size and thus the computation time fraction is increased further. This shows, that an adapted model can be found for a given required accuracy for the case of the single U-tube BHE and that the error caused by the grout thermal conductivity can be compensated by the right mesh density.

3.4.2 Double U-tube BHE model

In case of the double U-tube BHE model, again 25 numerical simulations are performed using different meshes. The results are then compared to the results of the original highly discretised numerical model with circular geometry in terms of heat balance deviation and computation speedup.

The results follow the same pattern as the results of the adapted single U-tube BHE (Fig. 3.7). The heat balance deviation decreases with growing element number (Fig. 3.7 a) reaching about 3.1 % for an element number of 8,000 and 0 % when the mesh size is around 26,000. Compared to the results of the adapted single U-tube BHE the element number is generally higher but the heat balance deviation drops more quickly. Still, more elements are needed for discretisation of a double U-tube BHE due to its more complex geometry. While the simulation time rises due to the increasing mesh size, the heat balance deviation decreases (Fig. 3.7 b). Compared to the trend line of the single U-tube BHE, the trend line of the double U-tube BHE model shows almost the same behaviour with minimum discrepancy, i.e. the adapted model is equally accurate for a double U-tube BHE when the resulting speedup is the same. The results of original and adapted model deviate by around 2.5 % under the condition that the fraction in computation time of the adapted model is 1 % (the adapted model is 100 times faster), and by 0 % when the computation time fraction is 2.5 % (speedup of 40).

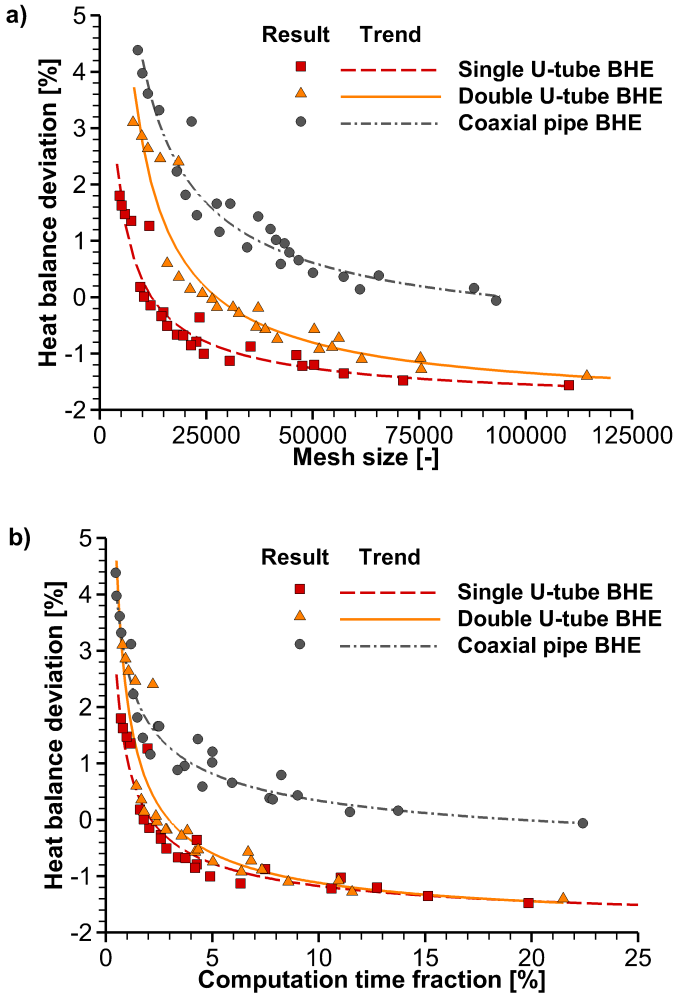

Fig. 3.7 *Calculated heat balance deviation between original and adapted numerical model and corresponding trend line over mesh size (a) and computation time fraction (b) that was needed by the adapted model compared to the original model*

3.4.3 Coaxial pipe BHE model

In contrast to the setup of a single or double U-tube BHE, the components of a coaxial pipe BHE, including the grout, are characterized by a radial geometry. Therefore, effective thermal conductivities can be calculated for all components according to Eq. 3.3. As for the two other BHE types, simulation results are computed for different meshes and then compared to simulation results of the original highly discretised coaxial pipe BHE model (Fig. 3.7 a). For the coaxial pipe BHE, the heat balance deviation is around 4 % for element numbers of around 10,000. Compared to the trend lines of other BHE types, the heat balance deviation shows the same behaviour but is always positive because the grout thermal conductivity is not underestimated as it is for single and

double U-tube BHE. Therefore, larger meshes are needed to reach similarly accurate heat balances and an error of 0 % is never achieved. Again, the relation between heat balance deviation and fraction in computation time shows the same trend (Fig. 3.7 b). The heat balance deviation between original and adapted model is about 3 % and less than 1 % for speedups of 100 and 30, respectively. Considering a fraction in computation time of 5 %, the heat balance deviation is about 0.6 %. To obtain the same speedup, the heat balance deviation is around −0.8 % for single and double U-tube BHE models.

Results for all three types of BHEs show that, in all cases, an adapted model can be configured for a given accuracy, which yields model results within a given tolerance with a reduced computational effort in terms of both computer storage demand and computational time. Computational times can thus be reduced by factors of 20 to 50 for an individual BHE with only very small losses of accuracy. Moreover, a parameter estimation of the grout thermal conductivity is not necessary for single and double U-tube BHE, as the right mesh density can compensate errors caused by underestimating this parameter. This approach thus makes the simulation of sites with many BHEs and multi-BHE sites feasible.

3.5 Application example

The introduced adapted modelling approach can be applied to numerical scenario simulations to investigate induced effects in the subsurface during seasonal heat storage in a BTES. In the presented storage scenario, heat is injected at high pipe inlet temperatures of 90 °C and extracted at low temperatures of 10 °C through 19 BHEs. Initially, the temperature in the model domain is 9 °C at the upper boundary and increases with depth by the geothermal gradient of $dT/dz = 0.03\,\mathrm{K\ m^{-1}}$. As a simplifying assumption that is made in this work, all boundaries are closed during the simulation. Ten storage cycles are simulated; each consisting of half a year of heat injection at 90 °C and half a year of heat extraction at 10 °C. During heat injection, the inner pipe of the BHE functions as the inlet with constant temperature boundary condition ($T_{in} = 90\,°\mathrm{C}$), while the annular pipe is run as inlet during heat extraction ($T_{in} = 10\,°\mathrm{C}$). This means, that the fluid flow direction in every BHE is reversed after each heat injection/extraction period. The absolute value of the flow rate, however, remains constant throughout the ten years of heat storage with $|Q| = 2.5 \times 10^{-3}\,\mathrm{m^3\ s^{-1}}$.

The BTES is composed of 19 parallel connected coaxial pipe BHEs, each with a length of 100 m. The distance between each BHE is 5 m. Hence, the overall diameter of the storage is 20 m. The total model area is 160 m × 160 m × 150 m, but due to the symmetry of the model setup and stagnant groundwater flow conditions in the storage formation,

the simulated model domain can be reduced to a quarter model. For the definition of the BHE geometry and parameterisation of the numerical model identical parameter values are used as for the adapted individual coaxial pipe BHE (Tab. 3.2). The spatial discretisation of the storage formation is finest between the BHEs with $\Delta x = 0.4\,\mathrm{m}$ and is coarsened with increasing distance from the BTES. In total, the numerical mesh consists of 195,000 elements. Compared to a highly discretised numerical model of this BTES setup, which tests whether the adapted model also works for large applications, the computational node number is reduced by a factor of 3.5. Due to the transient behaviour of the BHE, at the beginning of storage and recovery 60 time steps with increasing size are needed to correctly map the step temperature rise and fall. The computation time is 75 s per time step with the adapted model, corresponding to a speedup of 4.5 in comparison to the original numerical model. The speedup is smaller by a factor of 7 compared to the adapted model of an individual BHE with the same mesh structure because for the storage scenario, many elements are needed where the discretisation is controlled by the distance between the BHEs and the given mesh structure.

The horizontal temperature distribution in the BTES after one, four and ten years of heat storage shows, that the imposed temperature signal is highest in the vicinity of the individual BHEs and propagates radially into the storage formation through heat conduction (Fig 3.8 a). This results in a horizontal temperature gradient towards the model domain boundaries. Inside the storage, the temperatures are around 82 °C directly at the BHEs. Halfway between the BHEs they rise from $50 - 55\,^{\circ}\mathrm{C}$ after the first heat storage to $58 - 63\,^{\circ}\mathrm{C}$ and $60 - 64\,^{\circ}\mathrm{C}$ after the fourth and tenth heat storage cycle. Outside the BTES, the temperature drops rapidly. At a distance of 1 m from the outer BHEs, the temperature is only 44 °C, 52 °C and 55 °C after the first, fourth and tenth heat injection, respectively. During heat extraction, the temperature gradient is partially reversed, as the temperature is lowest close to the BHEs (Fig. 3.8 b). At greater distances from the BTES, however, heat still propagates outwards, as gradients at larger distances from the BHEs are not reversed. The temperature profiles at a depth of 50 m through the BTES show the same trend as the temperature distribution of the whole model domain after the first, fourth and tenth heat storage/recovery period (Fig. 3.9 a). The temperature profiles also show that the temperature maximum remaining after heat extraction is located slightly outside the storage site at about 15 m and remaining temperatures there grow with number of storage cycles. Both, original and adapted numerical models produce the same temperature trend and only show minor differences in the range of 0.2 °C between the BHEs inside the storage and less than 0.01 °C at a distance of 1 m from the outer BHE (comparison not shown).

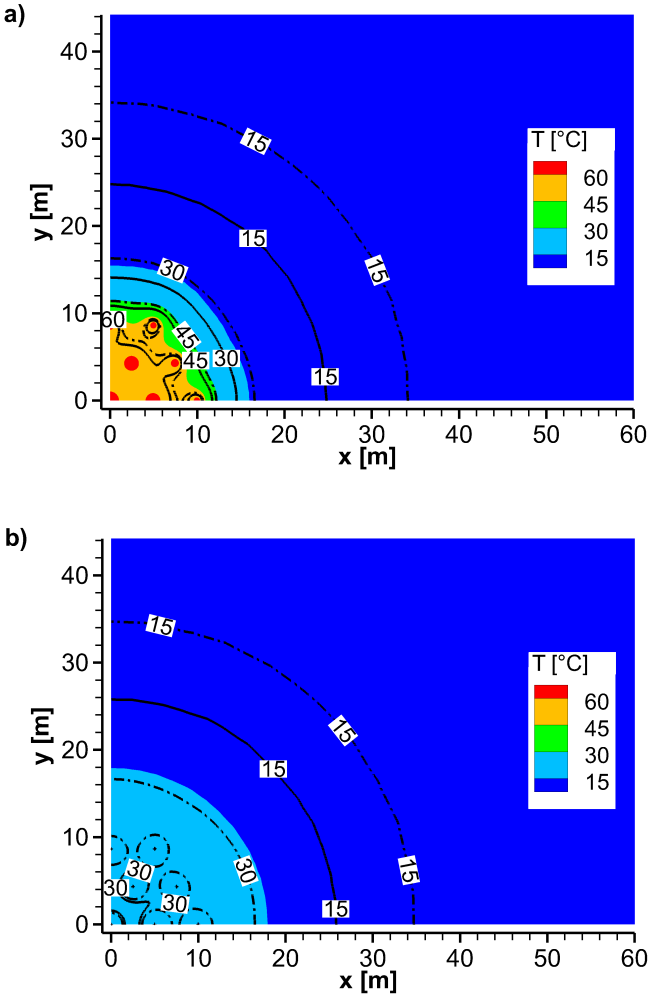

Fig. 3.8 *Horizontal temperature distribution after 1st (full contours), 4th (solid lines), and 10th (dash dotted lines) heat storage (a) and heat recovery (b)*

Temperatures are defined at the pipe inlets and calculated at the corresponding pipe outlets for each BHE (Fig. 3.9 b, by example of the centre BHE #1 and an outer BHE #8). While heat is transported by conduction and convection by the heat carrier fluid inside the pipes, heat is transported by conduction only through pipes and grout into the storage formation. Therefore, the temperature decreases along the length of the pipe during heat storage, resulting in a temperature spread between pipe inlet and outlet. During heat recovery periods, heat is transported from the storage formation to the BHE, leading to a temperature increase along the pipe. After the first ten hours of heat storage, the temperature difference between pipe inlet and outlet has decreased to $|\Delta T| = 12\,°\mathrm{C}$. It reduces further from $|\Delta T| = 6\,°\mathrm{C}$ after ten days of heat storage to $|\Delta T| = 2.5\,°\mathrm{C}$ in the centre BHE and to $|\Delta T| = 3.5\,°\mathrm{C}$ in an outer BHE, respectively. The amount of heat stored is proportional to this temperature

difference. Thus, more heat is stored through an outer BHE than through the centre BHE, which has also been observed by Bayer et al. (2014) for example. For heat recovery, the temperature difference after half a year is less than during heat injection with $|\Delta T| = 1.3\,°C$ and $|\Delta T| = 0.9\,°C$ for the centre and an outer BHE, respectively. In total, the amount of heat stored and retrieved is about 1500 MWh and 660 MWh after the first and 1100 MWh and 850 MWh after the tenth storage cycle. Compared to the highly discretised numerical model, these values are only 0.5 % smaller. This shows that both an accurate temperature distribution outside the BHEs as well as correct heat balances are obtained with the adapted model.

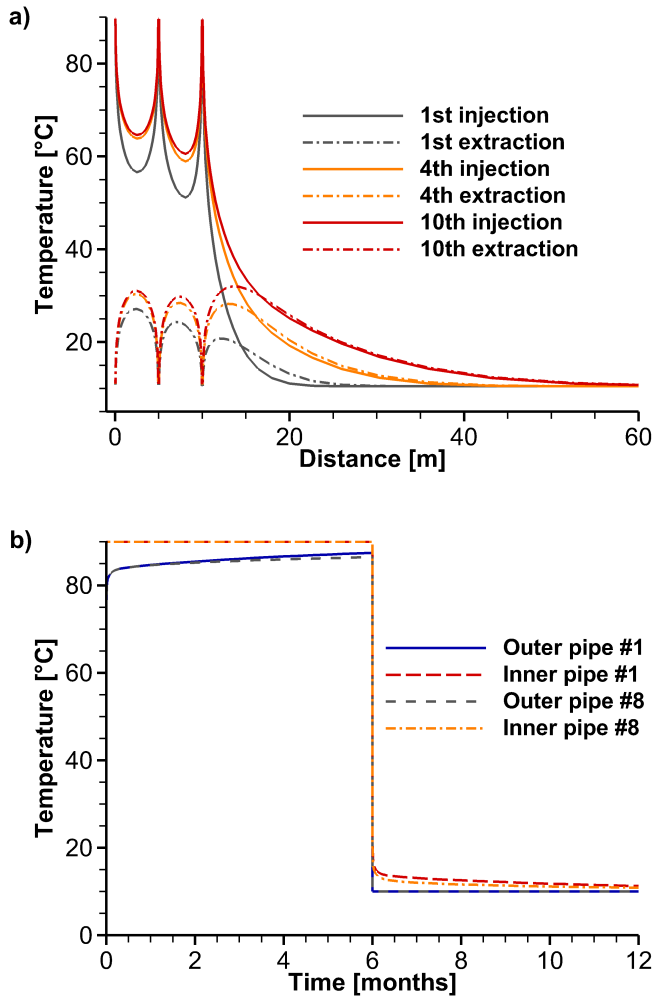

Fig. 3.9 *Temperature profile after 1st, 4th, and 10th heat storage/recovery (a) and temperature curves at pipes inlets and outlets of the centre BHE #1 and an outer BHE #8 (b)*

To quantify how much of the injected heat can be recovered, the fraction of recovered heat is calculated for each storage cycle by $\eta = H_{in}/H_{out}$, where H_{in} is the amount

of heat stored within the heat storage time of half a year and H_{out} is the regained heat during the following half a year of heat extraction. In the application example, the heat recovery ratio increases with number of storage cycles, although the amounts of additionally stored heat decreases with increasing number of storage cycles. After one heat storage cycle, heat recovery is 43 %, increasing to 67 % after the fourth storage cycle. After ten years, heat recovery is stable at about 74 %. So in the longer run, a heat recovery of 75 % or higher can be expected. By preloading the heat storage site for a few years before retrieving heat as it is done in practice (e.g. in Neckarsulm, Bauer et al. 2009), this higher heat recovery could be already obtained in the first cycle. Compared to storage sites in practice, the achieved heat recovery is much higher, because of the chosen boundary conditions. With the closed top boundary and such high or low inlet temperatures of 90 °C and 10 °C, the results therefore reflect the best-case scenario.

Thus, not all of the heat injected can be retrieved, i.e. a fraction is lost. The retrievable or stored heat is located inside the area, where temperature gradients point inward during heat extraction. The corresponding radius of maximum temperature increases from about 12 m during the first cycle to about 14 m after the tenth storage cycle, which is 4 m from an outer BHE. Outside this distance, temperature gradients always point outside, even during heat extraction, and thus the heat there is lost. This is reflected by the temperature increase in the storage formation, which is more than 1 °C for distances up to 24 m and 57 m after the first and tenth storage cycle, respectively (Fig. 3.8 a). However, the heat could be retrieved by using longer extraction periods.

The subsurface volume used for heat storage corresponds to $53,000\,\mathrm{m}^3$ after the tenth cycle. Heat extraction is 850 MWh for the tenth cycle, corresponding to a heat storage density of $16\,\mathrm{kWh\ m^{-3}}$. Using the storage formation heat capacity of $2.5\,\mathrm{MJ\ K^{-1}\ m^{-3}}$, an average used temperature difference in the heat storage site of 23 °C is calculated. This represents the average temperature difference in the storage site after heat injection and after heat extraction. Even though injection and extraction temperatures of 90 °C and 10 °C in the BHEs pipes are used, the average temperature difference is only about 23 °C, which compares well to the lines in Fig. 3.8 a.

3.6 Discussion

The introduced adapted modelling approach has shown to decrease computational efforts without neglecting the BHE's components and accuracy of results. Accepting a heat balance deviation of 1 % compared to the original fully discretised models, a reduction in element number of 98 %, 98 %, and 96 % is achieved for single, double U-tube and coaxial pipe BHEs, respectively. This corresponds to a reduction in computation

time by a factor of ~50 for single U-tube BHEs, ~50 for double U-tube BHEs and ~30 for coaxial pipe BHEs. Compared to this, the computation time is even further reduced by a factor of ~100 for single U-tube BHEs, ~80 for double U-tube BHEs, and ~85 for coaxial pipe BHEs, when accepting a heat balance deviation of 2 %. An error of 1 % is typically much smaller than the uncertainty due to uncertain subsurface parameters of the aquifer (VDI 4640 Part 1 2010). This work demonstrates further that efficient numerical modelling of large BTES with multiple BHEs is possible when applying the introduced adapted modelling approach. By using an example storage scenario with 19 coaxial pipe BHEs, it is shown by comparison with a conventional fully discretised model that induced temperature effects are correctly represented and heat recovery rates only deviate by 0.5 % from the original model, while still achieving a reduction in computation time of around 80 % for the given setting.

The adapted modelling approach keeps the BHE's geometric features and numerical accuracy and is able to correctly represent the steep temperature gradients inside and in the vicinity of the BHE where the temperature is highest during heat injection and lowest during heat extraction. Although it is possible, to reduce the computation time of the adapted model significantly compared to the original model, accounting for all details still leads to large numerical meshes and thus to large computation times of several minutes per times step for large-scale application with more than 19 BHEs. This is the main limitation of this approach, especially when storing and regaining of heat only proceeds constantly over hours or days and many time steps are needed. Hence, the achieved absolute computation time is still large and further speedup would be desirable. However, in contrast to simplified approaches like analytical solutions or the dual continuum approach, the adapted model allows for transient simulation of coupled processes in the close proximity of the BHE where those effects will be large. Therefore, temperature dependent processes can be modelled using the presented adapted approach. This includes temperature dependent thermal and hydraulic parameters, thermally induced convection, thermal expansion or geochemical reactions driven by their temperature dependency. With the adapted modelling approach it is possible to account for subsurface heterogeneities such as geological layering or lateral variations, allowing for a thorough interpretation of thermal response tests conducted in such settings. Furthermore, interactions with neighbouring BHEs as typical for geothermal storage sites or in urban areas with high BHEs densities are accurately represented. The adapted model can also account for groundwater flow at the BHEs, and can be readily expanded to be coupled to geochemical models to assess changes in groundwater geochemistry. Hence, the most important advantage of this approach is its capability of combining all abovementioned transient processes in one numerical model that also

includes subsurface heterogeneities.

3.7 Conclusions

Heat transfer from the BHE into the storage formation depends on the interaction of pipe, grout and storage formation and the consequent feedback on the temperature of the heat carrier fluid. Therefore, it is necessary to ensure that all BHE components are considered in the numerical model, with respect to a correct representation of the governing processes. This paper presents an adapted modelling approach for an efficient numerical simulation of all BHE types, which can be employed to simulate thermal response tests, heat production in urban areas with a high number of BHEs in close proximity or for large BTES site applications, like seasonal storage of heat from solar thermal energy systems.

By taking the example of a single U-tube BHE, the highly discretised model and the adapted modelling approach were calibrated and validated using a reference data set from a thermal response test experiment by Beier et al. (2011). Both simulation results were compared to the temperatures measured during the experiment. It was found that the fit between simulation results and experimental data was very good, thus showing heat transfer from the BHE into the sandbox as well as the highly transient temperature distribution inside the sandbox at varying distances to the BHE are simulated very accurately. Despite accounting for all BHE components and thus requiring a fully discretised mesh, the adapted model needs significantly less computation time than the original model (over 90 %). The adapted model is adequately accurate, achieving absolute heat balance deviations of less than 1 % and temperature differences of less than 0.4 °C at the borehole wall. The presented application example shows further that large-scale numerical simulations are feasible with the introduced approach, still precisely predicting temperature distribution and heat balance. While, compared to analytical solutions or dual continuum approach, the computation time is still high for an adapted numerical model on the one hand; it is able to allow for transient simulation of coupled THMC processes on the other hand. Therefore, the adapted model can be used for simulation of multiple interacting BHEs in complex geologic settings accounting for groundwater flow, thermally induced convection or other temperature dependent processes.

4 Dimensioning of borehole thermal energy storage

High-temperature borehole thermal energy systems (BTES) rely on heat conduction for heat exchange between the subsurface and the borehole heat exchangers (BHEs). They are thus suitable for seasonal heat storage in most subsurface settings. Adapting borehole number, length and their geometrical arrangement can scale BTES to fit the required storage capacities and rates, accounting for the subsurface thermal parameters prevailing at the storage site. In this work, achievable storage rates, storable heat amounts and induced temperature changes in the surroundings of the BTES site are investigated under two storage operation modes for 142 different storage scenarios. In the scenarios, storages with BHE numbers varying from 1 to 61 and distances varying between 2 and 8 m are studied in a homogeneous subsurface of various thermal conductivity and heat capacity, covering most realistic storage site settings. Results show, that achievable rates and storable heat amounts strongly vary with thermal conductivity and heat capacity, with this variation depending in turn on the BHE number and distance used. Generally, storage systems with small BHE spacing reach their loading capacity within a few weeks while systems with a large BHE distance of 8 m do not reach their full capacity with a seasonal storage cycle. Thermal conductivity mainly affects the recoverable heat amounts with large BHE distances and the recovered heat fraction with small BHE distances. The heat capacity mostly influences the storage behaviour when the BHE distance is small. Specific heat extraction rates thus range from 40 to 140 W m^{-1}, corresponding to recoverable heat amounts of ~500 to 2,000 MWh with recovered heat fractions between 60 and 85 %. BTES dimensions furthermore mainly control the temperature impact on the surrounding subsurface. Small storage systems show considerably larger temperature fluctuations inside the storage than large systems. Additionally, their range of influence in relation to the storage volume is twice as high compared to large storage systems. For a designated storage time, an optimal BHE distance thus exists, which again is specific for the thermal parameters prevailing at the site. These optimal distances are identified in this work for the variety of subsurface thermal parameters considered. Additionally, it is found that while achievable storage rates and capacities depend on the storage operation, recovered heat fraction is little influenced by the storage operation mode. This work shows that both, achievable rates and storable heat amounts as well temperature effects in the storage site and the near surrounding subsurface can be quantified by using suitable simulation tools.

4.1 Introduction

Seasonal storage of heat is a technology for providing heat during winter by storing surplus energy from primary producers such as solar thermal energy from solar collectors in summer, industrial processes or space cooling (Zhu et al. 2014). Seasonal storage requires large storage capacities and thus large storage volumes. Especially in cities, need cannot be met on the land surface. However, large storage volumes can be provided by the geological subsurface. A suitable technology for this purpose is BTES. Heat storage with BTES is flexible as the system uses multiple BHEs at defined spacings representing the storage volume to store heat in the subsurface. (Pinel et al. 2011). This storage volume can be expanded by increasing the number of BHEs (Rad and Fung 2016). During charging, hot water is circulated through the BHE and heat is transferred to the storage formation by conduction, increasing the storage temperature (Nordell and Hellström 2000). At the end of a heat injection period, temperatures are thus highest. During discharging, the process is reversed. Heat is recovered and temperatures are lowest after heat recovery. For preventing heat loss into the atmosphere, heat insulation on top of the storage is necessary (Mangold 2007).

Heat storage with BTES is a widely applied method. Around 400 systems are estimated to be in operation in Sweden (in 2011); the number of boreholes for heat storage in the Netherlands was about 22,500 in 2007. In other European countries, the numbers are high as well (Gao et al. 2015). Most of the BTES systems described in the literature operate with maximum temperatures below 50 °C, which has been documented as lower bound for high-temperature heat storage (Sanner and Knoblich 1999). From the systems in operation, it can be derived that subsurface thermal properties are given in practice, because the choice of storage location may typically be constrained by the location of the residential or industrial area to be supplied with heat. Common shallow geological formations are sediments with thermal conductivities ranging from 1.0 to 3.0 W m^{-1} K^{-1} and heat capacities from 1.5 to 3.0 MJ m^{-3} K^{-1}. For example, thermal conductivity and heat capacity of a typical Northern German till vary between 1.1 and 2.9 W m^{-1} K^{-1} or between 1.5 and 2.5 MJ m^{-3} K^{-1}, respectively.

Despite the high number of installed BTES systems, scientific research suffers from deficiencies. For an efficient and sustainable use, a thorough characterisation of the BTES site and the storage processes are required. The storage behaviour is determined by the geological subsurface and the thermal parameters found there, the type of use and operation with operation hours, standstill times, and injection/recovery temperatures, which in combination yield the achievable storage capacities and rates but also the subsurface space influenced by the system. Characterisation and dimensioning involving

all mentioned aspects especially in combination with high temperatures, however, is found seldom in the literature. Sensitivity analysis and performance optimisation for a single BHE has been done in many studies already (e.g. Boockmeyer and Bauer 2014, Casasso and Sethi 2014, Sivasakthivel et al. 2014, Esen and Turgut 2015, Pandey et al. 2017, Pu et al. 2017). Nonetheless, these studies are not representative for BTES applications, because storage processes cannot be considered as they are dominated by BHE interferences.

Various studies investigate BHE fields of different BHE number and configuration used for heating only, combined heating and cooling or even for (high-temperature) heat storage. Measurements from field scale experiments like the sites in San Diego, CA, USA with peak fluid temperatures of nearly 90 °C (McCartney et al. 2017, Başer and McCartney 2020) or in Montauriol, France, where maximum fluid temperatures are almost 50 °C (Lanini et al. 2014), can provide the foundation for a better understanding and data for subsequent numerical simulations like the ones described in the following. Rapantova et al. (2016) investigated an existing high-temperature BTES that reaches temperatures of up to 80 °C in its centre with a numerical model. The system consists of 16 BHEs of 60 m length spaced at 2.5 m. They optimised the injected and recovered heat amounts in the BTES system to maximize the recovery ratio based on different storage scenarios. Law and Dworkin (2016) studied the effects of different BHE configurations on the long-term development of subsurface temperatures for different combined heating and cooling applications with numerical simulations. They found that imbalance in heating/cooling loads causes a temperature increase (up to 32 °C in the investigated scenarios) and that each heating/cooling scenario needs a different layout.

A few studies use numerical simulations to understand and characterise BTES systems under different conditions. Catolico et al. (2016) used a validated numerical model to simulate the high-temperature BTES system in Drake Landing, which operates with maximum temperatures of almost 70 °C, and then varied thermal and hydraulic properties. Their findings support the results of Boockmeyer and Bauer (2014, for a single BHE) that recovered heat fraction is more sensitive to subsurface thermal conductivity as it decreases with increasing thermal conductivity and that convection cells form at higher subsurface permeability. Welsch et al. (2016) drew similar conclusions with their numerical study on middle-deep high-temperature BTES using temperatures between 70 and 110 °C. They additionally evaluated the effects of various BHE lengths, numbers and spacings combined as well as the effect of injection/recovery temperatures. They found that recovered heat fraction and specific heat extraction rate increase with higher BHE number and length but decrease with higher BHE spacing. The results

show further that large temperature differences between heat injection and recovery are favourable for all evaluated factors. Nilsson and Rohdin (2019) also used a validated numerical model of an existing high-temperature BTES system in Emmaboda, Sweden for investigating heat storage scenarios with different flow rate and temperature (up to 80 °C) of the working fluid. For each scenario, BHE spacing and depth were varied. They also investigated the effect of subsurface thermal conductivity and recovery temperature on the real storage application. They confirmed the results of Welsch et al. (2016) that BHE spacing is important and that there is a BHE distance enabling maximum recovered heat amount and recovered heat fraction. The difference between heat injection and recovery temperature should be large. In contrast, the influence of thermal conductivity on the results was low, probably because of the low injection temperature (i.e. 40 °C) of the considered scenario.

Thermal interaction between BHEs plays a significant role in BHE fields. This effect has been investigated in several studies regarding heating-only applications where thermally interacting BHEs are unwanted (Signorelli et al. 2005, Koohi-Fayegh and Rosen 2012, Koohi-Fayegh and Rosen 2014, Gultekin et al. 2016, Gultekin et al. 2019). The studies show that thermal interaction increases with number of BHEs and amount of extracted heat. Further, interaction decreases with increasing BHE distance. Thus, large BHE distances are generally favourable to minimize performance loss in heating only cases. However, for heat storage, thermal interactions are essential, so that these studies can only contribute to the general understanding of how neighbouring BHEs behave.

Instead of studying BTES behaviour for better system understanding, most of the research focuses on the optimisation of the BTES system or the BHE field. Several studies target efficiency optimisation, assuming that maximum efficiency is reached when the maximum temperature change is at minimum. For example, for a given energy demand, de Paly et al. 2012 and Beck et al. (2013) investigate energy extraction distribution and BHE arrangement for heating only. Bayer et al. (2014) later optimised the geometric arrangement of a BHE field, initially consisting of 54 BHEs with 6 m distance, for a given scenario of combined heating and cooling. Others optimised heat flux distributions (Retkowski et al. 2015) or even both geometric arrangement and heat flux, aiming at minimum temperatures at the BHE outlet during cooling (Li et al. 2017). Qian and Wang (2014) evaluated the system performance for different heating and cooling loads with different BHE lengths and distances. Schulte et al. (2016a) found an optimal BTES configuration for a given energy demand with focus on medium-deep boreholes. However, these optimisations only focus on system performance.

One possibility to optimise more than just parameter is the multi-objective design op-

timisation. Studies show that this approach is generally feasible and improves the optimisation process (e.g. Gholap and Khan 2007, Sayyaadi et al. 2009, Ndao et al. 2009). Huang et al. (2015) used this method to optimise the design of two existing combined heating and cooling systems, one consisting of 15 heat exchangers and the other of 270 BHEs. Optimisation includes BHE length, BHE number and BHE components for two heating and cooling systems, with regard to installation costs and temperature change in the subsurface. In both cases, optimisation resulted in lower BHE number with greater length. Subject of all these optimisations are heating and cooling applications that aim at balancing heat amounts. In contrast to BTES systems storing heat for later use, with these applications, heat arising from building cooling during summer is used to regenerate subsurface temperatures after heat extraction in winter. Therefore, their storage temperatures are more or less balanced and the temperature impact is low compared to a BTES system.

Some studies even optimise the whole district heating system with all their components. Rehman et al. (2017) investigated several district heating systems using BTES under different boundary conditions with temperatures between 40 and 70 °C in Finland. For each system, they individually determined optimal configurations and BTES volumes with respect to the achieved renewable energy fraction. They studied the influence of different BTES parameters on the optimisation result and found that the system performance improves with number of BHEs and BTES volume. Additionally, shallow but wide BTES geometries yield better performance (Rehman et al. 2018). Rosato et al. (2019) performed an optimisation of a solar district heating system with high-temperature BTES with temperatures up to 90 °C in Italy, aiming at saving fossil fuels and operation costs. They also optimised the BTES characteristics including BHE number (with variation of BHE number between 1 and 8 BHEs) as well as soil and grout thermal conductivities. Yet, their studies aim at reducing costs and an investigation of impacts through the high temperatures used is not performed. To sum up, many optimisations have been performed already with different purpose. The optimisations, however, focus on system performance aspects like capacities and barely include thermal impacts. Furthermore, the results were mostly conducted with small BHE number or low temperatures.

An option for achieving high capacities and rates that has been rarely investigated is using high injection temperatures up to 90 °C and thus enabling high temperature differences between BHE inlet and outlet. In combination with low recovery temperatures, high temperature gradients and thus heat storage rates are achieved in the subsurface that enhance heat conduction. Some BTES applications reach higher tem-

peratures (Lundh and Dalenbäck 2008, Rees 2016). The best-known examples for high-temperature BTES systems operating today with the purpose to cover the heat demand of residential areas in winter are located in Crailsheim and Neckarsulm, Germany (Bauer et al. 2009, Bauer et al. 2013b), Okotoks, Canada (Sibbitt et al. 2007, Sibbitt et al. 2012), and Brædstrup, Denmark (Sørensen and Schmidt 2018, Schmidt and Sørensen 2018). Their contribution to the respective heating network mainly depends on the storage volume and the injected heat amount. With large storage volume, larger amounts of heat can be charged and discharged, as shown by example of Neckarsulm. Additionally, large volumes have a smaller surface-area-to-volume ratio compared to small volumes, which reduces heat loss from them. Another factor is the temperature of the heat carrier fluid. Most BTES systems are discharged with comparatively high temperatures around 30 °C. Because of the resulting low temperature gradient between fluid and storage formation, the storage efficiencies are between 40 and 50 %, except for Neckarsulm where a storage efficiency of over 70 % is achieved due to large storage volume. Recoveriy heat at much lower temperatures leads to higher efficiencies, i.e. temperatures of 12 °C are used to discharge Brædstrup BTES, producing a storage efficiency of almost 65 % despite its small storage volume.

These projects show that high temperatures are generally feasible and more efficient. However they disregard thermal impacts. Using high temperatures may be favourable in terms of storage characteristics, but also potentially increases heat losses and thermal impacts on the subsurface. These aspects have to be considered when planning a BTES system to estimate spatial demands (Bauer et al. 2015). As the aforementioned examples show, dimensions of the BTES systems are optimised with respect to recoverd heat amount and recovery degree (or in consequence the necessary installation and operation costs for the heat demand). Temperature impacts or associated space requirements are disregarded in this optimisation process. Since an increase of the number of BTES systems installed can be expected in the future, subsurface spatial planning will become more important and spatial demands will have to be considered in the planning process (Kabuth et al. 2017). This emphasises that there is a need for more investigations that include heat storage impacts especially with high temperatures applied.

Findings of previous research show that there is a demand for systematic studies that combine estimating storage capacities and identifying thermal impacts with their related required space for high-temperature BTES under different conditions. Therefore, it is necessary to systematically evaluate and quantify the individual impact of each factor, before designing a BTES system with respect to the abovementioned aspects. This is valuable for gaining general knowledge about the system behaviour on the one

hand, and for deriving a concept of an optimal storage dimensioning on the other hand. The influence of BTES setting with BHE number and distance, BTES operation cycle and subsurface properties on storage capacities, rates, and on the induced temperature effects in the subsurface is thus investigated in this work for high-temperature storage to characterise the system behaviour as well as quantify impacts and space requirements for subsurface planning. Additionally, with the knowledge of storage characteristics and impacts, this chapter aims at deriving a concept for optimising the BTES layout to find an optimal BHE distance that accommodates conflicting storage aims. Especially with future subsurface spatial planning, temperature impacts will gain more importance in the optimisation process.

In this chapter, these aims are achieved through numerical simulations of 142 different BTES scenarios. In the simulations, a modelling approach is applied that considers all BHE components for a comprehensive representation of the governing processes. High-temperature BTES are investigated by analysing these scenarios with variation of the storage setting. This includes typical subsurface thermal properties of Schleswig-Holstein, typical storage configurations like BHE number or distance as well as storage operation mode (heat injection/recovery cycle). In the investigations, BHE numbers between 1 and 61 are considered to assess how BTES behave and if upscaling of capacities and impacts is possible. However, the focus is set on BHE distances varying from 2 to 8 m in different operation modes for observing how BHEs interact in a (homogeneous) subsurface with different thermal conductivities or heat capacities. Storage capacities with corresponding rates and heat losses as well as thermal impacts are then estimated and compared with each other. Especially determining the subsurface space that is occupied by the storage in terms of both the space that is used and the space where thermal impacts can be expected has to be done when planning a BTES system.

4.2 Methods

Numerical simulation of heat storage through a BHE accounting for all of the BHE's components includes simulation of advective heat transport with the heat carrier fluid, heat conduction through pipe and grout and coupled groundwater flow and heat transport in the subsurface if necessary. In this work, the heat transport in the subsurface is only conductive.

The governing equation for groundwater flow is given by Bear (2007)

$$(nb\rho_w + (1-n)a\rho_w)\frac{\partial p}{\partial t} + \nabla\left(\frac{k\rho_w}{\mu_w}(\nabla p + \rho_w g \nabla z)\right) + Q = 0 \tag{4.1}$$

with compressibilities of solid and fluid a and b [Pa^{-1}], porosity n [-], pressure p [Pa], intrinsic permeability k [m^2], fluid dynamic viscosity $\mu_w(p,T)$ [N s m^{-2}], fluid density $\rho_w(p,T)$ [kg m^{-3}] gravitational acceleration g [m s^{-2}], depth z [m], and sources and sinks Q [kg m^{-3} s^{-1}].

The heat transport equation for a fully saturated porous medium is (Bear and Bachmat 1990)

$$c\rho\frac{\partial T}{\partial t} + \nabla(nc_w\rho_w\mathbf{v}T) - \nabla(\mathbf{D}\nabla T) + Q_H = 0 \tag{4.2}$$

where $c\rho$ and $c_w\rho_w$ [J m^{-3} K^{-1}] are the volumetric heat capacities of porous medium and fluid, T [K] is the temperature, $\mathbf{v}$ [m s^{-1}] is the groundwater transport velocity, $\mathbf{D}$ [W m^{-1} K^{-1}] is the heat diffusion dispersion tensor, and Q_H [W m^{-3}] are heat sources and sinks.

The governing equations are solved using the OpenGeoSys simulator (e.g. Kolditz et al. 2012), a process and object oriented program (Kolditz and Bauer 2004, Wang et al. 2009) that employs a finite element method.

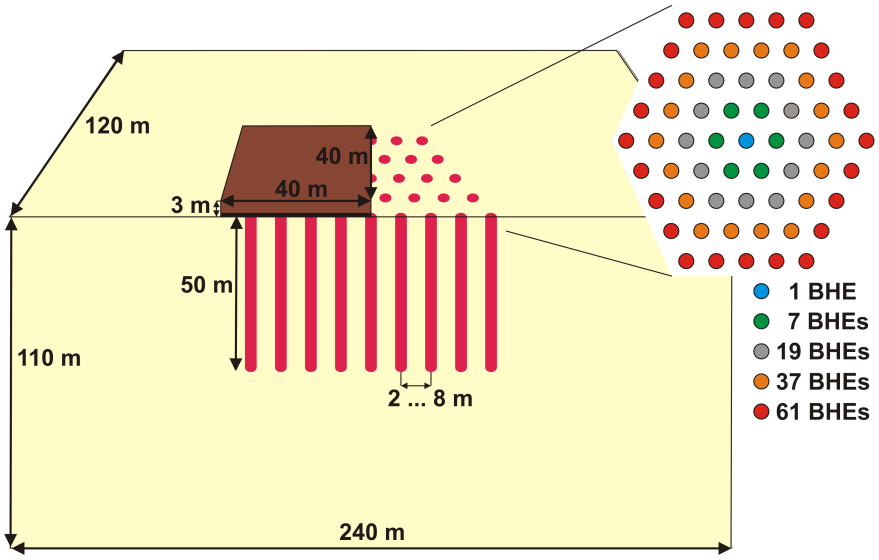

Fig. 4.1 *Half space of the scenario with 61 BHEs and scheme of the top view with BHE number variation*

4.3 BTES setup

Heat is stored in a BTES consisting of 61 parallel-connected double U-tube BHEs with each a length of 50 m. A 0.2 m thick insulating layer and 2.8 m of soil on top of it

thermally insulate the top of the storage (Fig. 4.1). The surrounding subsurface is assumed to be homogeneous with typical thermal parameters that are varied in different scenarios (see 4.4). The thermal parameters for the base scenario are given in Tab. 4.1. For the BHE components, the values are equal those chosen in Chapter 3, the base storage formation is parameterised by taking the mean of the values given for sediments in VDI 4640 Part 1 (2010). Values for insulating and overburden layer are the same as with the Neckarsulm BTES (Nußbicker-Lux 2010).

Initially, the temperature in the model domain is 9 °C at the upper boundary and increases with depth by a geothermal gradient of $dT/dz = 0.03\,\mathrm{K\ m^{-1}}$. With the dimensions for the numerical model of 240 m×240 m×110 m, the boundaries are far away enough from the storage volume so that heat does not flow across them. All boundaries are closed during the simulation except for the top surface, where the temperature is held constant at 9 °C. Twenty years of biannually alternating heat injection and recovery are simulated. Approximating heat storage during summer and heat recovery during winter, heat is injected for six months at high inlet temperatures of 90 °C and recovered for six months at low temperatures of 10 °C. The temperature function is defined in that way because simplified boundary conditions allow for a characterisation of the storage. The flow rate by which the heat carrier fluid is pumped through each pipe is $|Q| = 10^{-3}\,\mathrm{m^3\ s^{-1}}$.

Tab. 4.1 *Thermal parameters used for numerical simulation of the base scenario*

Material	λ [W m^{-1} K^{-1}]	$c\rho$ [MJ m^{-3} K^{-1}]
Heat carrier fluid	0.56	4.2
Pipe	0.42	1.7
Grout	2.00	3.9
Storage formation	2.00	2.0
Insulating layer	0.06	1.5
Overburden layer	1.5	1.9

To simulate heat storage through double U-tube BHEs, an adapted modelling approach introduced by Boockmeyer and Bauer (2016) is used in the presented scenario. In this approach, all BHE's components are explicitly accounted for. Following the shown principle, the circular BHE geometry is converted into an angular geometry that allows for lower mesh densities and thus reduced computation times compared to a circular geometry. The component's volumes are the same in both original and adapted model and

the true volumetric heat capacities can therefore be used for the numerical simulation. Due to the changes in shape, however, equivalent pipe thermal conductivities have to be used. For grout thermal conductivity, its original value is used (Boockmeyer and Bauer 2016). Generally, the adapted model allows for a coarser discretisation and this reduces the computation time by a factor of 50 for a double U-tube BHE compared to a conventional fully discretised model, accepting minor heat balance deviations of around 1 % and temperature differences in the range of 0.1 °C in the subsurface. The spatial discretisation of the storage formation is finest directly at the BHEs with $\Delta x = 0.05\,\mathrm{m}$ and is coarsened with increasing distance from the BTES. In total, the numerical mesh consists of around 694,000 elements. Due to the transient behaviour of the BHE, 60 time steps with increasing size are needed at the beginning of each storage and recovery phase to correctly simulate the steep initial temperature rise and fall as well as the steep spatial gradients after changing the temperature of the heat exchanger fluid.

4.4 Scenario variations

Besides the base scenario of a BTES with 61 double U-tube BHEs installed in a distance of 5 m from each other, further scenarios with variation of different parameters are defined:

- BHE number: For comparison of storage size effects, heat is stored in four different BTES consisting of 1, 7, 19, and 37 parallel-connected double U-tube BHEs with each a length of 50 m (setup is shown in Fig. 4.1).
- BHE distance: Based on a BTES with 61 BHEs, seven variations of BHE distance are simulated for each thermal parameter. Application examples like in Neckarsulm or Crailsheim operate with BHE distances smaller 3 m. To identify differences between typically used values and unused large distances, BHEs are placed in distances of 2, 3, 4, 5, 6, 7, and 8 m from each other. Thus, the volume of the storage varies from $9,150\,\mathrm{m}^3$ with a diameter of 16 m for 2 m BHE distance to $146,320\,\mathrm{m}^3$ with a diameter of 64 m for 8 m BHE distance.
- Thermal parameters: In Schleswig-Holstein, common shallow geological formations are sediments that were deposited during the alternating glacial and interglacial periods of the Pleistocene. These are mainly glacial deposits like till (silt with clay, sand, gravel) that forms the ground or end moraines and glaciofluvatile deposits like meltwater sands and gravels. Along the North Sea cost, postglacial deposits like marine or brackish marsh sediments (mostly silt) are also found (LLUR 2012). Thermal conductivities in those formations range from 1.0

to 3.0 W m^{-1} K^{-1} and heat capacities from 1.5 to 3.0 MJ m^{-3} K^{-1} (respective values from VDI 4640 Part 1 (2010)). For the BTES with 61 BHEs, both parameters are varied in steps of 0.5 W m^{-1} K^{-1} or $W\ m^{-1}\ K^{-1}$ within the abovementioned typical spectrum. To find an optimum BHE distance for every thermal parameter considered in this work, the BHE distance is varied for each thermal parameter, too.

- Storage operation mode: In the base scenario, heat is injected for six months and recovered for six months. As variation of the storage operation mode, a scenario is defined with each four months of injection/recovery and a two-months-long pause in between the two storage phases. As well as for the biannual alternating storage scenario, BHE distances and thermal parameters are varied for the storage scenario with four months of heat injection and recovery.

In total, 142 different storage scenarios are simulated here, including the base scenario (Tab. 4.2).

Tab. 4.2 *Variation of storage parameters for the different BTES scenarios. Bold numbers represent the base scenario*

Parameter	Variation						
BHE number* [-]	1	7	19	37	**61**		
BHE distance [m]	2	3	4	**5**	6	7	8
Subsurface thermal conductivity [W m^{-1} K^{-1}]	1.0	1.5	**2.0**	2.5	3.0		
Subsurface heat capacity [MJ m^{-3} K^{-1}]	1.0	1.5	**2.0**	2.5	3.0		
Storage operation mode	6 months		4 months				

*only varied in the storage scenario with 6 months of heat storage/recovery

4.5 Simulation results

In the first heat storage scenario, heat injection as well as heat recovery phase each take six months. In general, temperatures inside the storage rise during heat injection until they are highest at the end of the heat storage phase. During heat recovery, temperatures sink and thus are lowest at the end of the heat recovery phase (Fig. 4.2). Additionally, over time, the temperature signal spreads further into the subsurface and temperatures slowly increase outside the storage area.

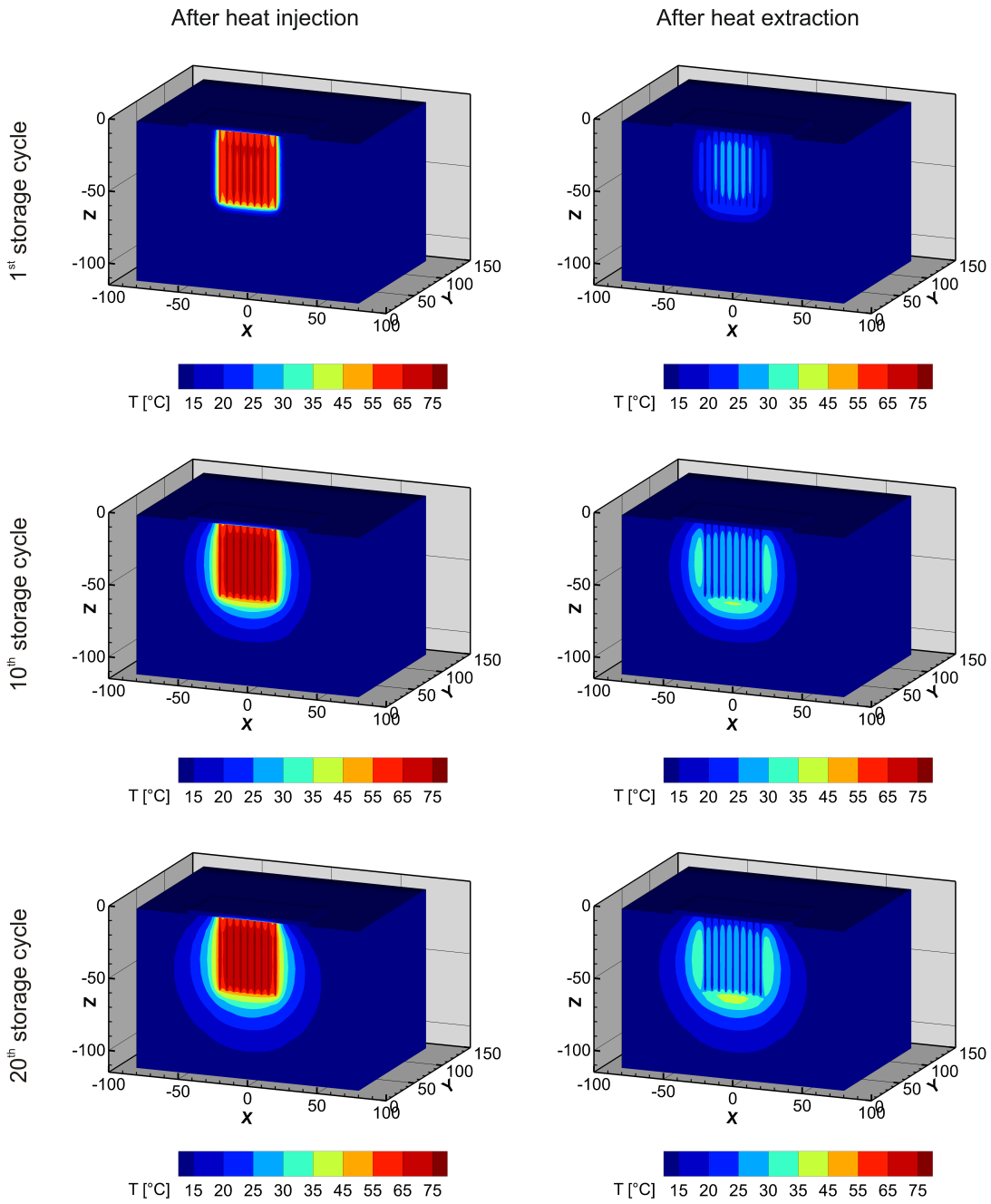

Fig. 4.2 *Temperatures inside the storage at the end of the 1^{st}, 10^{th}, and 20^{th} heat injection/recovery period of the base scenario. In y-direction the model domain is cut through symmetry axis at $y = 0$ m*

4.5.1 Base scenario

For the first five days at the beginning of the heat storage phase, the BHEs of the storage each act as a single BHE. During this time, the temperature signal is transported through the pipe by the heat exchanger fluid. Then, the pipes and the grout that is surrounding them are heated. Finally, heat spreads radially into the subsurface. After five days, the BHEs start to interact with each other (Fig. 4.3).

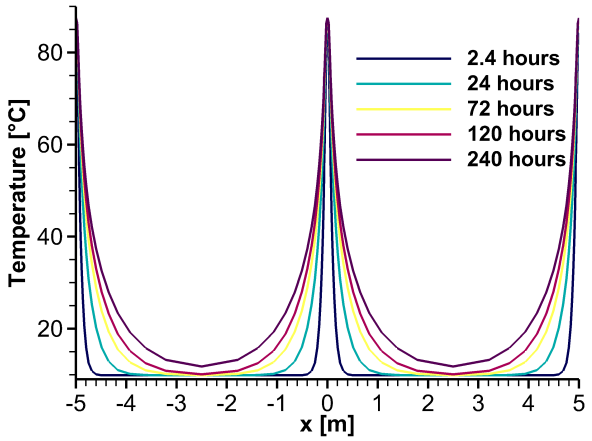

Fig. 4.3 *Temperature profiles along the x-axis between the centre of the inner BHEs for the base scenario after 2.4, 24, 72, 120, and 240 hours of heat injection*

From this moment on, the temperature signals of neighbouring BHEs overlap and the storage temperature rises, because heat cannot be transported further away from the BHEs. After the first heat injection, temperatures are around 86 °C directly at the BHEs and around 64 °C inside the BTES volume. (Fig. 4.4 a). Outside, temperatures only rise to 47 °C at a distance of 1 m and 19 °C at a distance of 5 m from the outer BHEs. During heat recovery, the storage mechanism is reversed, following the same principle. First, cool water with a temperature of 10 °C is pumped through the pipes. Then, the temperature signal spreads through pipe and grout into the storage formation. The neighbouring BHEs start to interact and the storage temperature sinks. After the first heat recovery, the temperature is lowest close to the BHEs (i.e. 12.5 °C, Fig. 4.4 b). Inside the BTES, the temperature drops to about 28 °C in the centre. At a distance of 1 and 5 m from the outer BHEs, the temperature is only 20 and 19.5 °C, respectively. With increasing storage cycle, the temperatures inside and outside the storage volume generally rise. After the 20^{th} heat injection, they reach 70 °C inside the BTES. Outside, temperatures are 59 and 38 °C at 1 and 5 m from it. The same trend is observed during heat recovery but to a minor extent. After the 20^{th} heat recovery, the temperature is 30 °C inside the storage volume. However, heat accumulates outside the BTES over time remaining in the subsurface. At a distance of about 5 m from the outer BHEs, the

temperature is at a maximum of 34 °C after the 20th heat recovery.

The amount of heat that can be injected or recovered at a certain moment of time during the operation (i.e. the heat injection/extraction rate) is proportional to the temperature difference between pipe inlet and outlet (Fig 4.5 a). For the first hour, this difference is only influenced by the borehole dimension and thermal parameters as well as the temperature difference between heat exchanger fluid and borehole. As this temperature difference is high, the heat injection and extraction rate are high as well. Additionally, the rapid temperature switch after heat storage and recovery leads to unrealistic high rates during the first fourty seconds of each phase. Realistically, the heat injection/extraction rate ranges from 0.1 to 1 MW (Fig. 4.5 b).

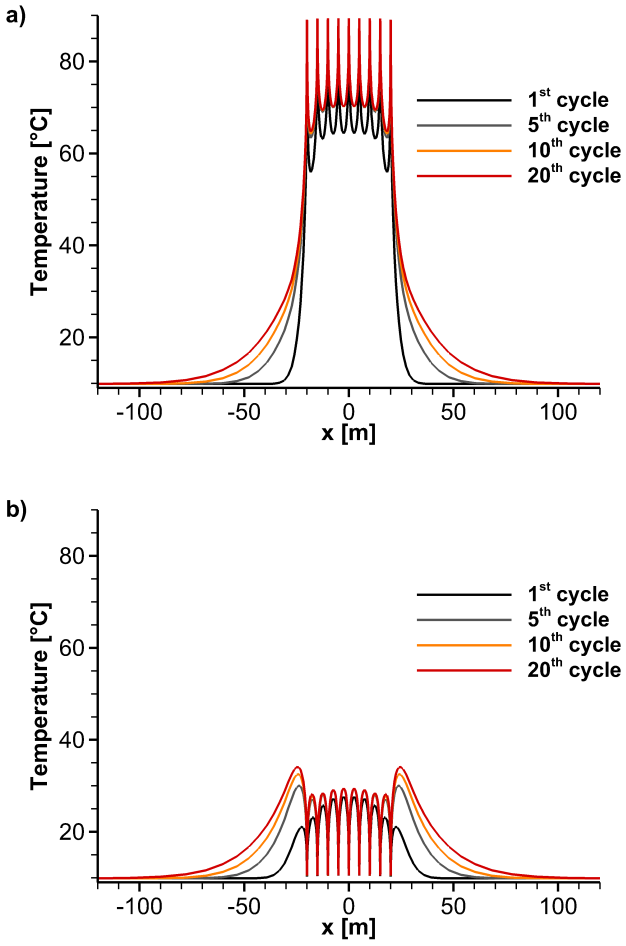

Fig. 4.4 *Temperature profiles through the storage centre along the x-axis for the base scenario after 1st, 5th, 10th, and 20th heat injection (a) and recovery (b)*

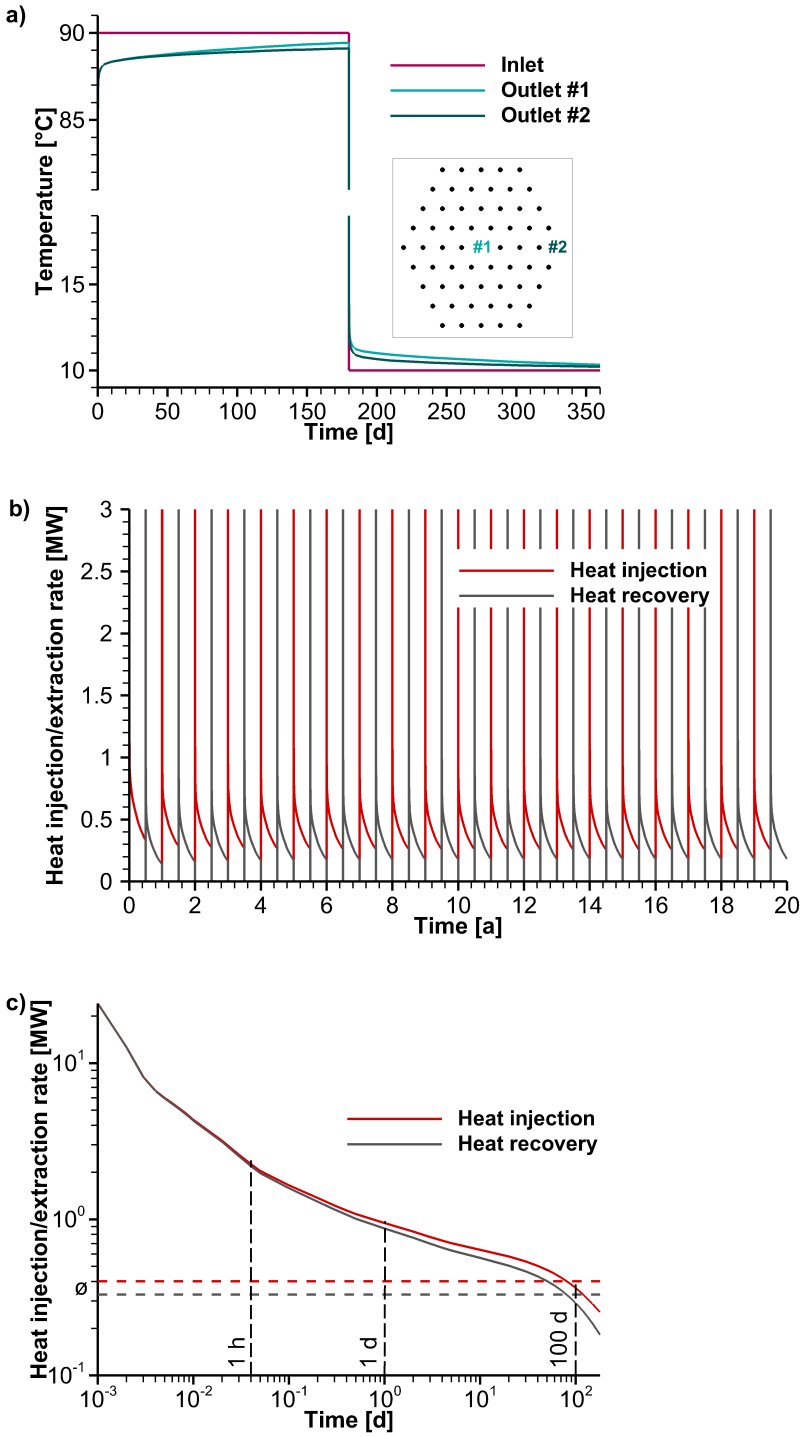

Fig. 4.5 *Pipe inlet and outlet temperatures for the inner and a marginal pipe during heat injection and recovery of the base scenario (a), long-term behaviour of total heat injection and extraction rate during alternating heat injection and recovery (b) and development of total heat injection and extraction rate with corresponding mean rates for the 20th heat storage cycle (c)*

With time, the temperature difference between pipe inlet and outlet is primarily controlled by the storage thermal parameters. As it decreases, the heat injection and extraction rate drop exponentially until they are lowest after half a year (Fig. 4.5 c). Since the subsurface heats up during alternating heat injection and recovery, the temperature difference between heat exchanger fluid and subsurface decreases over time. Therefore, the heat injection rate decreases as well. In the 20^{th} heat injection phase, the mean heat injection rate is 0.4 MW with corresponding maximum and minimum values of 24 MW and 0.25 MW, respectively (Fig. 4.5 c). Although the heat injection and extraction rate curves generally show the same behaviour, the heat injection rate is always higher than the heat extraction rate because heat is transported away from the storage into the subsurface (i.e. temperature gradients point towards the model boundaries). In contrast to the heat injection rate, the mean heat extraction rate increases over time as the storage temperature increases and more heat is available for extraction. In the 20^{th} heat recovery phase, it is thus 0.33 MW with 24 MW at the beginning and 0.18 MW at the end of the recovery phase.

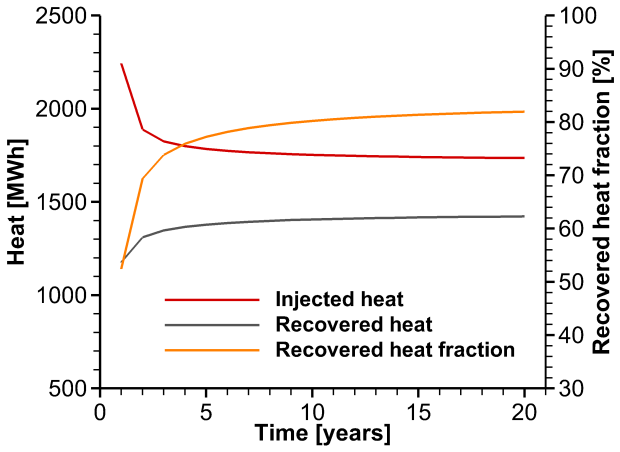

Fig. 4.6 *Injected and recovered heat over time with the corresponding recovered heat fraction (fraction of injected heat that can be recovered) for the base scenario*

Because the heat injection rate is always higher than the heat extraction rate, the recovered heat fraction (i.e. the fraction of heat that can be recovered from the previously injected heat) is always smaller than 100 % (Fig. 4.6). For example, after the first year of operation, 2,243 MWh of heat are injected and 1,176 MWh are retrieved, leading to a recovered heat fraction of 52 %. Over time, the amount of heat that can be injected decreases while the amount of heat that can be recovered increases because the storage temperatures rise. Therefore, the recovered heat fraction improves. After five years of operation, the amounts of heat injected and recovered are 1,785 MWh and 1,378 MWh. The injected heat decreases to 1,732 MWh while recovered heat increases to 1,423 MWh after twenty years. The recovered heat fraction is thus 77 % and 82 %

after five and twenty years, respectively. To recover a high fraction of the injected heat already with the first recovery, heat could initially only be injected for a few years to load the storage site before it is retrieved (e.g. as done in Neckarsulm, Bauer et al. 2009). Because of the high and low inlet temperatures of 90 °C and 10 °C assumed in this work, the achieved recovered heat fraction is higher in this scenario compared to existing storage sites in practice (69 % in Crailsheim with a maximum storage temperature of 70 °C (Bauer et al. 2013a).

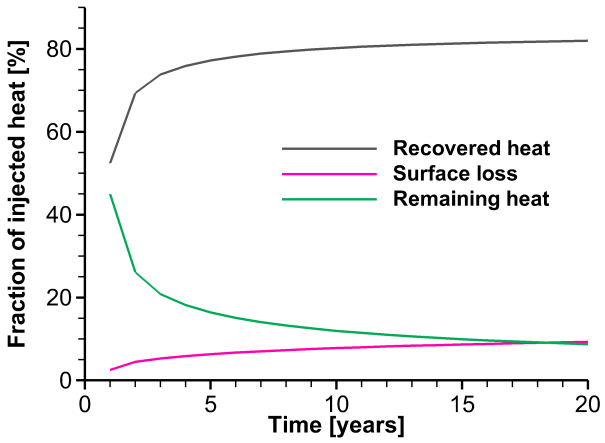

Fig. 4.7 *Recovered heat, surface loss and remaining heat as fraction of injected heat over time for the base scenario*

Nevertheless, heat is lost in this investigated scenario (Fig. 4.7). In the first year, 52 % of the injected heat can be recovered, hence 48 % are lost. After twenty years, 82 % are recovered and only 18 % are lost. Therefore, the total amount of lost heat decreases over time. It can be divided into heat that remains in the subsurface and heat that is lost over the land surface. The remaining heat drops over time while heat accumulates in the storage until storage temperatures have stabilised.

In contrast, the surface loss increases with time as the subsurface is heated continuously and the temperature signal spreads further. Aggravated over 20 years, 5,414 or 2,618 MWh remain in the subsurface or are lost over the land surface, respectively (Fig. 4.8), corresponding to 15 % or 7 % of the overall injected heat (Tab. 4.5, for 5 m BHE distance).

The fact that heat remains in the subsurface implicates that the volume that is used by the BTES is significantly smaller than the volume that is influenced. The volume that is used is the volume in which heat can be recovered with the given storage scenario, i.e. maximum where the temperature gradient points towards the BTES. Laterally, it is limited by the temperature maximum 5 m away from the outer BHE (Fig. 4.4 b). Beyond this maximum, the temperature gradient is always directed away from the

storage site towards the model boundaries and heat propagates away from it. That part of the injected heat is lost to the surrounding subsurface. The volume that is influenced by the temperatures arising from the BTES is the area in which the difference between initial and introduced temperatures is still larger than 5 °C for example (Fig. 4.9).

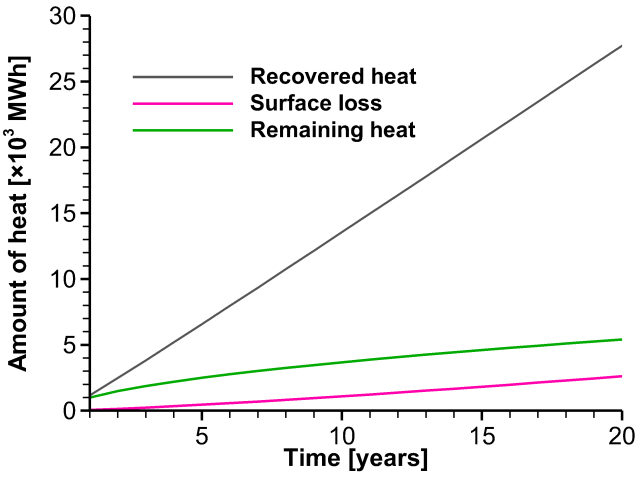

Fig. 4.8 *Accumulation of the amounts of recovered heat, surface loss and remaining heat over time for the base scenario*

Over time, the rising temperatures lead to an expansion of the volume that is influenced. Twenty years of heat injection and recovery result in an influenced volume with a horizontal radius of 53 m around the BTES centre and a vertical extent of 85 m. In contrast, the volume that is actually used by the storage, i.e. from which heat is recovered, is much smaller with a horizontal radius of 25 m around the BTES centre and a vertical extent of 53 m.

The usable heat capacity of the BTEs can be derived from the amount of recovered heat and the volume that is used by the storage

$$Usable\ heat\ capacity = \frac{Amount\ of\ recovered\ heat}{Volume\ used\ by\ the\ storage}$$

In the base scenario, the usable heat capacity is 13.8 kWh m^{-3} after the 20th heat storage cycle. To determine if the storage exploits its full potential, this value is put in relation to the theoretically possible heat capacity

$$Theoretical\ heat\ capacity = c\rho\Delta T$$

With the defined temperature difference between storage and recovery phase of 80 °C, the theoretical heat capacity is 44.4 kWh m^{-3}, which means in the considered scenario 31 % of the potential can technically be used. However, the theoretical heat capacity

can only be achieved in an unrealistic setting, where the subsurface has the same temperature as the heat carrier fluid after heat injection or recovery and where no heat is lost.

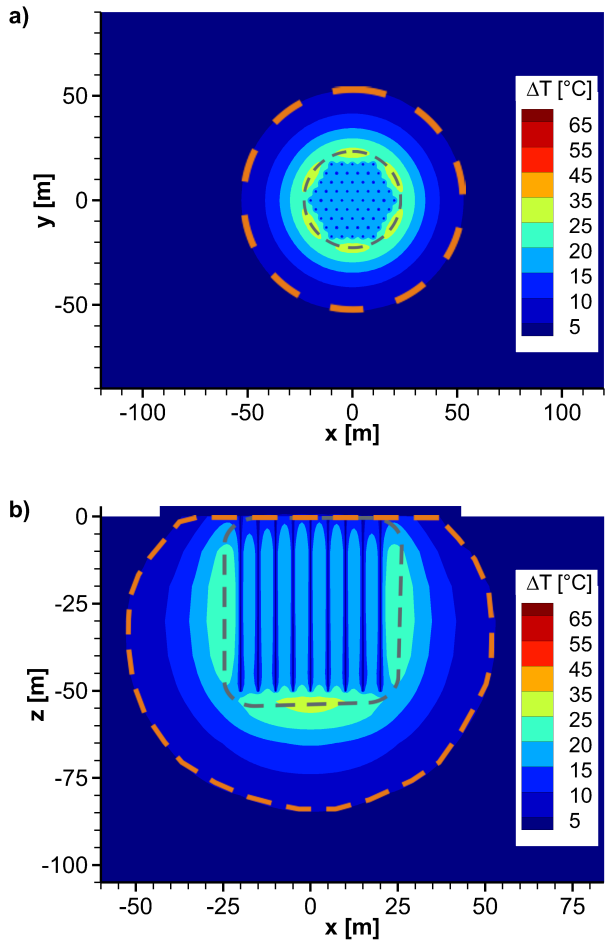

Fig. 4.9 *Difference between temperature distribution after the 20th heat recovery and the initial condition of the base scenario as horizontal (a) and vertical (b) slice through the storage centre with the corresponding volumes from which heat is recovered during a storage cycle (grey) and with 5 °C temperature difference (orange)*

4.5.2 Variation of BHE number

Variation of the BHE number is a variation of the storage size without altering the BHE distance. First, temperature profiles through the storage show that different storage temperatures are achieved with different BHE numbers (Fig. 4.10). The ”storage“ with a single BHE represents a special case because it is not a BTES by definition and a storage temperature cannot be determined. The storage temperatures are similar for the different BTES, except for the BTES consisting of 7 BHEs.

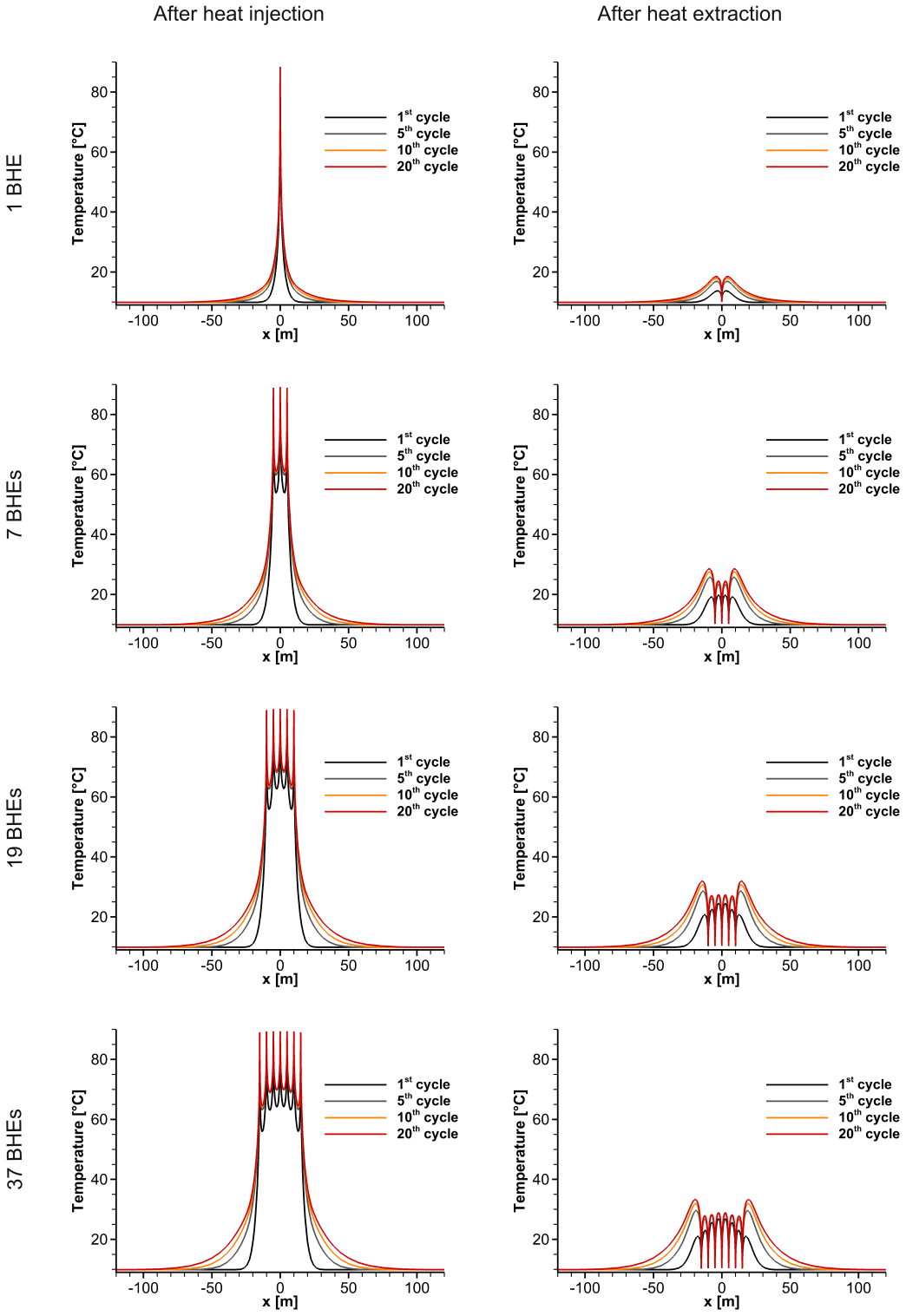

Fig. 4.10 *Temperature profiles through the storage centre along the x-axis after 1st, 5th, 10th, and 20th heat injection/recovery for the BTES with 1, 7, 19, and 37 BHEs in 5 m distance*

With 7 BHEs, temperatures are up to 10 °C lower at the end of heat injection or recovery compared to the base scenario, but with more BHEs they only vary around 2 °C. The reason is that only one BHE in the BTES with 7 BHEs is actually placed inside the storage while most BHEs are marginal BHEs and emit the heat directly to the surrounding subsurface. Therefore, the temperatures are higher with higher BHE number. Moreover, the mean temperature difference ΔT after heat injection and extraction is also almost the same for all storage scenarios; except with 7 BHEs it is 4 °C smaller than with 61 BHEs. Hence, in the investigated scenarios, the storage temperatures do not have an effect on storage characteristics.

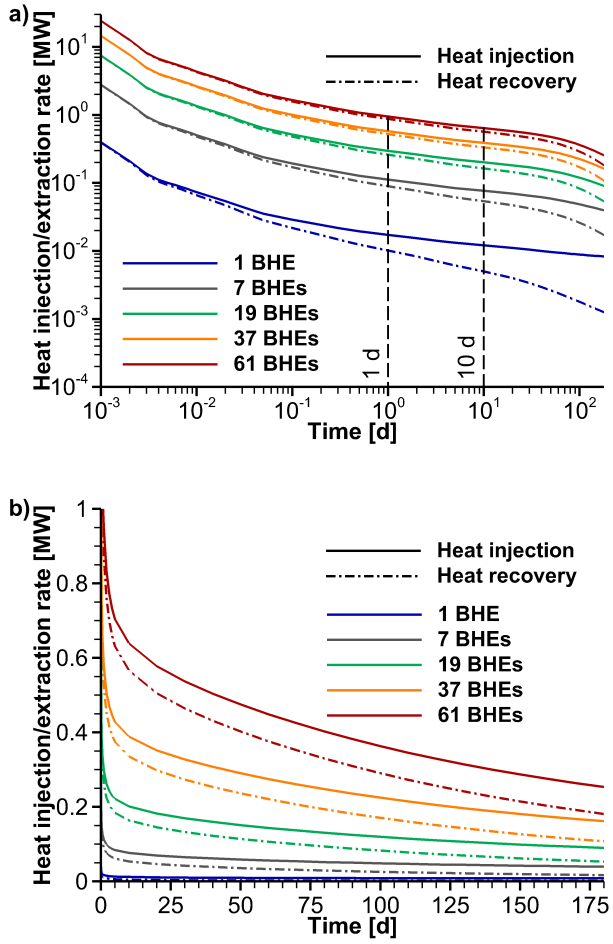

Fig. 4.11 *Development of heat injection and extraction rate in the 20th heat storage cycle for the BTES with 1, 7, 19, 37, and 61 BHEs in log-log (a) and linear scale (b)*

However, the heat injection and extraction rates vary significantly (Fig. 4.11 shown for the 20th storage cycle). In general, they increase with the number of BHEs installed, because more parallel-connected BHEs are operating with the same boundary conditions and thus naturally introduce and recover more heat into and from the subsurface.

Moreover, the gap between heat injection and extraction rate is largest with a single BHE and shrinks with increasing BHE number. Accordingly, mean injection and extraction rate increase with BHE number as well. Compared to the base scenario, the mean heat injection rate is smaller by a factor of 40 with a single BHE and smaller by a factor of three with 19 BHEs. The heat extraction rate is smaller by a factor of 140 or 3.5, respectively. This means that the rates are not simply proportional to the BHE number, i.e. the rate is not 61 times higher with a 61 times higher BHE number (Tab. 4.3).

Tab. 4.3 *Mean heat injection and extraction rates as well as recovered heat fraction in the 20th storage cycle for the whole BTES and per BHE of the different storages*

		BHE number				
		1 BHE	7 BHEs	19 BHEs	37 BHEs	61 BHEs
Rate [kW]	Injection	9.4	52.9	131.6	248.1	401.8
	Recovery	2.3	30.2	94.6	194.2	329.3
	Injection (per BHE)	9.4	7.6	6.9	6.7	6.6
	Recovery (per BHE)	2.3	4.3	5.0	5.3	5.4
Recovered heat fraction [%]		24.68	57.15	71.90	78.25	81.96

On the contrary, the mean heat injection rate per BHE is higher with smaller BHE numbers, as smaller storages consist of relatively more marginal BHEs (e.g. the BTES with 7 BHEs consists of one inner and six outer BHEs) and there is less interaction between them. The mean heat extraction rate per BHE is higher with larger BHE numbers due to improved surface-area-to-volume and inner-to-marginal-BHE ratios of larger storages with comparatively less heat loss.

The amounts of injected and recovered heat not only reflect the mean rates, they also increase with higher BHE number (Fig. 4.12). After the 20$^{\text{th}}$ heat storage cycle, the amounts of injected and recovered heat are 40 and 140 times higher with 61 BHEs than with 1 BHE. This leads to a 3.3 times higher heat recovery rate. However, the heat recovery rate almost stagnates when the BHE number rises above 19 BHEs. With 19 BHEs, the heat recovery rate is only 1.1 times smaller than with 61 BHEs and with 37 BHEs the ratio is even less with 1.05.

In general, the total heat loss increases with higher BHE numbers because with more BHEs more heat is introduced to the subsurface. In relation to the amount of injected heat, heat loss depends on the surface-area-to volume ratio and thus is smaller with

higher BHE numbers. This means, during 20 years of heat storage and recovery, 77 % of the overall injected heat are lost with a single BHE. With 19 and 61 BHEs, it is only 33 and 22.5 %, respectively. Surface loss and remaining heat as fraction of injected heat behave differently. The storage area grows with increasing BHE number and therefore the surface loss increases. The improved surface-area-to-volume ratios of larger storages as well as their BHE interactions lead to a decline of the remaining heat (Fig. 4.13).

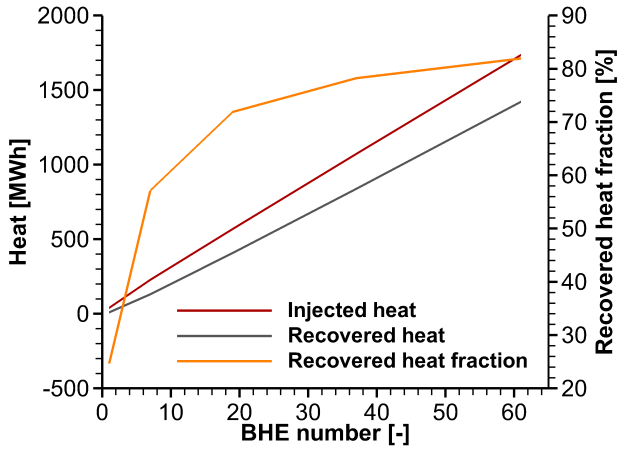

Fig. 4.12 *Injected and recovered heat over BHE number with the corresponding recovered heat fraction in the 20th storage cycle*

Concerning influenced and used volume; the simulation results show that both volumes are larger with higher BHE numbers. However, in vertical direction the BHE length mainly controls the temperature extent. Since it is 50 m for all storage scenarios, the vertical temperature extent is similar and the (horizontal) areas are thus a good measure for comparison. The influenced and used areas will be evaluated hereafter. With a single BHE, an area with a horizontal radius of 13 m is influenced by the storage while the area within a 4 m radius is used by it. Respectively, with 19 BHEs, the horizontal radii are 39 and 14.5 m for influenced and used volume, respectively. This yields a ratio of 6.4 and 5.6 for 1 and 19 BHEs between the volume that is additionally influenced and the used volume. In the base scenario, this ratio is 3.8, i.e. because the surface-area-to-volume ratio improves with increasing storage size, the ratio improves as well. Furthermore, the usable heat capacity increases from 3.8 kWh m^{-3} for a single BHE to 11.7 kWh m^{-3} for 19 BHEs to 13.8 kWh m^{-3} for 61 BHEs. With a constant theoretical heat capacity of 44.4 kWh m^{-3} for all BHE distances, the usable fraction of the theoretical heat capacity thus improves with BHE distance as well.

In summary, with higher BHE numbers more heat can be injected and recovered with an improved heat recovery rate as well as usable heat capacity while at the same time heat loss (in relation to injected heat) and the ratio between influenced and used volume

are reduced.

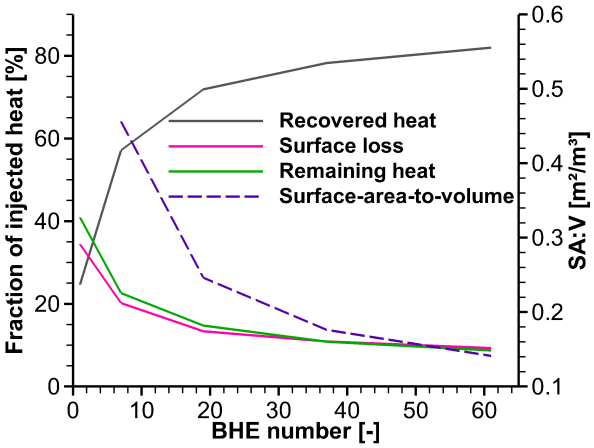

Fig. 4.13 *Recovered heat, surface loss and remaining heat as fraction of injected heat over BHE number in the 20th storage cycle and surface-area-to-volume-ratio of the investigated storages*

4.5.3 Variation of BHE distance

When the BHE distance in the scenario described above is altered between 2 and 8 m, the storage behaviour changes. This is expressed through changes in storage temperatures, heat balances and required areas after injection and recovery. Primarily, the changing storage behaviour is reflected by the storage temperatures (Fig. 4.14). With increasing BHE distance, the space between the BHEs expands. This means that with smaller BHE distances the volume of subsurface material inside the storage that is available for heat storage and thus the storage capacity are smaller. In the scenario with 2 m BHE distance, the temperature inside the storage is highest (about $85 - 89.7\,°C$ already after the first heat injection period) almost reaching the defined inlet temperature of 90 °C. Therefore, the temperature difference between BHE and storage that controls the heat transfer is smallest with 1 to 5 °C. Under this condition, considerably less heat can be transferred into the storage volume and its capacity is reached long before the end of the storage phase, i.e. the storage is loaded with the defined storage mode. In contrast, a larger volume of subsurface material inside the BTES is available for heat storage with larger BHE distances. Then the storage limit is not reached with the defined storage operation mode and storage temperatures are generally lower. For a BHE distance of 8 m, the storage temperature is much lower with 35 °C after the first heat injection and 55 °C from the fifth heat injection phase leading to a higher temperature difference of 35 °C between storage volume and BHE (Fig. 4.15).

Since the temperature difference is always significant, heat can be introduced into the storage formation throughout the whole time of the heat injection period and the stor-

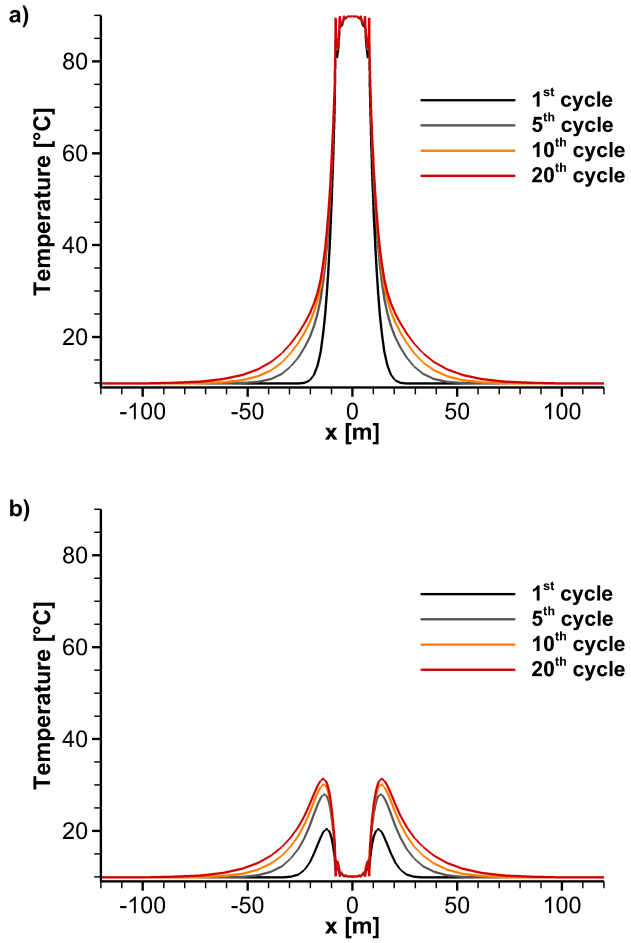

Fig. 4.14 *Temperature profiles through the storage centre along the x-axis after 1^{st}, 5^{th}, 10^{th}, and 20^{th} heat injection (a) and recovery (b) for the BTES with 61 BHEs in 2 m distance*

age volume is not filled completely. The same effect at reversed temperatures can be observed after the heat recovery period. Here, the storage temperature is lowest in case of a BHE distance of 2 m with $10.2 - 13\,°C$ already after the first recovery. As during heat injection, the temperature difference between the BHEs and the storage formation is minor and little heat can be recovered (i.e. the storage is emptied to its limits). With larger BHE distances however, storage temperatures are comparatively higher. In case of a BHE distance of 8 m, the storage temperature is 28 °C after the first and 42 °C after the fifth heat recovery. The temperature difference between BHE and storage formation thus is 32 °C indicating that the BTES is not emptied completely but heat remains in the subsurface that cannot be regained with the defined setup but likely with a longer heat recovery phase. In summary, storage temperatures after heat injection and recovery as well as their difference decrease with increasing BHE distance.

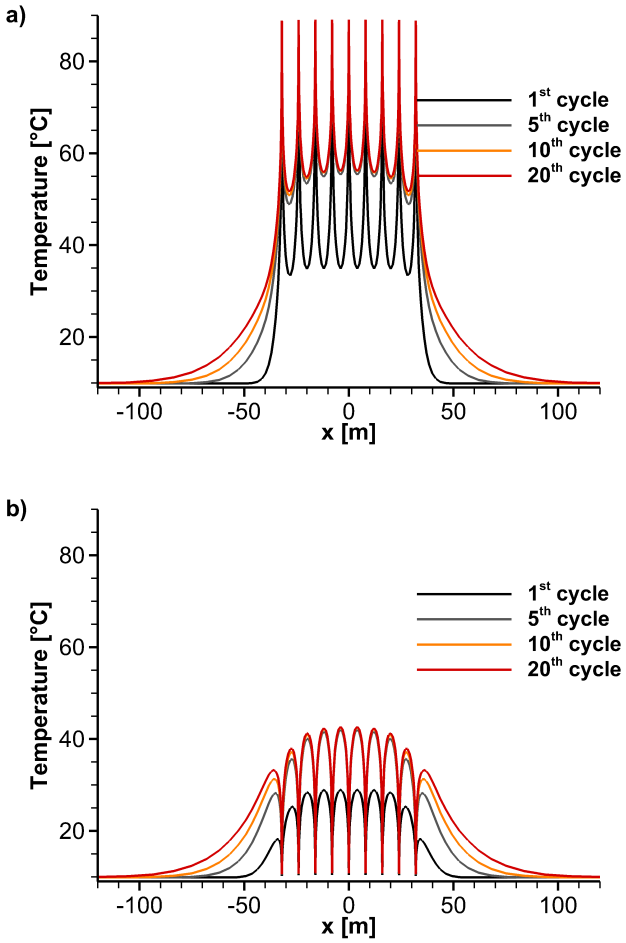

Fig. 4.15 *Temperature profiles through the storage centre along the x-axis after 1st, 5th, 10th, and 20th heat injection (a) and recovery (b) for the BTES with 61 BHEs in 8 m distance*

As the heat injection and extraction rates are coupled directly to the observed temperatures they are similarly influenced when the BHE distance is varied (Fig 4.16, shown for heat extraction rates). At the beginning of heat injection or recovery, the heat injection or extraction rate is only affected by the borehole dimension and thermal parameters. As a result, the maximum heat injection and extraction rates are about the same for all BHE distances. After ten days, heat injection and extraction rates drop comparatively faster with small BHE distances, while they decrease only gradually after ten days with large BHE distances. At the end of the 20$^{\text{th}}$ heat recovery period, the heat extraction rate is still almost ten times higher with 8 m BHE distance than with 2 m. Consequently, the minimum heat injection and extraction rates increase with BHE distance. Additionally, the heat injection rate is higher for larger BHE distances during the whole heat storage phase and thus is the mean heat injection rate.

However, mean heat extraction rates behave differently (Tab. 4.4). In the 20$^{\text{th}}$ heat

recovery period, it is at a maximum for a BHE distance of 6 m. This means that the observed heat injection and extraction rates confirm the assumption that with a small BHE distance the BTES is already almost full or empty at an early point of heat storage or recovery. For heat recovery, this means that considerably less heat can be regained from the storage. In addition, with larger BHE distances more heat can be injected during heat storage periods as heat injection rates stay high over a longer time. The same applies for the heat extraction rate, which remains at a constant level and confirms that the BTES cannot be emptied with the defined setup.

Tab. 4.4 *Mean heat injection and extraction rates in the 20th storage cycle as well as recovered heat and heat losses as a fraction of injected heat summarized over whole time*

	Mean rate [kW]		As fraction of injected heat* [%]		
BHE distance	Injection	Recovery	Recovered heat	Surface loss	Remaining heat
2 m	179	142	76.63	7.60	15.77
3 m	285	237	80.16	6.59	13.25
4 m	363	303	79.96	6.62	13.42
5 m	402	329	77.55	7.32	15.14
6 m	417	333	74.20	8.33	17.48
7 m	425	328	70.33	9.37	20.30
8 m	429	319	66.33	10.41	23.26

*total amounts over whole simulation time divided by total injected heat

The achieved amounts of injected and recovered heat are proportional to the mean heat injection and extraction rates. Resulting from the heat injection rates, the amount of injected heat thus increases with increasing BHE distance (Fig. 4.17). It increases linearly until a BHE distance of 4 m BHE and then stagnates when the BHE distance increases further. The maximum storable amount is 1,854 MWh (for 8 m); compared to the minimum amount of 773 MWh (2 m) in the 20$^{\text{th}}$ cycle. Based on the mean extraction rate, the recovered heat is at an optimum with 6 m BHE distance where 1,438 MWh of heat are recovered in the 20$^{\text{th}}$ cycle. That is 2.3 times higher than the minimum value. The smallest amount of heat is regained with 2 m BHE distance, but the recovered heat fraction is lowest with 8 m BHE distance. With 4 m BHE distance, the recovered heat fraction is at an optimum of 84 %. Still, all BTES achieve recovered heat fractions between 74 % and 84 % in the 20$^{\text{th}}$ heat storage cycle.

The recovered heat fractions are linked to the total heat loss (sum of surface loss and

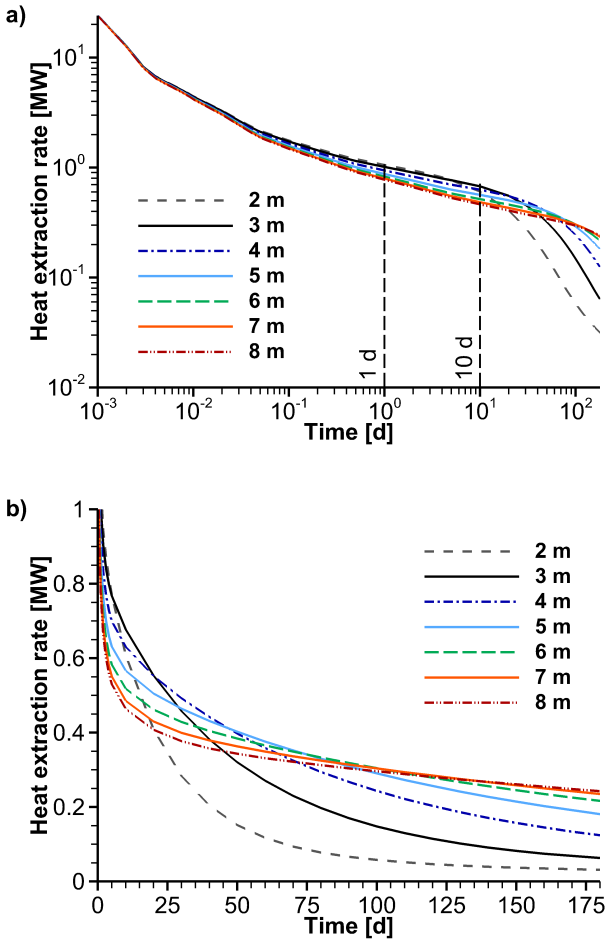

Fig. 4.16 *Heat extraction rate in the 20th heat storage cycle of all investigated BHE distances in log-log (a) and linear scale (cut above 1 MW) (b)*

remaining heat), i.e. lower recovered heat fraction means higher heat loss (Tab. 4.4). The surface loss scales with storage size. For larger BHEs, the horizontal storage area increases leading to higher surface losses. However, in relation to the amount of injected heat the surface loss is similar for all BHE distances throughout the entire storage time (Fig 4.18, after one and twenty years).

The heat that is lost because it remains in the subsurface is higher for larger BHE distances as well. Deducing from the temperature distribution with temperatures inside the BTES that are close to the BHE inlet temperature, for small BHE distances the remaining heat is mainly located outside the storage surrounding it. Storage systems with medium BHE distances are able to store more heat in the space between the BHEs while at the same time their surface-area-to-volume ratio is smaller, which is favourable because the area over which heat is lost from the storage is thus comparatively smaller. Then, the remaining heat is lower which corresponds to the highest recovered heat

fractions. However, when the BHE distance is larger than 5 m, in addition to the heat surrounding the BTES more heat remains in the space between the BHEs. This is reflected in lower temperatures between the BHEs after heat injection and higher temperatures after heat recovery. Most of the remaining heat is already introduced during the first storage cycle, while after twenty years it is about the same for all considered variations (Fig. 4.18). Therefore, besides subsurface thermal parameters and storage mode, the heat loss depends on both surface-area-to-volume ratio and the usable storage volume between the BHEs.

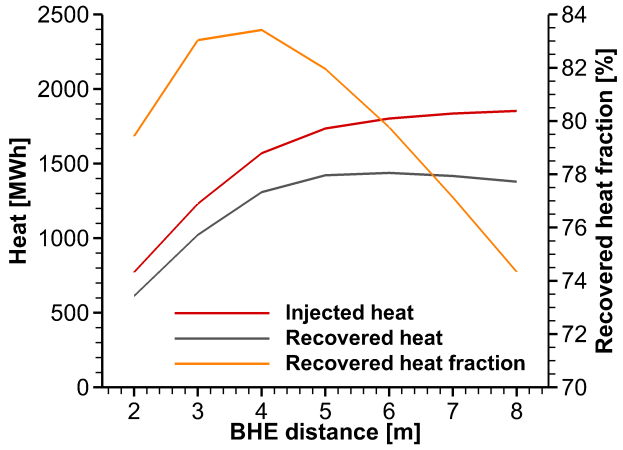

Fig. 4.17 *Injected and recovered heat over BHE distance with the corresponding recovered heat fraction in the 20th storage cycle*

Both, influenced and used area deduced from the temperature differences are larger with higher BHE distance (Tab. 4.5). With 2 m BHE distance, the areas with horizontal radii of 38 m and 14 m with a ratio of 5.5 are influenced and used by the storage. For a large BHE distance of 8 m, the horizontal radii are larger with 65 and 36 m for influenced and used area, respectively. This yields a ratio of 2.6 between the area that is additionally influenced and the used area. However, their usable heat capacity is poor with 6.4 kWh m^{-3} resulting in a fraction of only 14.5 % of the theoretical heat capacity. Both increase with smaller BHE distances with the result that the usable heat capacity is largest with 2 m BHE distance. After the 20$^{\text{th}}$ storage cycle, it is 17.5 kWh m^{-3} corresponding to a fraction of 39.4 %. Although larger storages require more space, in relation to their storage size they influence a smaller area, while smaller storages yield higher values concerning the usable heat capacity.

To summarise, with the given constraints, medium large systems are able to provide the largest absolute amounts of heat during heat recovery and are thus favourable in that regard. However, in relation to the amount of injected heat, more heat can be recovered with small BHE distances because the storage is filled and emptied to its limit and

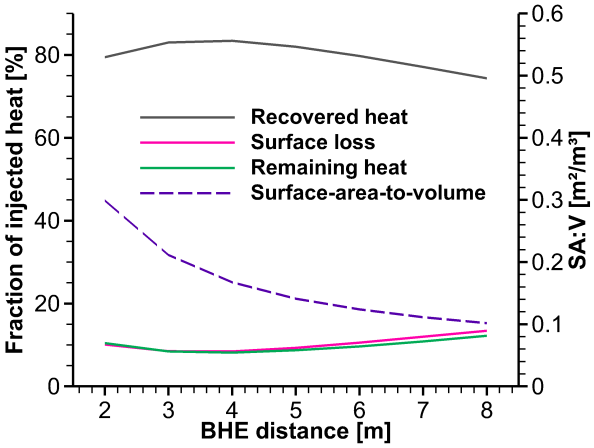

Fig. 4.18 *Recovered heat, surface loss and remaining heat as fraction of injected heat over BHE distance in the 20th storage cycle and surface-area-to-volume-ratio of the investigated storages*

usable heat capacities are higher. Concerning recovered heat fraction and usable heat capacity, smaller storages are therefore preferable. As small BTES systems work at their limits, they induce higher temperatures in the subsurface and influence a large area compared to their size. Larger storages require more space, but in relation to their storage size they influence a smaller area and temperatures are lower. For this reason, they are preferred when the effect on the subsurface should be minimized. Still, the results also indicate that systems with larger BHE distances need more time to operate steadily. In this work, 20 years of heat storage are investigated; after longer times the effects may develop differently.

Tab. 4.5 *Radii of influenced and used area, relation of additionally influenced volume to used volume as well as usable heat capacity after the 20th storage cycle for storages with different BHE distances*

	Radius of area [m]		Ratio of influenced	Usable heat
BHE distance	Influenced	Used	to used area [-]	capacity [kWh m^{-3}]
2 m	38	14	5.5	17.5
3 m	44	18	4.7	18.5
4 m	49	21	4.3	17.1
5 m	53	25	3.8	13.8
6 m	57	28	3.4	10.8
7 m	61	33	2.9	8.0
8 m	65	36	2.6	6.4

4.5.4 Variation of thermal parameters

To study the storage behaviour of a BTES with 61 BHEs in distances between 2 and 8 m under different subsurface conditions, thermal conductivity and heat capacity are varied within a range that is typical for Northern German sediments. In principle, heat transfer occurs at a higher rate in materials with a high thermal conductivity and more heat can be stored in materials with high heat capacity (when imposing the same temperature). In this work, thermal conductivity and heat capacity are varied individually, meaning that the respective other parameter is kept constant. The simulation results of the scenarios are first compared for the BTES with 5 m BHE distance after twenty years of heat storage.

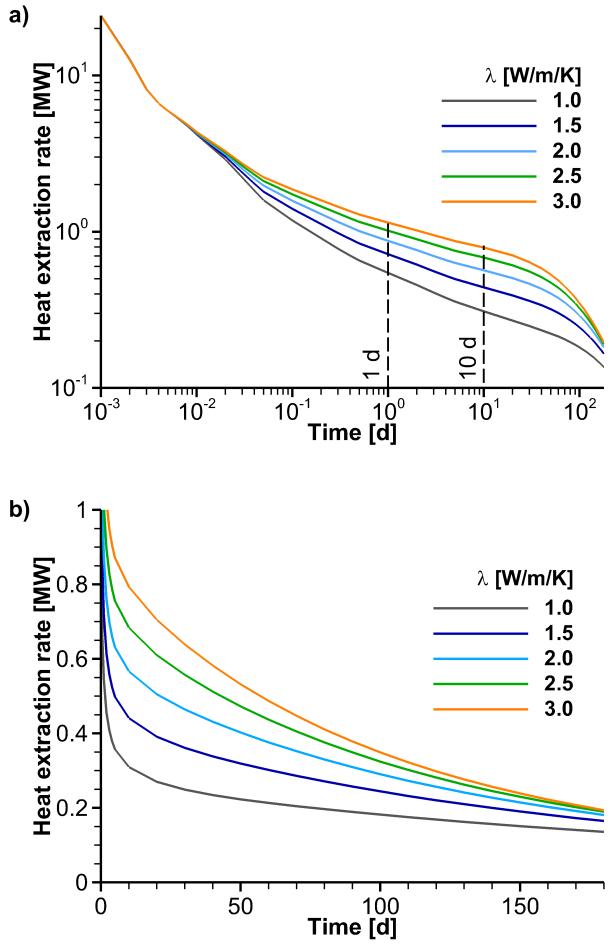

Fig. 4.19 *Heat extraction rate in the 20th heat storage cycle of all investigated thermal conductivities for the BTES with 61 BHEs in 5 m distance in log-log (a) and linear scale (cut above 1 MW) (b)*

Thermal conductivity

The role of thermal conductivity on heat transfer can be observed in the defined scenarios. For example, with higher thermal conductivity, the temperatures inside the storage are higher after heat injection and lower after heat recovery (Fig. 4.21, middle row). Except for the used area where temperatures are also lower after heat recovery, the temperatures in the subsurface outside the storage are generally are higher for higher thermal conductivities due to the improved heat transfer in direction of the temperature gradient. This also results in a higher heat extraction rate (Fig. 4.19).

With high thermal conductivity, the heat extraction rate drops much slower although in long-term the differences diminish. At the end of the heat recovery phase it is only marginally higher, i.e. the minimum value of the heat extraction rate is 7 % higher at a 50 % higher thermal conductivity compared to the base scenario. In contrast, the mean heat extraction rate is 26 % higher under this condition. The same applies to the mean heat injection rate and thus the amounts of injected and recovered heat (Fig. 4.20).

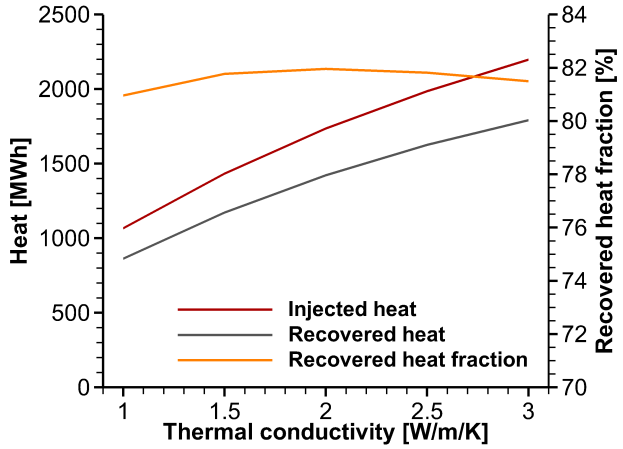

Fig. 4.20 *Injected and recovered heat over thermal conductivity with the corresponding recovered heat fraction in the 20th storage cycle*

Compared to the base scenario, the amounts of injected and recovered heat are higher by 26 % when the thermal conductivity increases by 50 % and lower by 39 % when the thermal conductivity decreases by 50 %. As a result, the recovered heat fraction is almost constant and only varies between 81 and 82 %. Consequently, surface loss and remaining heat fraction are almost constant as well, although the absolute amounts increase with increasing thermal conductivity, just like injected and recovered heat amounts. Only the surface loss fraction increases slightly for higher thermal conductivities because more heat is transferred away from the storage and thus elevates the temperature gradient between subsurface and top model boundary. These BTES with medium BHE distance are quite robust because the remaining heat is in balance. When the thermal

conductivity is low, more heat remains between the BHEs whereas with high thermal conductivity, less heat remains between the BHEs and more heat is transported outside the storage. For this reason, the influenced area is larger with higher thermal conductivities. With a thermal conductivity of 3.0 W m^{-1} K^{-1}, the influenced area's radius is 57 m, which is 4 m more than in the base scenario (Tab. 4.6). Therefore, the relation between influenced and used area increases. However, the change in used area is minor with the effect that with a high thermal conductivity, usable heat capacity and its fraction of the theoretical heat capacity increase.

To conclude, the recovered heat fraction of BTES systems with medium BHE distance is not sensitive to changes in thermal conductivity, but the amounts of injected and recovered heat scale linearly, because thermal conductivity drives the heat transfer. For this reason, used and influenced area increase with higher thermal conductivity.

Tab. 4.6 *Radius of influenced area, relation of additionally influenced area to used area, and usable heat capacity after the 20th storage cycle for the different thermal parameters*

		Influenced area		Usable heat
		Radius [m]	Relation* [-]	capacity [kWh m^{-3}]
λ	1.0	46	3.2	15.9
	2.0	53	3.8	13.8
	3.0	57	4.3	13.2
$c\rho$	1.0	58	4.1	9.4
	2.0	53	3.8	13.8
	3.0	50	3.5	16.1

*relation between additionally influenced and used area

To investigate if storages with smaller or larger BHE distances function in the same way, all possible combinations of thermal conductivity and BHE distance (in total 35 variations) are simulated in this work.

The results show that the temperatures barely vary with 2 m BHE distance in a different subsurface (Fig. 4.21). Regardless of the thermal conductivity, the storage is completely heated as the temperatures always reach almost 90 °C inside the storage after heat injection and is completely cooled down to 10 °C after heat recovery, because the storage volume mainly drives temperature distribution. Compared to the base scenario, the temperature variation inside the storage, which depends on subsurface thermal conductivity, is smaller with large BHE distances (Fig. 4.21, bottom row for a

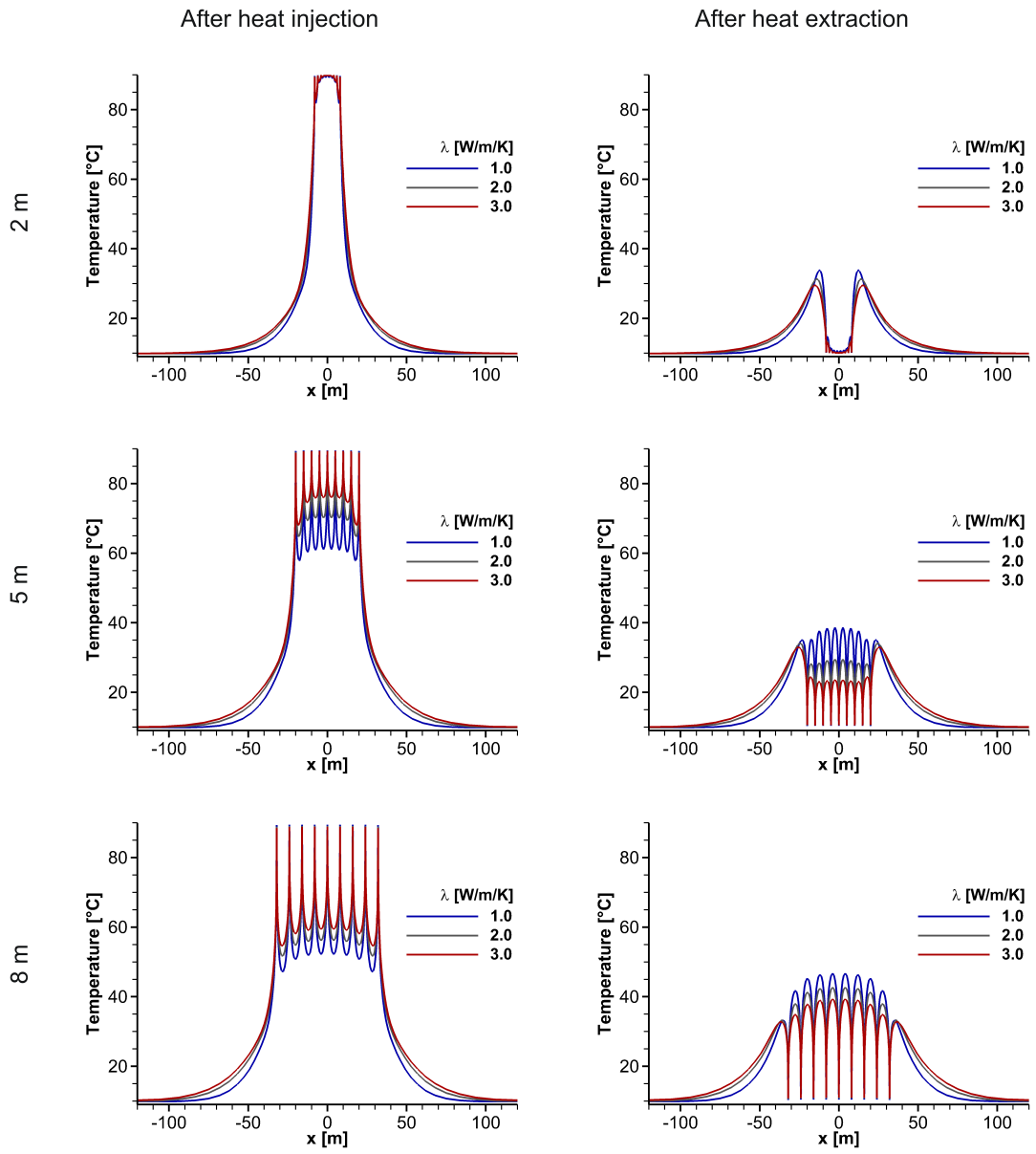

Fig. 4.21 *Temperature profiles through the storage centre along the x-axis after 20^{th} heat injection/recovery in a subsurface with different thermal conductivity for the BTES with 61 BHEs in 2, 5, and 8 m distance*

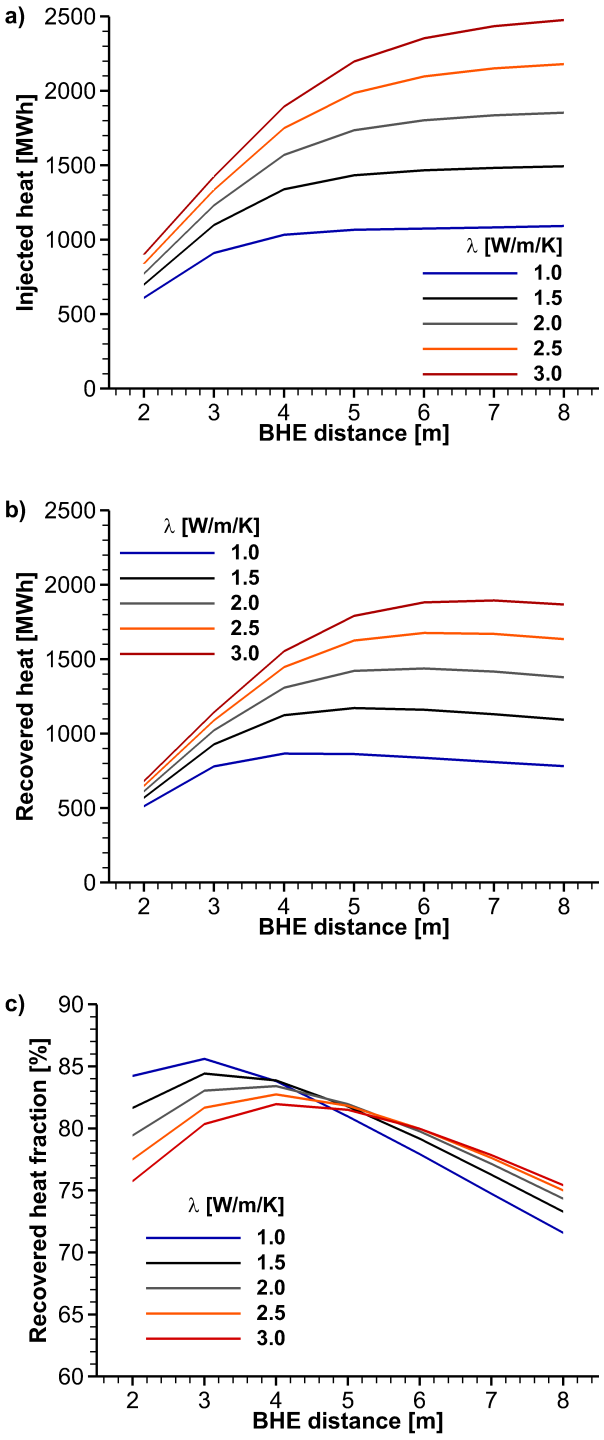

Fig. 4.22 *Injected heat (a), recovered heat (b), and recovered heat fraction (c) over BHE distance of all considered thermal conductivities for the BTES with 61 BHEs in the 20th storage cycle*

storage with 8 m BHE distance). The reason is that the storage volume is comparatively larger and it takes more time to heat up more material.

Furthermore, the amount of injected heat increases with increasing subsurface thermal conductivity as well as with increasing BHE distance (Fig. 4.22 a). For small BHE distances, the injected heat is more sensitive to changes in BHE distance, as it only changes marginally in a different subsurface. That means that the BHE distance limits the amount of heat that can be injected. The behaviour is reversed with high BHE distances and the increase depending on the thermal conductivity is more significant. The observation shows that the subsurface thermal conductivity is then a limiting factor. This leads to the injected heat maximum of 2,476 MWh at a thermal conductivity of 3.0 W m^{-1} K^{-1} and 8 m BHE distance. This is four times as high as the injected heat minimum of 610 MWh, obtained with a thermal conductivity of 1.0 W m^{-1} K^{-1} and 2 m BHE distance. Like the amount of injected heat, the recovered heat is always higher with higher thermal conductivity (Fig. 4.22 b). However, in contrast, the recovered heat maximum is never reached with a BHE distance of 8 m. Instead, the recovered heat depending on the BHE distance increases at first and then drops again for large BHE distances leading to an optimum BHE distance for each thermal conductivity value (Fig. 4.22 b). As well as the stored heat, the recovered heat is limited by the BHE distance for values smaller than 5 m and limited by the subsurface thermal conductivity when the BHE distances are larger. During heat recovery phase, the heat still spreads inside the storage away from the BHE. For this reason, the amount of recovered heat drops again for larger BHE distances as less heat can be regained but remains in the storage. The minimum amount of heat that can be recovered is 514 MWh with a thermal conductivity of 1.0 W m^{-1} K^{-1} and 2 m BHE distance. The absolute recovered heat maximum is achieved with a thermal conductivity of 3.0 W m^{-1} K^{-1} and 7 m BHE distance. With smaller thermal conductivity, the maximum is achieved with a smaller BHE distance, which is thus at an optimum between 3 m (for a thermal conductivity of 1.0 W m^{-1} K^{-1}) and 7 m (for a thermal conductivity of 3.0 W m^{-1} K^{-1}), depending on the given subsurface conditions.

In contrast to the BTES with 5 m BHE distance with its steady recovered heat fraction, BTES with smaller or larger BHE distance show deviations depending on the subsurface thermal conductivity (Fig. 4.22 c). The recovered heat fraction does not necessarily increase with increasing thermal conductivity. Instead, it decreases with increasing thermal conductivity when the BHE distance is 2 or 3 m, because more heat is lost to the subsurface. For BHE distances of 6 m or more, however, the fraction of recovered heat increases with increasing thermal conductivity. The reason is that in these large

storages more heat remains between the BHEs.

In a subsurface with small thermal conductivity, the portion of heat between the BHEs is even higher. In this defined setup, the absolute recovered heat fraction maximum of 85.6 % is achieved with a thermal conductivity of 1.0 W m^{-1} K^{-1} and BHE distance of 3 m. In general, the optimum BHE distance is smaller for the fraction of recovered heat as for recovered heat amount (between 3 and 4 m). The recovered heat fraction is more limited by the BHE distance than the thermal conductivity because the BHE distance controls the storage volume. Small storages with small BHE distances have a larger surface area and therefore lose more heat to the surrounding subsurface. Large storages with large BHE distances lose comparatively less heat to the surrounding but at the same time cannot be completely emptied during half a year of heat recovery. For this reason, medium large storages with a moderate surface-area-to-volume ratio and moderate heat losses yield higher recovered heat fractions.

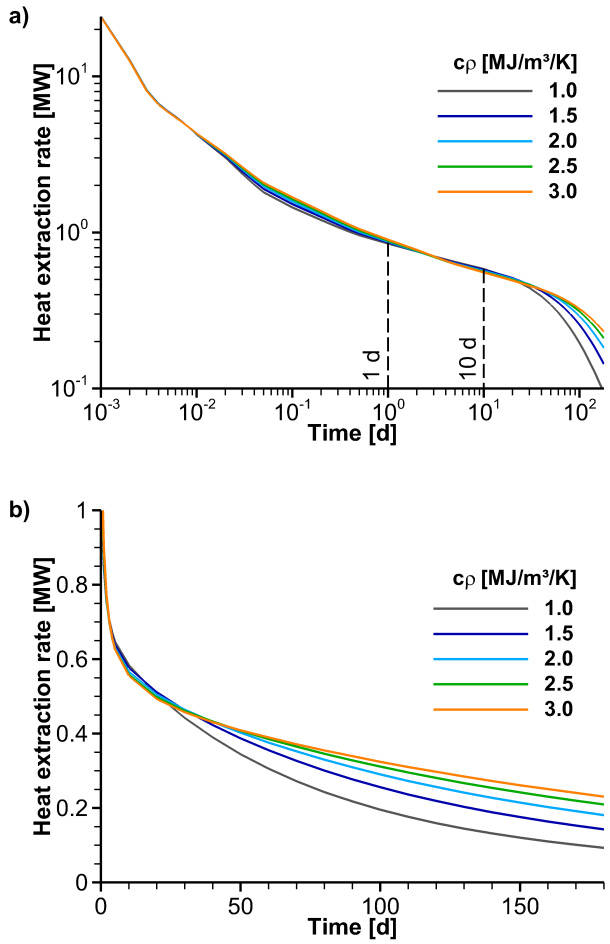

Fig. 4.23 *Heat extraction rate in the 20th heat storage cycle of all investigated heat capacities for the BTES with 61 BHEs in 5 m distance in log-log (a) and linear scale (cut above 1 MW) (b)*

Heat capacity

The approach used for thermal conductivity in the preceding paragraph is now applied to heat capacity based on the BTES with 5 m BHE distance. Again, all possible combinations between BHE distance and heat capacity are investigated afterwards (35 scenarios). The simulation results indicate that the heat capacity is especially affecting the heat transfer in the long-term. Here, the effect is demonstrated by the heat extraction rate (Fig. 4.23, for the 20^{th} heat recovery period).

In the beginning of heat recovery, the rate shows a similar trend in all curves, which means, heat transfer is not sensitive to heat capacity at this point. But over time, the differences between the curves grow and the heat extraction rate drops much slower with high heat capacity. At the end of the heat recovery phase the minimum value of the heat extraction rate is 28 % higher with a 50 % higher heat capacity compared to the base scenario. The reason is that heat conduction is slower, the BHEs start to interact later and more heat can be stored in the vicinity of the BHEs that is reachable with the given thermal conductivity. This results in smaller temperatures and thus higher heat extraction rates. Conversely, this means that more heat is recovered because more heat is available in the vicinity. Therefore, the amounts of injected and recovered heat increase with higher heat capacity (Fig. 4.24).

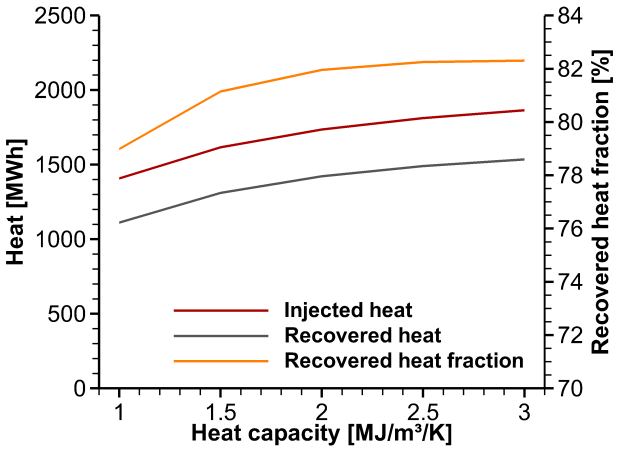

Fig. 4.24 *Injected and recovered heat over heat capacity with the corresponding recovered heat fraction in the 20^{th} storage cycle*

Compared to the base scenario, the increase of both is only about 7 % for a 50 % higher heat capacity. For a 50 % lower heat capacity, 19 and 22 % less heat can be injected and recovered. The recovered heat fraction then varies between 79 and 82 %. These minor changes arise from the surface loss that is higher with lower heat capacity because heat transfer is improved (Fig. 4.25). The remaining heat fraction is almost constant although it is distributed differently. With low heat capacity, heat is transported further

and remains outside the storage; with high heat capacity, heat remains between the BHEs. Changes in heat capacity are compensated by medium BHE distances so that the amounts of injected and recovered heat as well as the recovered heat fraction for storages with medium BHE distance do not react sensitive to them. Looking at storages with higher BHE distances, the storage characteristics are less affected by heat capacity.

Differences in the amounts of injected and recovered heat are only about 7 % at maximum in a subsurface with a 50 % lower heat capacity (Fig. 4.26 a and b). The reason is that the thermal conductivity is still the limiting factor. As demonstrated before, thermal conductivity controls the heat transfer, which reacts highly sensitive to changes of this parameter. Still, the influence of heat capacity on storages with higher BHE distances occur at a later stage in heat injection or recovery phase compared to the base scenario. This results from the fact that with a BHE distance of 8 m the storage and thus the space between the BHEs is larger and BHEs start to interact later. For this reason, the efficiency is small with large BHE distances and only varies marginally (less than 1 %) within the given range of heat capacity (Fig 4.26 c). In contrast, the amounts of injected and recovered heat in storages with smaller BHE distances react most sensitive to the subsurface heat capacity (Fig 4.26 a and b); the recovered heat (±36 %) responds even stronger than the injected heat (±29 %).

The reason is that with their small-scale storage volume, these BTES are always filled and emptied to their limit and the heat capacity scales the amounts of heat. In addition, the heat capacity delays heat loss into the surrounding subsurface. The impact is highest with small BHE distances and hence, the recovered heat fraction rises from 71 to 83 % when the heat capacity increases from 1.0 to 3.0 MJ m^{-3} K^{-1} (Fig. 4.26 c).

To sum up, the extraction rate and thus recoverable heat amounts are enhanced by higher thermal conductivity and higher heat capacity but the influence of thermal conductivity is more important in the investigated scenarios where heat conduction is the dominant process. At BHE distances of around 4 m and more, the thermal conductivity is the limiting factor for heat recovery. With BHE distances smaller 4 m, the recoverable heat is mostly controlled by the distances itself and the amounts are generally lower. Thus, medium large systems in a subsurface with high thermal conductivity (and heat capacity) are preferable for gaining the highest absolute amounts of heat. In contrast, regarding recovered heat fraction and usable heat capacity, the sensitivities reverse and recovered heat fractions of small storages are mainly affected by thermal parameters. Then, the heat capacity is the main constraining parameter.

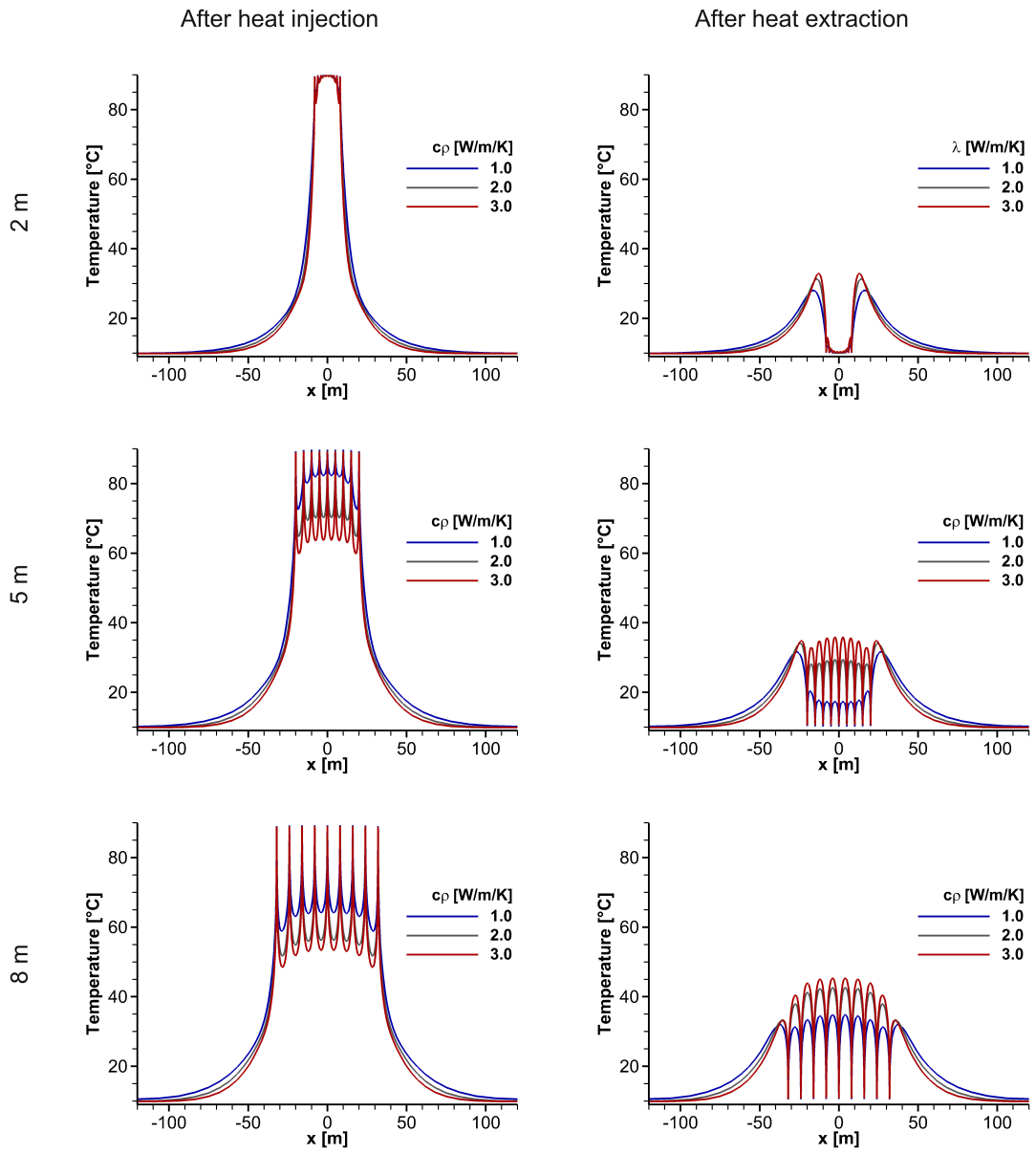

Fig. 4.25 *Temperature profiles through the storage centre along the x-axis after 20^{th} heat injection/recovery in a subsurface with different heat capacity for the BTES with 61 BHEs in 2, 5, and 8 m distance*

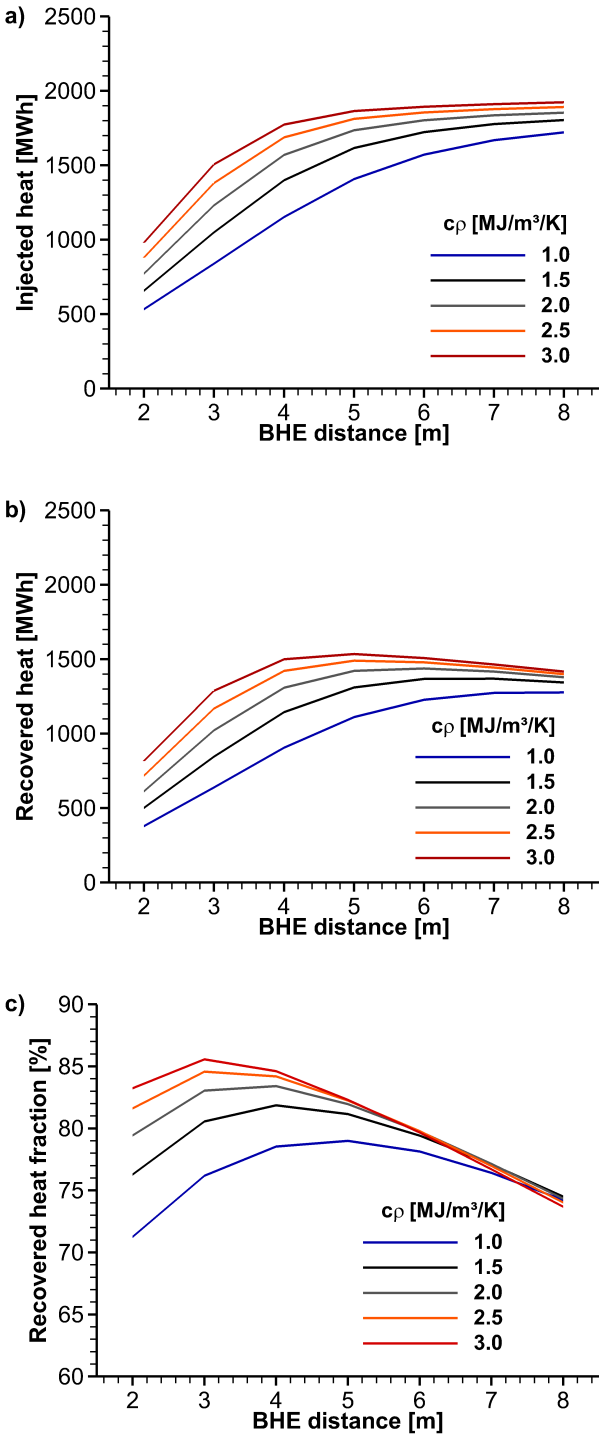

Fig. 4.26 *Injected heat (a), recovered heat (b), and recovered heat fraction (c) over BHE distance of all considered heat capacities for the BTES with 61 BHEs in the 20th storage cycle*

In larger BTES systems, recovered heat fractions are only sensitive to the BHE distance. Recovered heat fraction and usable heat capacity correlate and both reach their optimum with small BHE distances in a subsurface of low thermal conductivity and high heat capacity. Finally, induced temperatures and influenced volume mainly depend on the BHE distance and less on the thermal parameters of the subsurface.

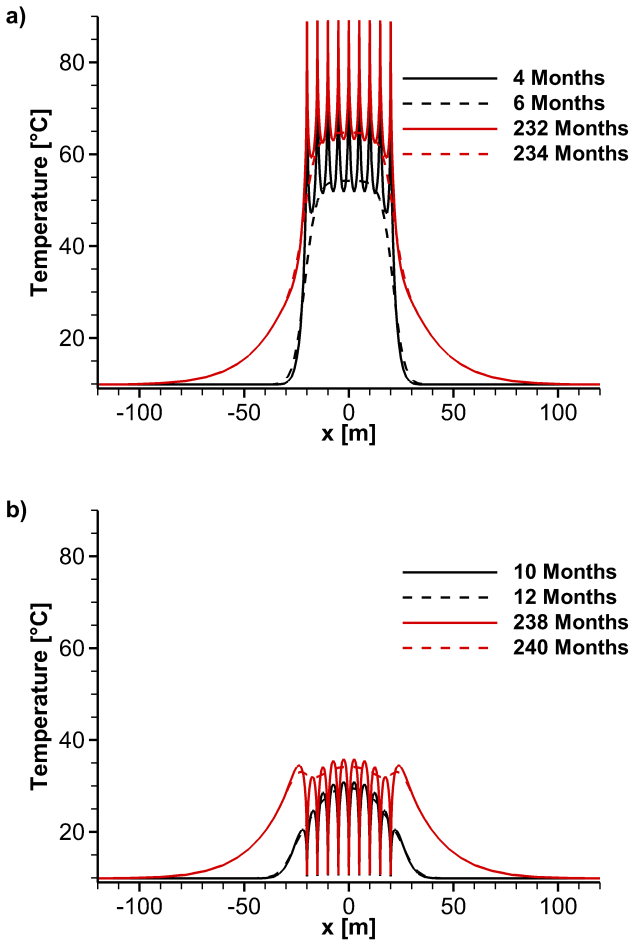

Fig. 4.27 *Temperature profiles through the storage centre along the x-axis for the scenario with alternative storage operation mode after 1^{st}, 5^{th}, 10^{th}, and 20^{th} heat injection (a) and recovery (b) as well as after respective two months long operation pause*

4.5.5 Variation of storage operation mode

The previously hypothesised strictly biannual storage mode for the BTES system operation, where heat is injected at a constant inlet temperature for six months and afterwards recovered for six months, is not a realistic scenario. Instead, heat availability and demand control the storage operation mode and inlet temperatures. During warm months (~May to August), usually more heat is available for injection while during cold months

(~November to February) the heat demand is high. During the months in between, both availability and demand are lower although not necessarily zero and the transitions are indistinct. For practical implementation in the numerical model, this behaviour is approached here by simulating a scenario with each four months of injection/recovery and a two-months-long pause in between the two storage phases. After four months of heat injection or recovery, no further heat is introduced or obtained with the considered scenario. From this point, heat transfer depends on the temperature gradients then and on the same thermal parameters as in the base scenario. The scenarios are evaluated regarding storage characteristics and effects and then compared to the base scenario.

The period of heat injection or recovery is obviously smaller by one third in comparison to the base scenario. Therefore, less heat can be introduced to the subsurface during the heat injection period and the storage temperatures are generally lower after heat injection (Fig. 4.27 a), i.e. around 51 °C after the first injection and stabilise to 62 °C after the fifth injection. Then, heat is transported by heat conduction only and the temperature gradients around the BHEs are equalised as no further heat is injected. After six months, the peaks have thus been flattened while the temperature signal towards the model boundaries has increased. The reverse effect is observed after heat recovery when temperatures in the storage are comparatively higher with 29 °C after the first heat recovery and increase much more than in the base scenario to 35 °C from the fifth recovery (Fig 4.27 b). As for the pause after heat injection, the peaks are flattened when no further heat is recovered while the remaining heat moves away from the storage.

A two-months-long pause leads to an equalisation of the temperature gradients in the pipes as well (Fig 4.28 a). In the pause after heat injection, temperatures drop significantly due to the redistribution of heat through conduction and for the same reason rise in the pause after heat recovery. This is more pronounced in outer BHEs because the temperature gradients are steeper there and it results in smaller temperature differences when storage mode switches from pause to operation.

For this reason, the initial heat injection/extraction rate is lower compared to the base scenario but the rate also decreases exponentially and shows a similar trend (Fig 4.28 b). Due to the nature of this development, and because the mean heat injection rate corresponds to an operation time of only four months, with 0.43 MW and it is 8 % higher than in the base scenario. Following this logic, the mean heat extraction rate should be higher as well. However, due to the two-months-long pause, the heat loss is larger and the mean rate is 0.33 MW, the same as in the base scenario (Fig 4.28 c).

Because these high(er) obtained mean rates are only the result of a smaller operation

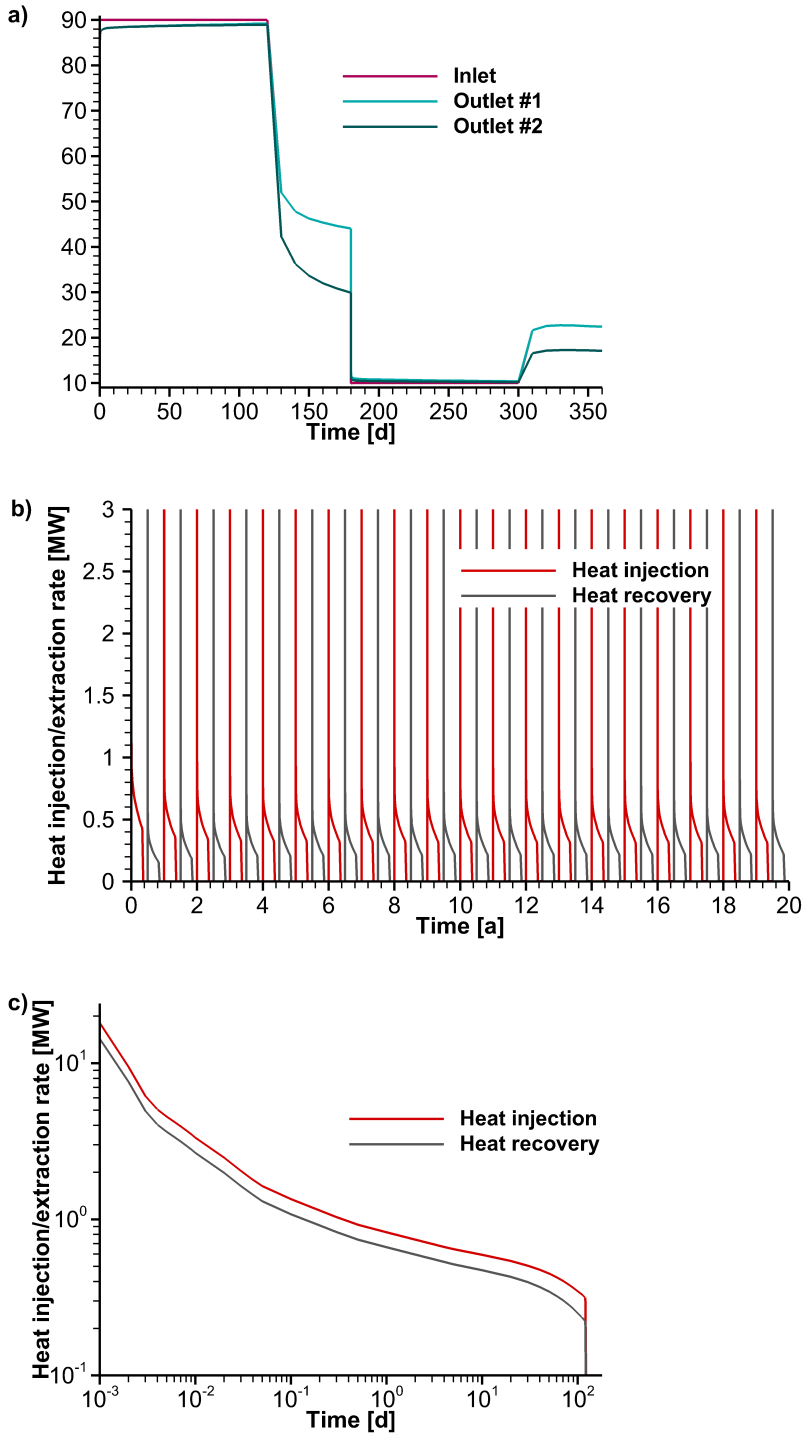

Fig. 4.28 *Pipe inlet and outlet temperatures for the inner and a marginal pipe during heat injection and recovery of the scenario with alternative storage operation mode (a), long-term behaviour of total heat injection and extraction rate during alternating heat injection and recovery (b) and development of total heat injection and extraction rate with corresponding mean rates in the 20th heat storage cycle (c)*

time of four months, they do not result in higher total injected or recovered amounts of heat. During the first heat injection, the amount of injected heat is still two thirds of the amount injected with the base scenario. Additional heat loss occurs during the two-months-long pause, because high temperature gradients inside the storage are reduced and heat is transported away from the storage towards the model boundaries. This results in a reduction of the amount of recovered heat already in the first recovery by 41 % compared to the base scenario and further to a reduction of recovered heat fraction by 12 %. Nevertheless, the amounts of injected and recovered heat as well as the recovered heat fraction show the same development like the base scenario (Fig 4.29). After 20 years of operation, 1,252 MWh are injected and 952 MWh are recovered leading to a recovered heat fraction of 76 %, which is 6 % lower than with the base scenario. (Fig 4.30). The 6 % heat loss compared to the base scenario is not divided equally between surface loss and remaining heat. Disproportional more heat remains compared to the base scenario because of its redistribution in the subsurface during the storage operation pause. This is especially established during the first years of heat storage when the remaining heat fraction is high; after the first year it is even higher than the recovered heat fraction.

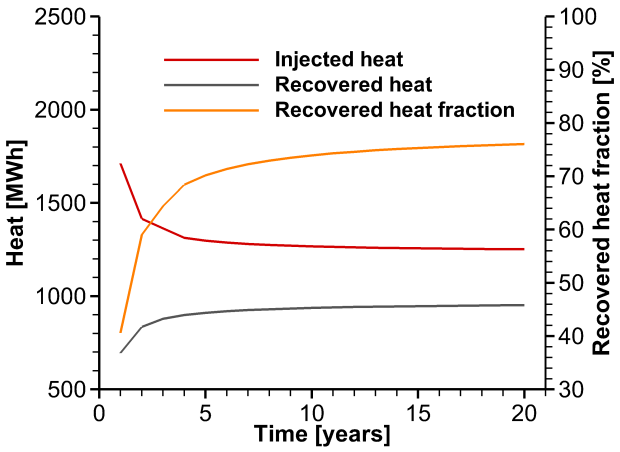

Fig. 4.29 *Injected and recovered heat over time with the corresponding recovered heat fraction for the scenario with alternative storage operation mode in the 20th storage cycle*

Heat transport in the subsurface is driven by the thermal parameters of the subsurface and the temperature gradient. After four months of heat injection or recovery, this temperature gradient is the same in both variations of the storage operation mode. Although no further heat is introduced with the observed scenario then, the heat transfer is driven by the same thermal parameters as with the base scenario. For this reason, in this scenario, the area that is influenced by the storage is only 4 % smaller than with the base scenario (Fig 4.31 a and b), although 30 % less heat is introduced to the subsurface in total. The same applies for the area that is used by the storage, but to a lesser extent

because of the comparatively shorter heat recovery period. Here, the volume is smaller by around 8 %.

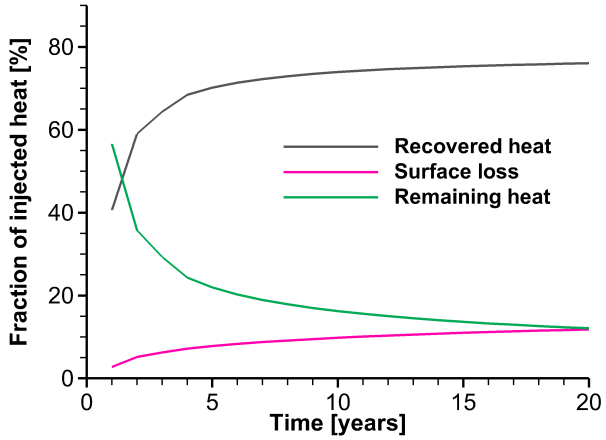

Fig. 4.30 *Accumulation of the amounts of recovered heat, surface loss and remaining heat over time for the scenario with alternative storage operation mode in the 20th storage cycle*

Again, thermal conductivity and heat capacity are varied within the defined range to compare the storage behaviour of a BTES with 61 BHEs in distances between 2 and 8 m in different storage operation modes. First, amounts of injected and recovered heat as well as recovered heat fraction are investigated for different subsurface thermal conductivities (Fig. 4.32 a-c). Then, the results are analysed for varying heat capacities (Fig 4.33 a-c). A comparison of the two storage operation modes shows that the storage behaves in a similar pattern even when the operation mode is paused in between and thus the effect of thermal parameters on the storage characteristics is similar. The difference is that, concerning small BHE distances, with higher thermal conductivity or lower heat capacity the heat transport into the storage surrounding subsurface and towards the model boundaries is improved during the two months of operation break. Regarding high BHE distances, lower thermal conductivities or higher heat capacities only cause a compensation of the temperature peaks during the operation break. For these reasons, injected and recovered heat amounts do not scale linearly with operation time (i.e. with the investigated scenario the amount of recovered heat is smaller than the amount of heat recovered over four months with the base scenario).

Thus, the recovered heat fraction additionally decreases and even more heat is lost then. Although the recovered fractions are up to 10 % lower compared to the base scenario, the optimal BHE distance is similar. For example, the maximum recovered heat fractions in a subsurface with thermal conductivity of 1.0 or 3.0 W m^{-1} K^{-1} are still achieved with BHE distances of 3 or 4 m, respectively. In summary, the absolute amounts of injected and recovered heat are lower and so is the recovered heat fraction for the scenario of

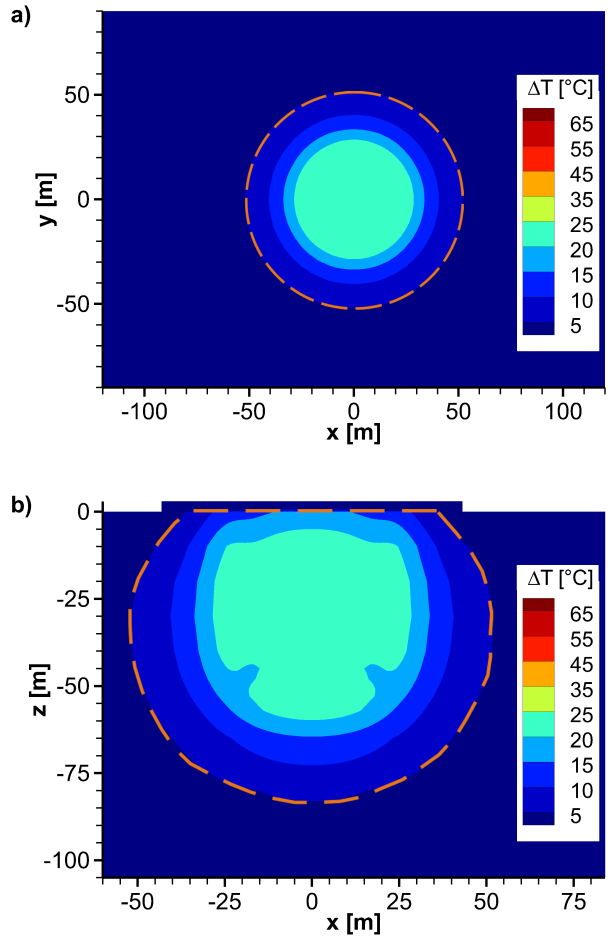

Fig. 4.31 *Difference between temperature distribution after the last two-months-long pause (20 years) and the initial condition of the scenario with alternative storage operation mode as horizontal (a) and vertical (b) slice through the storage centre with the corresponding volume with 5 °C temperature difference (orange)*

four months of heat injection/recovery and a two-months-long pause in between. Thus, the system is less efficient while it influences the same subsurface volume because of an increased heat loss.

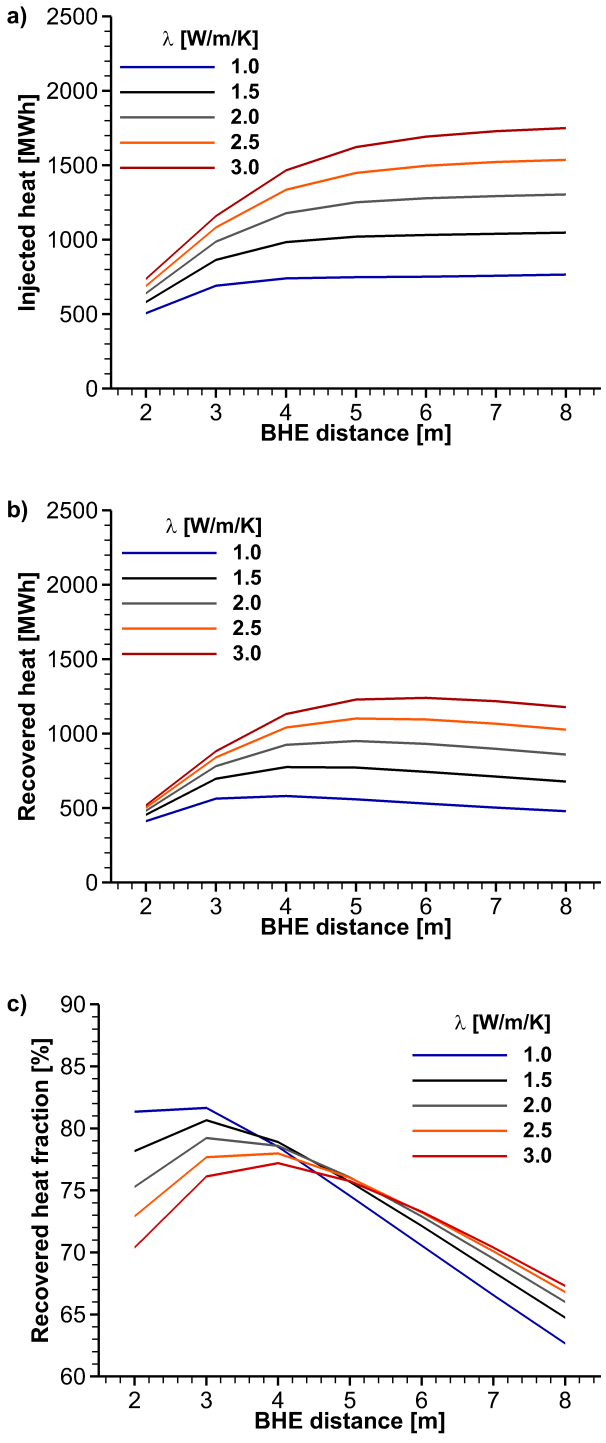

Fig. 4.32 *Injected heat (a), recovered heat (b), and recovered heat fraction (c) over BHE distance of all considered thermal conductivities for the scenario with alternative storage operation mode in the 20^{th} storage cycle*

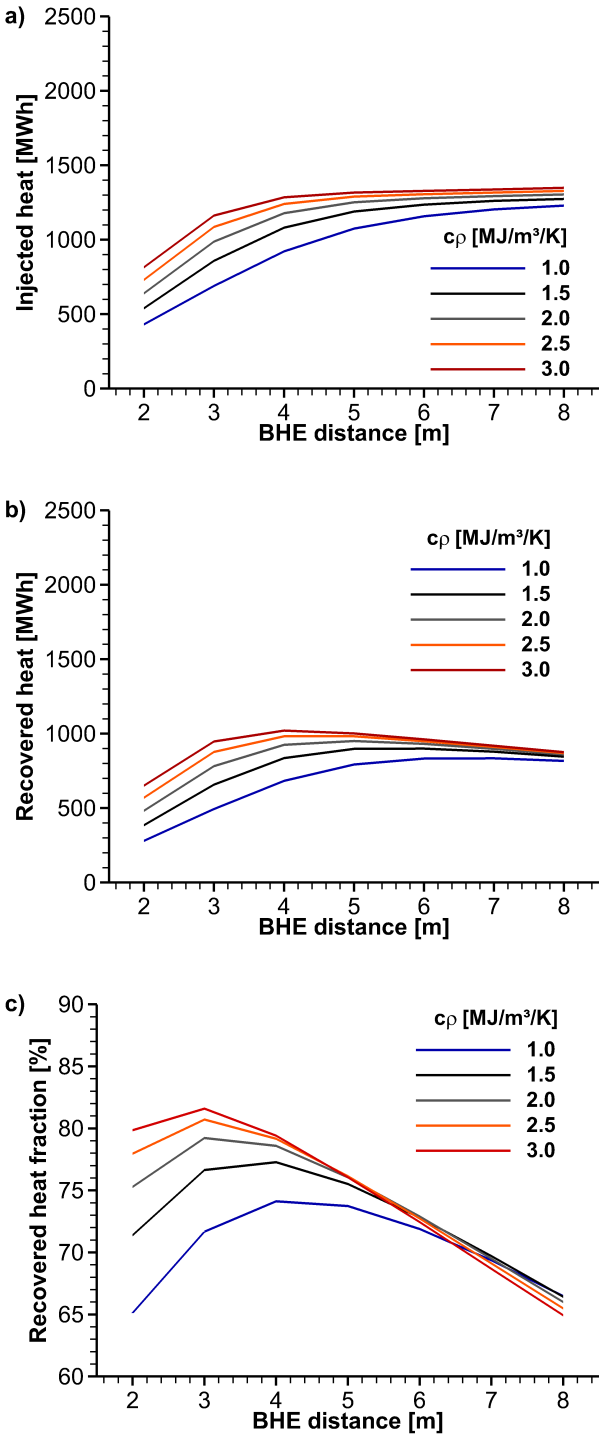

Fig. 4.33 *Injected heat (a), recovered heat (b), and recovered heat fraction (c) over BHE distance of all considered heat capacities for the scenario with alternative storage operation mode in the 20th storage cycle*

4.6 Discussion

Numerical simulations of heat transfer are performed in this work to study storage behaviour with different storage properties and its effects on the geological subsurface. High-temperature BTES systems are simulated respresenting all BHEs with geometric detail and high resolution in the numerical model for a correct representation of the governing processes. Because of this level of detail, simulations are time-consuming, but can consider all possible constraints. The assumptions made in the numerical model concerning the storage operation mode with constant inlet temperatures but also in terms of subsurface properties or model boundary conditions allow to test the storage setup and draw generalised conclusions, which help to understand the system's behaviour. Moreover, numerical simulations are necessary to predict a particular BTES's storage characteristics and impacts for the local conditions. The numerical simulation approach used in this work alows for such specific details and conditions to be included.

Variations of subsurface thermal parameters and storage properties show that the system is robust in terms of recovered heat fraction variety when heat transport in the subsurface is solely conductive. In most cases, the recovered heat fraction varies between 75 and 85 %. The recovered heat fractions in the investigated systems therefore reach similarly high levels as the "utilization ratio" specified in VDI 4640 Part 3 (2001) and recovered heat fractions of a real storage site in Neckarsulm, Germany, where 69 % are achieved (Bauer et al. 2013a). Compared to BTES systems in Annenberg, Sweden (46 % after eight years of operation, Heier et al. 2011) or Drake Landing, Canada (54 % after four years, Sibbitt et al. 2012) significantly higher recovered heat fractions are observed, even after four and eight years. One reason is the storage operation mode where heat is injected for six months and then directly recovered. In the alternative scenario with two months standstill between four months of injection and recovery, recovered heat fractions are around 5 % lower compared to their equivalent scenarios. Thus, the main reasons for higher recovered heat fraction are the high temperature during heat injection as well as the high temperature difference between injection and recovery. Most BTES systems are discharged with comparatively high temperatures around 30 °C. Because 10 °C are used in the scenarios, the temperature gradient between fluid and storage formation is higher leading to higher storage efficiencies. The same effect is observed in Brædstrup, where discharging is performed at 12 °C, producing a storage efficiency of almost 65 % despite its small storage volume. The results show further that these high values can be gained even with small storage volume of ~$10,000\,\mathrm{m}^3$ or less, although small BTES systems tend to have unfavourable surface-area-to-volume ratios. In addition to the recovered heat fraction, performances of BTES systems can

be compared by the specific heat extraction rate (Welsch et al. 2016), which is derived from the mean rate of one extraction period and the total length of all BHEs together

$$Specific\ heat\ extraction\ rate = \frac{Mean\ heat\ extraction\ rate}{BHE\ number \times BHE\ length}$$

It is found that specific heat extraction rates are controlled by several factors (Fig 4.34). Besides subsurface conditions, the BHE number and BHE distance have to be considered when implementing a BTES system. In the observed scenarios, specific heat extraction rates of up to 135 W m^{-1} can be obtained, which is within a similar range as observed by Welsch et al. (2016). Compared to the rough starting values given in VDI 4640 Part 3 (2001) this is twice as much, because those values were originally given in VDI 4640 Part 2 (2001) for shallow heating-only single BHE systems. The extracted heat per meter borehole is affected by the temperature as well.

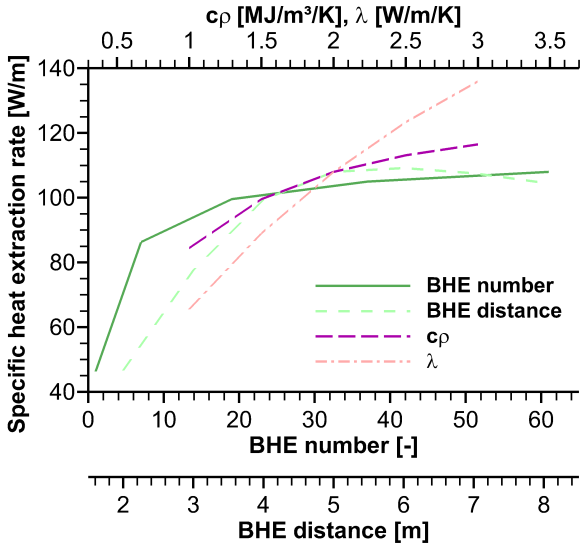

Fig. 4.34 *Specific heat extraction rate depending on BHE number, BHE distance or thermal parameters during the 20th heat extraction. BHE distance and thermal parameters are analysed for the BTES with 61 BHEs*

For example, the Brædstrup BTES reaches 0.36 and 0.24 MWh per borehole metre during heat injection and recovery, using temperatures of around 50 and 12 °C, respectively. The Crailsheim storage only achieves 0.18 and 0.09 MWh/m in comparison with temperatures of 60 and 30 °C. This emphasizes that high temperature differences between working fluid and subsurface are favourable for heat storage.

Here, the main reasons for high specific heat extraction rates and recovered heat fractions are the defined storage layout with BHEs connected in parallel and the storage operation mode using a large temperature difference between the pipe's inlet and outlet. In a real setting, the specific heat extraction rate may probably be lower, because recovery temperatures are commonly higher and injection/recovery cycles fluctuate.

Low specific heat extraction rates correlate with small storage volumes, resulting either from small BHE number or from small BHE distance. Only then, the values given in VDI 4640 Part 2 (2001) can function as reference. However, comparison of the results of two BTES systems with the same volume yet different BHE number and distance reveals that the specific heat extraction rate can only serve as indicator for the actual performance of a BTES. For example, the system with 37 BHEs in 5 m distance achieves a higher specific heat extraction rate because of its larger BHE distance. Nevertheless, both absolute amount of recovered heat and recovered heat fraction are higher in a system with 61 BHEs in 4 m distance, because the BHE number is 1.6 times higher then. Again, this demonstrates that besides the surface-area-to-volume ratio the storage design is an important factor. Also, this shows that storage behaviour of even larger BTES systems cannot easily be extrapolated, but need to be assessed by simulations of their individual setup.

With numerical simulations, optimum BHE distances can be determined under different conditions (Tab 4.7, using the example of a BTES with 61 BHEs operated in a biannual injection/recovery cycle). The results show that with the given simplified boundary conditions and subsurface parameterisation, the optimum varies depending on the regarded aspect that is considered most important. For example, when subsurface thermal conductivity is 2 W m^{-1} K^{-1}, the highest recovered heat amount is reached with 6 m BHE spacing, while the recovered heat fraction is highest with 4 m. The highest usable heat capacity is reached with 3 m BHE distance here. In this example, the specific heat extraction rate is proportional to the recovered heat amount, because BHE length and number are constant. However, the heat extraction rate changes during half a year of heat recovery. Therefore, one aim could be an consistently high heat extraction rate. This can refer either to the maximum average value or minimum average slope. The first is reached using 6 m BHE spacing with the given scenario, the latter is always reached with the largest chosen BHE distance of 8 m, because thermal interaction between the BHEs is smallest then. With future subsurface planning, especially in urban areas where different storage options are potentially installed in close proximity, an overall low thermal impact (i.e. low storage temperature after heat injection) of the BTES system as well as a small impacted area could be possible aims in the design process. Both aims are achieved with the largest used BHE distance of 8 m in the given example.
Analysis of the optimum BHE distance shows that in a prescribed subsurface different aims cannot be reached with one BHE distance and compromises must be found when the dimensions of the storage are determined. This means again that each particular storage scenario has to be investigated individually. Nonetheless, as in this work thermal conductivity and heat capacity of the subsurface have been studied separately, in reality

Tab. 4.7 *Optimal BHE distances to reach the individual aims in different subsurface thermal conductivities with a BTES of 61 BHEs operated in a biannual injection/recovery cycle*

		Constraint (λ [W m^{-1} K^{-1}])				
		1.0	1.5	2.0	2.5	3.0
Aim	High recovered heat amount	4 m	5 m	6 m	6 m	7 m
	High recovered heat fraction	3 m	3 m	4 m	4 m	4 m
	High usable heat capacity	2 m	2 m	3 m	3 m	4 m
	Consistently high rates*	5/8 m	5/8 m	6/8 m	6/8 m	6/8 m
	Low storage temperature	8 m	8 m	8 m	8 m	8 m
	Small influenced volume	8 m	8 m	8 m	8 m	8 m

*first: maximum average value, second: minimum average slope

they will be given by the geological subsurface available as storage formation. The approach used here would be a suitable approach for considering that. In addition to the parameters investigated here, the detailed representation of the BHE, with for example grout material or borehole diameter, as well as the exact storage operation mode will influence the BTES systems characteristics. In the scenarios of this work, the grout's thermal conductivity is relatively high, so it does not strongly limit the heat exchange with the subsurface. Furthermore, the flow rate of the heat carrier fluid is high. causing a high temperature gradient during most of the operation time. Variability of those settings is very high, so that a general investigation of these factors is not possible here, but has to performed for an individual site with given constraints.

4.7 Conclusions

- Numerical simulations prove to be required for assessing the impacts of high-temperature BTES systems on the subsurface. The numerical model is thus equally able to predict the temperature development beyond the operation of the BTES system.
- All investigated storage systems supply high specific rates given the applied high temperatures and are able to provide heat for a residential complex of around 8 houses (depending on their size).
- The BTES system always affects a significantly larger area than it actually needs for operation.

- Small storage system are more suitable for short-term heat storage, while medium sized storage systems with higher rates are suitable for seasonal heat storage. Large storage systems are preferable when the temperature impact must be kept at a low level.
- The optimal dimensions of the BTES (especially the BHE distance) can be obtained by numerical simulation and depend on the predefined constraints and aims of the storage.

5 Conclusions

BTES system are an increasingly used technology to seasonally store heat in the geological subsurface. In this thesis, numerical scenario simulations are used to assess the environmental impacts of BTES systems when high temperatures are applied. The simulations also help to extrapolate dependencies between constraining factors and optimal storage dimensions. Numerical simulations are necessary to quantify the ongoing coupled hydraulic and thermal processes that are induced in the subsurface by the heat storage. A realistic prediction of the interaction between grout, pipe and subsurface material parameters and thus of the transient behaviour of the storage processes requires a detailed representation of the BHE geometry. To ensure a correct characterisation not only in case of a singular BHE but also for large-scale BTES consisting of multiple BHEs, an efficient numerical model with feasible computation times is needed. So far, only highly discretised or greatly simplifying models exist, that either require immense computation time or neglect the full geometry of the BHEs. Consequently, a modelling approach is developed and validated in the thesis that diminishes the computation time and still includes all BHE components in the model. The introduced adapted model is valuable for quantifying and comparing the temperature impacts of different BTES setups in the subsurface and for deriving optimal storage dimensions under different subsurface conditions. Concerning these operation requirements, the model serves as a decision making tool for large storage projects. Based on the here described procedure, the major conclusions of this thesis are:

- Scenario simulations with an individual BHE show that the permeability of the storage formation has to be considered, especially when high temperatures are applied. In formations with high permeability, thermally induced convection may occur, enhancing heat transfer between BHE and subsurface with more heat being injected, resulting in an uneven and non-reversible heat plume in the subsurface. In consequence, the storage efficiency drops greatly. To prevent induced convection with a real storage site, a site evaluation with identification of the storage formation's hydraulic parameters is thus crucial.

- Comparison with experimental data shows that a correct representation of the interaction between the BHE components and the subsurface is crucial for a realistic prediction of heat balances and a reliable quantitative description of induced effects.

- Model validation proves that the adapted modelling approach developed in this thesis for reducing computation time to a viable minimum is able to BHEs with

only small deviations in terms of heat balance and induced effects. The developed modelling approach can thus also serve as a basis for validating other models (Schulte et al. 2016b).

- Simulations show that BTES is a feasible storage option. The estimated storage capacities can support up to 200 households with the given storage cycle at mean heat extraction rates between 0.1 and 0.4 MW. The thus achieved heat supply is similarly high as with existing BTES systems in Luleå or Neckarsulm.

- A structured approach for finding an optimum BHE distance is developed and its practical applicability is shown in this work. In this context, the optimum varies depending on the specific aim that is considered most important. Each aim can be reached with a respective BHE distance but at the same time, compromises need to be accepted to reasonably combine the achievable competing storage requirements.

- One possible storage aim that has hardly been considered in previous work but is identified as an important factor for subsurface spatial planning is a low thermal impact. With scenario simulations, the effects of BTES on the subsurface can be quantified. Temperature impact can be significant, with temperatures inside the storage about as high or low as the BHE fluid temperatures and average storage temperatures reaching up to 70 °C. This can lead to an impacted volume that is considerably higher than the actual storage volume, depending on the criterion used for delineating the volume impacted. Thermal impact should thus be considered in the dimensioning of a BTES system, especially when high temperatures are applied.

The simulation results in this thesis are grounded on simplifying assumptions regarding storage operation and subsurface properties, thus providing basic information about thermal and hydraulic behaviour of high-temperature heat storage. This is essential to eliminate unwanted effects in the comparison of the different simulation results caused by heterogeneities or uncertainties. For simulation of a real storage site, however, a thorough field data exploration is required and site-specific simulations using the approach developed in this thesis can be performed to assess storage capacities, achievable rates and estimate the thermally impacted subsurface volume. Scenario simulations as used in this thesis are essential for gaining a thorough system understanding as well as for characterisation and dimensioning of BTES systems and quantification of their impacts in the subsurface and thus should be applied to support the realisation of high-temperature BTES projects in urban areas, especially with future subsurface spatial planning in the context of the energy transition.

References

Abdelaziz, S. L., Ozudogru, T. Y., Olgun, C. G., & Martin, J. R. (2014). Multilayer finite line source model for vertical heat exchangers. *Geothermics*, *51*, 406–416. doi:10.1016/j.geothermics.2014.03.004

AGEB. (2013). *Anwendungsbilanzen für die Endenergiesektoren in Deutschland in den Jahren 2011 und 2012 mit Zeitreihen von 2008 bis 2012*. Arbeitsgemeinschaft Energiebilanzen e.V., Berlin, Germany.

AGEB. (2019). *Energieverbrauch in Deutschland: Daten für das 1. - 4. Quartal 2018*. Arbeitsgemeinschaft Energiebilanzen e.V., Berlin, Germany.

Bandos, T. V., Montero, Á., Fernández, E., Santander, J. L. G., Isidro, J. M., Pérez, J., ... Urchueguía, J. F. (2009). Finite line-source model for borehole heat exchangers: Effect of vertical temperature variations. *Geothermics*, *38*(2), 263–270. doi:10.1016/j.geothermics.2009.01.003

Başer, T., & McCartney, J. S. (2020). Transient evaluation of a soil-borehole thermal energy storage system. *Renewable Energy*, *147*, 2582–2598. doi:10.1016/j.renene.2018.11.012

Bauer, D., Heidemann, W., Marx, R., Nußbicker-Lux, J., Ochs, F., Panthalookaran, V., & Raab, S. (2009). *Solar unterstützte Nahwärme und Langzeit-Wärmespeicher (Juni 2005 bis Juli 2008)*. Stuttgart, Germany.

Bauer, D., Marx, R., Nußbicker-Lux, J., Ochs, F., Drück, H., & Heidemann, W. (2013a). *Solarthermie2000plus: Wissenschaftlich-technische Begleitung des Förderprogramms Solarthermie2000plus zu solar unterstützter Nahwärme und Langzeit-Wärmespeicherung (August 2008 bis September 2012)*. Stuttgart, Germany.

Bauer, D., Marx, R., Nußbicker-Lux, J., Ochs, F., Heidemann, W., & Müller-Steinhagen, H. (2010). German central solar heating plants with seasonal heat storage. *Solar Energy*, *84*(4), 612–623. doi:10.1016/j.solener.2009.05.013

Bauer, S., Class, H., Ebert, M., Feeser, V., Götze, H., Holzheid, A., ... Dahmke, A. (2012). Modeling, parameterization and evaluation of monitoring methods for CO2

storage in deep saline formations: The CO2-MoPa project. *Environmental Earth Sciences*, *67*(2), 351–367. doi:10.1007/s12665-012-1707-y

Bauer, S., Beyer, C., Dethlefsen, F., Dietrich, P., Duttmann, R., Ebert, M., ... Dahmke, A. (2013b). Impacts of the use of the geological subsurface for energy storage: An investigation concept. *Environmental Earth Sciences*, *70*(8), 3935–3943. doi:10.1007/s12665-013-2883-0

Bauer, S., Pfeiffer, T., Boockmeyer, A., Dahmke, A., & Beyer, C. (2015). Quantifying induced effects of subsurface renewable energy storage. *Energy Procedia*, *76*, 633–641. doi:10.1016/j.egypro.2015.07.885

Bayer, P., de Paly, M., & Beck, M. (2014). Strategic optimization of borehole heat exchanger field for seasonal geothermal heating and cooling. *Applied Energy*, *136*, 445–453. doi:10.1016/j.apenergy.2014.09.029

Bear, J., & Bachmat, Y. (1990). *Introduction to modeling of transport phenomena in porous media , volume 4*. Kluwer Academic Publishers.

Bear, J. (2007). *Hydraulics of groundwater*. OCLC: ocm71275659. Mineola, N.Y: Dover Publications.

Beck, M., Bayer, P., de Paly, M., Hecht-Méndez, J., & Zell, A. (2013). Geometric arrangement and operation mode adjustment in low-enthalpy geothermal borehole fields for heating. *Energy*, *49*, 434–443. doi:10.1016/j.energy.2012.10.060

Beier, R. A. (2014). Transient heat transfer in a u-tube borehole heat exchanger. *Applied Thermal Engineering*, *62*(1), 256–266. doi:10.1016/j.applthermaleng.2013.09.014

Beier, R. A., Smith, M. D., & Spitler, J. D. (2011). Reference data sets for vertical borehole ground heat exchanger models and thermal response test analysis. *Geothermics*, *40*(1), 79–85. doi:10.1016/j.geothermics.2010.12.007

Benner, M., Bodmann, M., Mangold, D., Nußbicker, J., Raab, S., Schmidt, T., & Seiwald, H. (2003). *Solar unterstützte Nahwärmeversorgung mit und ohne Langzeit-Wärmespeicher: Forschungsbericht zum BMBF/BMWA-Vorhaben (November 1998 bis Januar 2003)*. OCLC: 249932754. Stuttgart, Germany.

Beyer, C., Popp, S., & Bauer, S. (2016). Simulation of temperature effects on groundwater flow, contaminant dissolution, transport and biodegradation due to shallow geothermal use. *Environmental Earth Sciences*, *75*(18), 1244. doi:10.1007/s12665-016-5976-8

BMUB. (2016). *Climate Action Plan 2050: Principles and goals of the German government's climate policy*. Federal Ministry for the Environment, Nature Conservation, Building.

BMWi. (2010). *Energiekonzept für eine umweltschonende, zuverlässige und bezahlbare Energieversorgung*. Federal Ministry for Economic Affairs.

Bockelmann, F., Fisch, N., & Kipry, H. (2011). *Erdwärme für Bürogebäude nutzen*. OCLC: 845840933. Stuttgart, Germany: Fraunhofer-IRB-Verlag.

Bollin, E., Mangold, D., & Huber, K. (2013). *Solare Wärme für große Gebäude und Wohnsiedlungen*. OCLC: 856798101. Stuttgart, Germany: Fraunhofer IRB Verlag.

Boockmeyer, A., & Bauer, S. (2014). High-temperature heat storage in geological media: High-resolution simulation of near-borehole processes. *Géotechnique Letters*, *4*(2), 151–156. doi:10.1680/geolett.13.00060

Boockmeyer, A., & Bauer, S. (2016). Efficient simulation of multiple borehole heat exchanger storage sites. *Environmental Earth Sciences*, *75*(12), 1021. doi:10.1007/s12665-016-5773-4

Carslaw, H. S., & Jaeger, J. C. (1959). *Conduction of heat in solids* (2nd ed). Oxford [Oxfordshire] : New York: Clarendon Press ; Oxford University Press.

Casasso, A., & Sethi, R. (2014). Sensitivity analysis on the performance of a ground source heat pump equipped with a double U-pipe borehole heat exchanger. *Energy Procedia*, *59*, 301–308. doi:10.1016/j.egypro.2014.10.381

Catolico, N., Ge, S., & McCartney, J. S. (2016). Numerical modeling of a soil-borehole thermal energy storage system. *Vadose Zone Journal*, *15*(1). doi:10.2136/vzj2015.05.0078

Chiasson, A., Rees, S., & Spitler, J. (2000). A preliminary assessment of the effects of ground-water flow on closed-loop ground-source heat pump systems. *ASHRAE Transactions*, *106*(1), 380–393.

Cimmino, M., & Bernier, M. (2014). A semi-analytical method to generate g-functions for geothermal bore fields. *International Journal of Heat and Mass Transfer*, *70*, 641–650. doi:10.1016/j.ijheatmasstransfer.2013.11.037

de Paly, M., Hecht-Méndez, J., Beck, M., Blum, P., Zell, A., & Bayer, P. (2012). Optimization of energy extraction for closed shallow geothermal systems using linear programming. *Geothermics*, *43*, 57–65. doi:10.1016/j.geothermics.2012.03.001

Diersch, H.-J., Bauer, D., Heidemann, W., Rühaak, W., & Schätzl, P. (2011). Finite element modeling of borehole heat exchanger systems. *Computers & Geosciences*, *37*(8), 1122–1135. doi:10.1016/j.cageo.2010.08.003

Doherty, J. (2015). *Calibration and uncertainty analysis for complex environmental models*. OCLC: 991568728.

Emad Dehkordi, S., Schincariol, R. A., & Olofsson, B. (2015). Impact of groundwater flow and energy load on multiple borehole heat exchangers. *Groundwater*, *53*(4), 558–571. doi:10.1111/gwat.12256

Esen, H., & Turgut, E. (2015). Optimization of operating parameters of a ground coupled heat pump system by Taguchi method. *Energy and Buildings*, *107*, 329–334. doi:10.1016/j.enbuild.2015.08.042

Eskilson, P. (1987). *Thermal analysis of heat extraction boreholes*. OCLC: 46010530.

Florides, G., & Kalogirou, S. (2007). Ground heat exchangers - a review of systems, models and applications. *Renewable Energy*, *32*(15), 2461–2478. doi:10.1016/j.renene.2006.12.014

Gao, L., Zhao, J., & Tang, Z. (2015). A review on borehole seasonal solar thermal energy storage. *Energy Procedia*, *70*, 209–218. doi:10.1016/j.egypro.2015.02.117

Gérard, A., Genter, A., Kohl, T., Lutz, P., Rose, P., & Rummel, F. (2006). The deep EGS (Enhanced Geothermal System) project at Soultz-sous-Forêts (Alsace, France). *Geothermics*, *35*(5), 473–483. doi:10.1016/j.geothermics.2006.12.001

Gholap, A., & Khan, J. (2007). Design and multi-objective optimization of heat exchangers for refrigerators. *Applied Energy*, *84*(12), 1226–1239. doi:10.1016/j.apenergy.2007.02.014

Gultekin, A., Aydin, M., & Sisman, A. (2016). Thermal performance analysis of multiple borehole heat exchangers. *Energy Conversion and Management*, *122*, 544–551. doi:10.1016/j.enconman.2016.05.086

Gultekin, A., Aydin, M., & Sisman, A. (2019). Effects of arrangement geometry and number of boreholes on thermal interaction coefficient of multi-borehole heat exchangers. *Applied Energy*, *237*, 163–170. doi:10.1016/j.apenergy.2019.01.027

Hähnlein, S., Bayer, P., Ferguson, G., & Blum, P. (2013). Sustainability and policy for the thermal use of shallow geothermal energy. *Energy Policy*, *59*, 914–925. doi:10.1016/j.enpol.2013.04.040

Hauer, A., Hiebler, S., & Reuß, M. (2013). *Wärmespeicher*. OCLC: 857326072. Stuttgart, Germany: Fraunhofer IRB Verlag.

HeidelbergCement. (2019). *ThermoCem©*.

Heier, J., Bales, C., Sotnikov, A., & Ponomarova, G. (2011). Evaluation of a high temperature solar thermal seasonal borehole storage. In *Proceedings of ISES Solar World Congress*.

Hein, P., Kolditz, O., Görke, U.-J., Bucher, A., & Shao, H. (2016). A numerical study on the sustainability and efficiency of borehole heat exchanger coupled ground source heat pump systems. *Applied Thermal Engineering*, *100*, 421–433. doi:10.1016/j.applthermaleng.2016.02.039

Huang, S., Ma, Z., & Wang, F. (2015). A multi-objective design optimization strategy for vertical ground heat exchangers. *Energy and Buildings*, *87*, 233–242. doi:10.1016/j.enbuild.2014.11.024

IEA. (2008). *Worldwide energy trends in energy use and efficiency*. International Energy Agency, Paris, France.

IEA. (2013). *Redrawing the the energy climate map*. International Energy Agency, Paris, France.

Ingersoll, L. R., Zobel, O. J., & Ingersoll, A. C. (1954). *Heat conduction with engineering, geological and other applications*. Madison, WI: University of Wisconsin Press.

IPCC, Pachauri, R., & Mayer, L. (2014). *Climate change 2014: Synthesis report*. OCLC: 914851124. Geneva, Switzerland: Contribution of Working Groups I, II and III to the Fifth Assessment Report of the Intergovernmental Panel on Climate Change.

Javed, S., & Claesson, J. (2011). New analytical and numerical solutions for the short-term analysis of vertical ground heat exchangers. *ASHRAE Transactions*, *117*(1), 3–12.

Jesußek, A., Grandel, S., & Dahmke, A. (2013). Impacts of subsurface heat storage on aquifer hydrogeochemistry. *Environmental Earth Sciences*, *69*(6), 1999–2012. doi:10.1007/s12665-012-2037-9

Kabuth, A., Dahmke, A., Beyer, C., Bilke, L., Dethlefsen, F., Dietrich, P., ... Bauer, S. (2017). Energy storage in the geological subsurface: Dimensioning, risk analysis and spatial planning: The ANGUS+ project. *Environmental Earth Sciences*, *76*(1), 23. doi:10.1007/s12665-016-6319-5

Al-Khoury, R., & Bonnier, P. G. (2006). Efficient finite element formulation for geothermal heating systems. part II: Transient. *International Journal for Numerical Methods in Engineering*, *67*(5), 725–745. doi:10.1002/nme.1662

Al-Khoury, R., Bonnier, P. G., & Brinkgreve, R. B. J. (2005). Efficient finite element formulation for geothermal heating systems. part I: Steady state. *International Journal for Numerical Methods in Engineering*, *63*(7), 988–1013. doi:10.1002/nme.1313

Kohl, T., Brenni, R., & Eugster, W. (2002). System performance of a deep borehole heat exchanger. *Geothermics*, *31*(6), 687–708. doi:10.1016/S0375-6505(02)00031-7

Kolditz, O., Bauer, S., Bilke, L., Böttcher, N., Delfs, J. O., Fischer, T., ... Zehner, B. (2012). OpenGeoSys: An open-source initiative for numerical simulation of thermo-hydro-mechanical/chemical (THM/c) processes in porous media. *Environmental Earth Sciences*, *67*(2), 589–599. doi:10.1007/s12665-012-1546-x

Kolditz, O., & Bauer, S. (2004). A process-oriented approach to computing multi-field problems in porous media. *Journal of Hydroinformatics*, *6*(3), 225–244. doi:10.2166/hydro.2004.0017

Koohi-Fayegh, S., & Rosen, M. (2014). An analytical approach to evaluating the effect of thermal interaction of geothermal heat exchangers on ground heat pump efficiency. *Energy Conversion and Management*, *78*, 184–192. doi:10.1016/j.enconman.2013.09.064

Koohi-Fayegh, S., & Rosen, M. A. (2012). Examination of thermal interaction of multiple vertical ground heat exchangers. *Applied Energy*, *97*, 962–969. doi:10.1016/j.apenergy.2012.02.018

Lanini, S., Delaleux, F., Py, X., Olivès, R., & Nguyen, D. (2014). Improvement of borehole thermal energy storage design based on experimental and modelling results. *Energy and Buildings*, *77*, 393–400. doi:10.1016/j.enbuild.2014.03.056

Law, Y. L. E., & Dworkin, S. B. (2016). Characterization of the effects of borehole configuration and interference with long term ground temperature modelling of ground source heat pumps. *Applied Energy*, *179*, 1032–1047. doi:10.1016/j.apenergy.2016.07.048

Li, C., Mao, J., Zhang, H., Li, Y., Xing, Z., & Zhu, G. (2017). Effects of load optimization and geometric arrangement on the thermal performance of borehole heat exchanger fields. *Sustainable Cities and Society*, *35*, 25–35. doi:10.1016/j.scs.2017.07.018

Li, D., Bauer, S., Benisch, K., Graupner, B., & Beyer, C. (2014). OpenGeoSys-ChemApp: A coupled simulator for reactive transport in multiphase systems and application

to CO2 storage formation in northern germany. *Acta Geotechnica*, *9*(1), 67–79. doi:10.1007/s11440-013-0234-7

Li, M., & Lai, A. C. (2012). Parameter estimation of in-situ thermal response tests for borehole ground heat exchangers. *International Journal of Heat and Mass Transfer*, *55*(9), 2615–2624. doi:10.1016/j.ijheatmasstransfer.2011.12.033

Lienen, T., Lüders, K., Halm, H., Westphal, A., Köber, R., & Würdemann, H. (2017). Effects of thermal energy storage on shallow aerobic aquifer systems: Temporary increase in abundance and activity of sulfate-reducing and sulfur-oxidizing bacteria. *Environmental Earth Sciences*, *76*(6), 261. doi:10.1007/s12665-017-6575-z

LLUR. (2012). Geologische Übersichtskarte von Schleswig-Holstein 1:250 000. Landesamt für Landwirtschaft, Umwelt und ländliche Räume (LLUR) - Geologischer Dienst.

Lüders, K., Firmbach, L., Ebert, M., Dahmke, A., Dietrich, P., & Köber, R. (2016). Gas-phase formation during thermal energy storage in near-surface aquifers: Experimental and modelling results. *Environmental Earth Sciences*, *75*(21), 1404. doi:10.1007/s12665-016-6181-5

Lundh, M., & Dalenbäck, J.-O. (2008). Swedish solar heated residential area with seasonal storage in rock: Initial evaluation. *Renewable Energy*, *33*(4), 703–711. doi:10.1016/j.renene.2007.03.024

Mangold, D. (2007). Seasonal storage - a German success story. *Sun & Wind Energy*, *1*, 48–58.

Mangold, D., Miedaner, O., Primoudi Tziggili, E., Schmidt, T., Unterberger, M., & Zeh, B. (2012). *Technisch-wirtschaftliche Analyse und Weiterentwicklung der solaren Langzeit-Wärmespeicherung (Dezember 2007 bis Februar 2011)*. Stuttgart, Germany.

Marcotte, D., & Pasquier, P. (2008). On the estimation of thermal resistance in borehole thermal conductivity test. *Renewable Energy*, *33*(11), 2407–2415. doi:10.1016/j.renene.2008.01.021

McCartney, J., Başer, T., Zhan, N., Lu, N., Ge, S., & Smits, K. (2017). Storage of solar thermal energy in borehole thermal energy storage systems. In *Proceedings of the IGSHPA Technical/Research Conference and Expo 2017*. doi:10.22488/okstate.17.000512

Molina-Giraldo, N., Blum, P., Zhu, K., Bayer, P., & Fang, Z. (2011). A moving finite line source model to simulate borehole heat exchangers with groundwater advection. *International Journal of Thermal Sciences*, *50*(12), 2506–2513. doi:10.1016/j.ijthermalsci.2011.06.012

Ndao, S., Peles, Y., & Jensen, M. K. (2009). Multi-objective thermal design optimization and comparative analysis of electronics cooling technologies. *International Journal of Heat and Mass Transfer*, *52*(19-20), 4317–4326. doi:10.1016/j.ijheatmasstransfer.2009.03.069

NETL. (2017). *Risk management and simulation for geologic storage projects*. National Energy Technology Laboratory at the U.S. Department of Energy.

Nilsson, E., & Rohdin, P. (2019). Empirical validation and numerical predictions of an industrial borehole thermal energy storage. *Energies*, *12*(12), 2263. doi:10.3390/en12122263

Nordell, B. (1990). *The borehole heat store in rock at the University of Luleå: The Lulevärme project, 1982-1988*. OCLC: 22620641. Stockholm, Sweden: Swedish Council for Building Research.

Nordell, B. (1993). *Borehole heat store design optimization*. Luleå, Sweden: Luleå University of Technology.

Nordell, B., & Hellström, G. (2000). High temperature solar heated seasonal storage system for low temperature heating of buildings. *Solar Energy*, *69*(6), 511–523. doi:10.1016/S0038-092X(00)00120-1

Nußbicker-Lux, J. (2010). *Simulation und Dimensionierung solar unterstützter Nahwärmesysteme mit Erdsonden-Wärmespeicher*. Stuttgart, Germany: Universität Stuttgart.

Oreskes, N. (2018). The scientific consensus on climate change: How do we know we're not wrong? In E. A. Lloyd & E. Winsberg (Eds.), *Climate modelling: Philosophical and conceptual issues* (pp. 31–64). doi:10.1007/978-3-319-65058-6_2

Pandey, N., Murugesan, K., & Thomas, H. (2017). Optimization of ground heat exchangers for space heating and cooling applications using Taguchi method and utility concept. *Applied Energy*, *190*, 421–438. doi:10.1016/j.apenergy.2016.12.154

Pannike, S., Kölling, M., Schulz, H., Panteleit, B., Reichling, J., & Scheps, V. (2006). Auswirkung hydrogeologischer Kenngrößen auf die Kältefahnen von Erdwärmesondenanlagen in Lockersedimenten. *Grundwasser*, *11*(1), 6–18. doi:10.1007/s00767-006-0114-2

Pasten, C., & Santamarina, J. C. (2011). Energy geo-storage - analysis and geomechanical implications. *KSCE Journal of Civil Engineering*, *15*(4), 655–667. doi:10.1007/s12205-011-0006-6

Pinel, P., Cruickshank, C. A., Beausoleil-Morrison, I., & Wills, A. (2011). A review of available methods for seasonal storage of solar thermal energy in residential applications. *Renewable and Sustainable Energy Reviews*, *15*(7), 3341–3359. doi:10.1016/j.rser.2011.04.013

Popp, S., Beyer, C., Dahmke, A., & Bauer, S. (2015). Model development and numerical simulation of a seasonal heat storage in a contaminated shallow aquifer. *Energy Procedia*, *76*, 361–370. doi:10.1016/j.egypro.2015.07.842

Popp, S., Beyer, C., Dahmke, A., Koproch, N., Köber, R., & Bauer, S. (2016). Temperature-dependent dissolution of residual non-aqueous phase liquids: Model development and verification. *Environmental Earth Sciences*, *75*(11), 953. doi:10.1007/s12665-016-5743-x

Poulsen, S. E., & Alberdi-Pagola, M. (2015). Interpretation of ongoing thermal response tests of vertical (BHE) borehole heat exchangers with predictive uncertainty based stopping criterion. *Energy*, *88*, 157–167. doi:10.1016/j.energy.2015.03.133

Pu, L., Qi, D., Xu, L., & Li, Y. (2017). Optimization on the performance of ground heat exchangers for GSHP using Kriging model based on MOGA. *Applied Thermal Engineering*, *118*, 480–489. doi:10.1016/j.applthermaleng.2017.02.114

Qian, H., & Wang, Y. (2014). Modeling the interactions between the performance of ground source heat pumps and soil temperature variations. *Energy for Sustainable Development*, *23*, 115–121. doi:10.1016/j.esd.2014.08.004

Rad, F. M., & Fung, A. S. (2016). Solar community heating and cooling system with borehole thermal energy storage - Review of systems. *Renewable and Sustainable Energy Reviews*, *60*, 1550–1561. doi:10.1016/j.rser.2016.03.025

Rapantova, N., Pospisil, P., Koziorek, J., Vojcinak, P., Grycz, D., & Rozehnal, Z. (2016). Optimisation of experimental operation of borehole thermal energy storage. *Applied Energy*, *181*, 464–476. doi:10.1016/j.apenergy.2016.08.091

Rees, S. (Ed.). (2016). *Advances in ground-source heat pump systems*. Amsterdam: Woodhead Publishing, imprint of Elsevier, Number 100.

Rehman, H. u., Hirvonen, J., & Sirén, K. (2017). A long-term performance analysis of three different configurations for community-sized solar heating systems in high latitudes. *Renewable Energy*, *113*, 479–493. doi:10.1016/j.renene.2017.06.017

Rehman, H. u., Hirvonen, J., & Sirén, K. (2018). Performance comparison between optimized design of a centralized and semi-decentralized community size solar district heating system. *Applied Energy*, *229*, 1072–1094. doi:10.1016/j.apenergy.2018.08.064

Retkowski, W., Ziefle, G., & Thöming, J. (2015). Evaluation of different heat extraction strategies for shallow vertical ground-source heat pump systems. *Applied Energy*, *149*, 259–271. doi:10.1016/j.apenergy.2015.03.004

Rivera, J. A., Blum, P., & Bayer, P. (2015). Ground energy balance for borehole heat exchangers: Vertical fluxes, groundwater and storage. *Renewable Energy*, *83*, 1341–1351. doi:10.1016/j.renene.2015.05.051

Rivera, J. A., Blum, P., & Bayer, P. (2016). A finite line source model with Cauchy-type top boundary conditions for simulating near surface effects on borehole heat exchangers. *Energy*, *98*, 50–63. doi:10.1016/j.energy.2015.12.129

Rosato, A., Ciervo, A., Ciampi, G., Scorpio, M., & Sibilio, S. (2019). Impact of seasonal thermal energy storage design on the dynamic performance of a solar heating system serving a small-scale Italian district composed of residential and school buildings. *Journal of Energy Storage*, *25*, 100889. doi:10.1016/j.est.2019.100889

Sanner, B., & Knoblich, K. (1999). Advantages and problems of high temperature underground thermal energy storage. *Bulletin d'Hydrogéologie*, *17*, 341–348.

Santamouris, M. (Ed.). (2001). *Energy and climate in the urban built environment.* London: James & James.

Sass, I., & Lehr, C. (2011). Improvements on the thermal response test evaluation applying the cylinder source theory. In *Proceedings of the Thirty-Sixth Workshop on Geothermal Reservoir Engineering.*

Sayyaadi, H., Amlashi, E. H., & Amidpour, M. (2009). Multi-objective optimization of a vertical ground source heat pump using evolutionary algorithm. *Energy Conversion and Management*, *50*(8), 2035–2046. doi:10.1016/j.enconman.2009.04.006

Schmidt, T., Mangold, D., & Müller-Steinhagen, H. (2003). Seasonal thermal energy storage in Germany. In *Proceedings of ISES Solar World Congress*, Gothenburg, Sweden.

Schmidt, T. (2015). Erfahrungen mit großen BTES in Deutschland - Das Beispiel der solaren Fernwärme mit saisonalem Erdsonden-Wärmespeicher in Crailsheim. Steinbeis Forschungsinstitut für solare und zukunftsfähige thermische Energiesysteme.

Schmidt, T., & Sørensen, P. A. (2018). Monitoring results from large scale heat storages for district heating in Denmark. In *Proceedings of 14th International Conference on Energy Storage*, Adana, Turkey.

Schulte, D. O., Rühaak, W., Oladyshkin, S., Welsch, B., & Sass, I. (2016a). Optimization of medium-deep borehole thermal energy storage. *Energy Technology*, *4*(1), 104–113. doi:10.1002/ente.201500254

Schulte, D. O., Welsch, B., Boockmeyer, A., Rühaak, W., Bär, K., Bauer, S., & Sass, I. (2016b). Modeling insulated borehole heat exchangers. *Environmental Earth Sciences*, *75*(10), 910. doi:10.1007/s12665-016-5638-x

Shonder, J. A., & Beck, J. V. (1999). Determining effective soil formation thermal properties from field data using a parameter estimation technique. *ASHRAE Transactions*, *105*(1), 458–466.

Sibbitt, B., McClenahan, D., Djebbar, R., Thornton, J., Wong, B., Carriere, J., & Kokko, J. (2012). The performance of a high solar fraction seasonal storage district heating system - five years of operation. *Energy Procedia*, *30*, 856–865. doi:10.1016/j.egypro.2012.11.097

Sibbitt, B., Onno, T., McClenahan, D., Thornton, J., Brunger, A., Kokko, J., & Wong, B. (2007). The Drake Landing Solar Community Project - early results. In *Proceedings of the 32nd Annual Conference of the Solar Energy Society of Canada*, Calgary, Canada.

Signorelli, S., Bassetti, S., Pahud, D., & Kohl, T. (2007). Numerical evaluation of thermal response tests. *Geothermics*, *36*(2), 141–166. doi:10.1016/j.geothermics.2006.10.006

Signorelli, S., Kohl, T., & Rybach, L. (2005). Sustainability of production from borehole heat exchanger fields. In *Proceedings World Geothermal Congress*, Antalya, Turkey.

Sivasakthivel, T., Murugesan, K., & Sahoo, P. (2014). Optimization of ground heat exchanger parameters of ground source heat pump system for space heating applications. *Energy*, *78*, 573–586. doi:10.1016/j.energy.2014.10.045

Skarphagen, H., Banks, D., Frengstad, B., & Gether, H. (2019). Design considerations for borehole thermal energy storage (BTES): A review with emphasis on convective heat transfer. *Geofluids*, *2019*, 1–26. doi:10.1155/2019/4961781

Sørensen, P. A., Larsen, J., Thøgersen, L., Dannemand Andersen, J., Østergaard, C., & Schmidt, T. (2013). *Boreholes in Brædstrup.*

Sørensen, P. A., & Schmidt, T. (2018). Design and construction of large scale heat storages for district heating in Denmark. In *Proceedings of 14th International Conference on Energy Storage*, Adana, Turkey.

Sternberg, A., & Bardow, A. (2015). Power-to-what? - Environmental assessment of energy storage systems. *Energy & Environmental Science*, *8*(2), 389–400. doi:10.1039/C4EE03051F

UBA. (2013). *Und sie erwärmt sich doch - Was steckt hinter der Debatte um den Klimawandel?* Umweltbundesamt, Dessau-Roßlau, Germany.

Underground Energy. (2019). Last access 25.09.2019. Retrieved from https://underground-energy.com/our-technology/btes/

USGCRP, Wuebbles, D., Fahey, D., Hibbard, K., Dokken, D., Stewart, B., & Maycock, T. (2017). *Climate science special report: Fourth national climate assessment, Volume I.* U.S. Global Change Research Program. doi:10.7930/J0J964J6

van Meurs, G. A. M. (1985). *Seasonal heat storage in the soil.* Pijnacker, Netherlands: Dutch Efficiency Bureau.

Vandenbohede, A., Hermans, T., Nguyen, F., & Lebbe, L. (2011). Shallow heat injection and storage experiment: Heat transport simulation and sensitivity analysis. *Journal of Hydrology*, *409*(1), 262–272. doi:10.1016/j.jhydrol.2011.08.024

VDI 4640 Part 1. (2010). *Thermal use of the underground - Fundamentals, approvals, environmental aspects.* Verein deutscher Ingenieure e.V., Düsseldorf, Germany.

VDI 4640 Part 2. (2001). *Thermal use of the underground - Ground source heat pump systems.* Verein deutscher Ingenieure e.V., Düsseldorf, Germany.

VDI 4640 Part 3. (2001). *Utilization of the subsurface for thermal purposes - Underground thermal energy storage*. Verein deutscher Ingenieure e.V., Düsseldorf, Germany.

Vienken, T., Schelenz, S., Rink, K., & Dietrich, P. (2015). Sustainable intensive thermal use of the shallow subsurface-a critical view on the status quo. *Groundwater*, *53*(3), 356–361. doi:10.1111/gwat.12206

Wagner, V., Bayer, P., Kübert, M., & Blum, P. (2012). Numerical sensitivity study of thermal response tests. *Renewable Energy*, *41*, 245–253. doi:10.1016/j.renene.2011.11.001

Wagner, W., & Kruse, A. (1998). *Properties of water and steam: The industrial standard IAPWS-IF97 for the thermodynamic properties and supplementary equations for other properties*. OCLC: 864099740. Berlin, Heidelberg: Springer Berlin Heidelberg.

Wang, W., Kosakowski, G., & Kolditz, O. (2009). A parallel finite element scheme for thermo-hydro-mechanical (THM) coupled problems in porous media. *Computers & Geosciences*, *35*(8), 1631–1641. doi:10.1016/j.cageo.2008.07.007

Watanabe, N., Wang, W., Taron, J., Görke, U. J., & Kolditz, O. (2012). Lower-dimensional interface elements with local enrichment: Application to coupled hydro-mechanical problems in discretely fractured porous media. *International Journal for Numerical Methods in Engineering*, n/a–n/a. doi:10.1002/nme.3353

Welsch, B., Rühaak, W., Schulte, D. O., Bär, K., & Sass, I. (2016). Characteristics of medium deep borehole thermal energy storage. *International Journal of Energy Research*, *40*(13), 1855–1868. doi:10.1002/er.3570

Wijsman, A., & Havinga, J. (1988). Monitoring results of the Groningen-CSHPSS. In *Advances in solar energy technology* (pp. 1232–1237). doi:10.1016/B978-0-08-034315-0.50239-1

Yang, H., Cui, P., & Fang, Z. (2010). Vertical-borehole ground-coupled heat pumps: A review of models and systems. *Applied Energy*, *87*(1), 16–27. doi:10.1016/j.apenergy.2009.04.038

Zhang, C., Guo, Z., Liu, Y., Cong, X., & Peng, D. (2014). A review on thermal response test of ground-coupled heat pump systems. *Renewable and Sustainable Energy Reviews*, *40*, 851–867. doi:10.1016/j.rser.2014.08.018

Zhu, N., Hu, P., Xu, L., Jiang, Z., & Lei, F. (2014). Recent research and applications of ground source heat pump integrated with thermal energy storage systems: A review. *Applied Thermal Engineering*, *71*(1), 142–151. doi:10.1016/j.applthermaleng.2014.06.040

Eidesstattliche Erklärung

Hiermit versichere ich eidesstattlich, dass die vorliegende Arbeit, abgesehen von der Beratung durch den Betreuer, nach Inhalt und Form selbstständig und ohne unzulässige Hilfsmittel von mir angefertigt wurde. Die vorliegende Arbeit hat weder in Teilen noch im Ganzen an anderer Stelle im Rahmen eines Prüfungsverfahrens vorgelegen und wurde nicht veröffentlicht oder zur Veröffentlichung eingereicht. Weiterhin versichere ich, dass die Arbeit unter Einhaltung der Regeln guter wissenschaftlicher Praxis der Deutschen Forschungsgemeinschaft angefertigt wurde und dass mir kein akademischer Grad entzogen wurde.

Meerbusch, 15.05.2020

Anke Boockmeyer

Danksagung

Ich möchte gerne die Möglichkeit nutzen und den Menschen danken, die mich bei der Erarbeitung meiner Doktorarbeit unterstützt haben. Zunächst danke ich meinem Doktorvater Prof. Dr. Sebastian Bauer dafür, dass er mir die Promotion an seinem Lehrstuhl ermöglicht hat. Seine wertvollen Anregungen und hilfreichen Ideen in unseren zahlreichen Diskussionen haben sehr zu der Fertigstellung dieser Arbeit beigetragen. Darüber hinaus möchte ich mich insbesondere bei ihm bedanken für seine Hilfestellung und Betreuung über die Zeit an der Universität Kiel hinaus sowie die Motivation in schweren Zeiten.

Ein großer Dank geht auch an meinen Kollegen Dr. Christof Beyer für die fachliche Unterstützung und aufbauenden Worte während meiner Promotion.

Außerdem möchte ich mich bei der gesamten Arbeitsgruppe bedanken für ihre Hilfsbereitschaft und die konstruktive Arbeitsamthmosphäre, und dabei besonders Dr. Katharina Benisch, Steffi Popp, Tessa Strutz, und Dr. Wolf Tilmann Pfeiffer für die wunderbare gemeinsame Zeit und die emotionale Unterstützung.

Ich danke auch meinen Freunden Inga Grunwald, Kristina Köster, Anne Raguse und Nico Koproch, die jederzeit ein offenes Ohr für mich hatten und mich den gesamten Weg begleitet und bestärkt haben, auch wenn es ihnen sicher nicht immer leicht gefallen ist. Kristin Hamann möchte ich zusätzlich auch für die Korrekturen der Texte danken.

Ganz besonders möchte ich mich bei meiner Mutter bedanken für ihre Hilfe in all den Jahren und den Rückhalt, den ich zeitweise gebraucht habe.

Schließlich gilt mein außerordentlicher Dank meinem Partner Patrick Fey, der mir mit seinem Verständnis und seinem moralischen Beistand die Kraft gegeben hat, die Dissertation fertigzustellen.